

Planar Groove Gap Waveguides



Titus Oluwale Oyedokun

Thesis Presented for the Degree of

DOCTOR OF PHILOSOPHY

in the Department of Electrical Engineering

UNIVERSITY OF CAPE TOWN

January, 2019

The copyright of this thesis vests in the author. No quotation from it or information derived from it is to be published without full acknowledgement of the source. The thesis is to be used for private study or non-commercial research purposes only.

Published by the University of Cape Town (UCT) in terms of the non-exclusive license granted to UCT by the author.

“It always seems impossible until it’s done.”

-Nelson Rolihlahla Mandela

Declaration

I declare that this thesis is my own, unaided work. It is being submitted for the degree of Doctor of Philosophy in Engineering in the University of Cape Town. It has not been submitted before for any degree or examination in any other university.

Signed by candidate

Signature of Author

Cape Town

January 31, 2019

Abstract

With the increasing demand for wireless services and applications, the integration and coexistence of multi-standard and multi-band operations into a single device has led to intensive research in the design of tunable and reconfigurable planar devices. A planar medium to achieve this integration is the [Substrate Integrated Waveguide \(SIW\)](#). However, due to a lack of DC isolated planes of the structure, bridging wires or concentric etched rings are often used to enable active device biasing.

This research presents a novel planar structure referred to as the [Planar Groove Gap Waveguide \(PGGWG\)](#). The new structure has similar modal characteristics to air-filled machined [Groove Gap Waveguide \(GGWG\)](#), but in a low-cost fabrication technology that is readily integrated with surface mount components. The structure provides two DC isolated conducting planes, while still providing a low loss planar transmission medium. Simulation results demonstrate the existence of a TE_{10} propagating mode within the artificially created bandgap. There is good agreement between de-embedded simulated and measured results over the usable bandwidth of the waveguide (28 to 40 GHz). A passband is measured having an average insertion loss of 1.2 dB and 0.5 dB insertion loss variation implemented on a substrate of relative permittivity ϵ_r of 3.5, and loss tangent of 0.004.

The broadband characterization of the transmission line loss and phase constant for [PGGWG](#) at K_a -band shows that [PGGWG](#) has comparable attenuation over the band of interest to [SIW](#). The transmission line Q-factor is found to vary from 135 to 140 over the band of interest, which is comparable to [SIW](#) in the same

medium. PGGWG is also found to have a phase constant of nearly double that of comparable SIW, which is a significant results for system miniaturization. The unloaded Q-factor of a 33.5GHz PGGWG rectangular cavity resonator is measured to be 209. This is found to be comparable to an SIW resonator on the same substrate and frequency band.

This work further explores the DC isolation property of the PGGWG by presenting electrically tunable PGGWG resonant cavities. It is found that a simple biasing network can be applied to the cavity using a varactor diode to vary the resonant frequency of the cavity. This is done without bridging wire and concentric etched rings as a direct result of the DC isolation of the PGGWG. A tuning range of 4.5% is achieved in measurement.

From the experiments conducted, it is concluded that PGGWG can be used as an alternative planar waveguide media. The PGGWG platform can be used in the design and implementation of RF front-end components at millimeter waves. Its DC isolated conducting planes also provide a simple way of biasing active components in frequency agile applications.

Acknowledgements

I would like to express my sincere gratitude and appreciation to the following people for their contributions towards the completion of this thesis:

To my supervisors, Prof Riana Geschke and Dr Tinus Stander, thank you for your support, patience, and encouragement throughout my doctoral program. Your technical inputs have been invaluable. I have learned a lot from you both over the years through your mentorship.

To my family, your love, support and encouragement remains unwavering. I am grateful to God each day for blessing me with you all. This would have been nearly impossible without your support. Thank you once again for always being there for me at each step of the way.

To members of the Radar Remote Sensing Group (RRSG) at the University of Cape Town, thank you for all your support throughout the years. RRSG has been my academic home since undergraduate studies. To my lab mate, Leokadia Nepaya, thank you for getting me up to speed with some foundation theory and for the encouragement.

To Victoria Iyun, my companion, thank you for all the encouragement and support you have shown to me. Thank you for sparing the time to listen to me talk about my work and reading my write up.

To Rikus Nel at the Carl and Emily Fuchs Institute for Microelectronics (CE-FIM), University of Pretoria, South Africa. Thank you for taking the time out to help with taking macroscopic pictures of different cut of the fabricated circuits.

I would also like to thank Hannes Venter, also at CEFIM, who assisted me with measurements using the microwave lab at CEFIM. In addition, thank for your knowledge sharing on varactor diodes.

I also extend my appreciation to MACOM for the varactor diode samples used to prototype the design conducted in this work and Smittech (Pty)Ltd for the precision assembly.

The financial assistance of the National Research Foundation (Scholarship 99870 and Grant number 88100) towards this research is hereby acknowledged. Opinions expressed and conclusions arrived at, are those of the author and are not necessarily to be attributed to the NRF.

The use of CST Microwave Studio and NI AWR Microwave office academic licenses are also hereby acknowledged.

Contents

Declaration	ii
Abstract	iii
Acknowledgements	v
Contents	vii
List of Figures	x
List of Tables	xviii
1 Introduction	1
1.1 Background	2
1.2 Problem Statement	8
1.3 Objectives of Research	9
1.4 Original Contributions	10
1.5 Publications	10
1.6 Outline of the Thesis	10
2 Literature Review	12
2.1 Introduction	12
2.2 Rectangular Waveguide	13
2.3 Gap Waveguide Technology	14
2.4 Artificial Magnetic Conductors and Electromagnetic Bandgaps . .	16
2.5 Groove Gap Waveguide	19

2.6	Ridge Gap Waveguide	22
2.7	Microstrip Gap Waveguide	22
2.8	Tunable Substrate Integrated Waveguide Structures	24
2.9	Conclusion	28
3	Propagation Characterisation of a Planar Groove Gap Waveguide	29
3.1	Introduction	29
3.2	Basic Geometry	29
3.3	Simulation Analysis of the Embedded EBG Structure	32
3.3.1	Effect of the number of EBG rows on attenuation	34
3.3.2	Effect of varying the height h on the stopband	35
3.3.3	Effect of varying the gap height h_a on the stopband	36
3.3.4	Effect of pitch p variation on the stopband	37
3.3.5	Effect of varying the via diameter v_d on the stopband	38
3.3.6	Effect of varying the catch pad p_d surface area	39
3.3.7	Effect of the dielectric constant ϵ_r on the bandgap	40
3.4	Dispersion Diagram	43
3.5	Modal Analysis	47
3.6	S-Parameter Analysis	48
3.7	Conclusion	51
4	PGGWG Prototyping and Measurement	53
4.1	Introduction	53
4.2	Wideband Coplanar Waveguide to PGGWG Transition	54
4.3	PGGWG Calibration Standards	57
4.4	Fabrication Processes and Measurement Setup	60
4.5	PGGWG Measurement Results and Comparison to Simulation	63
4.6	Conclusion	66
5	Broadband Propagation and Resonant Characterisation of Planar Groove Gap Waveguide	67
5.1	Introduction	67
5.2	Propagation Constant Analysis of PGGWG	68

5.3	Planar Groove Gap Waveguide Resonant Cavities	73
5.4	Quality Factor of PGGWG Resonant Cavity	74
5.5	Conclusion	79
6	Tunable Planar Groove Gap Waveguide Cavity	80
6.1	Introduction	80
6.2	Tunable Cavity Geometry	80
6.3	Varactor Loading and DC Biasing	83
6.3.1	Biasing coupled, cascaded resonators	84
6.4	Varactor Diode Selection	85
6.5	Hybrid EM-Circuit Simulation	88
6.6	Fabricated Circuit and Measurement	93
6.7	Conclusion	97
7	Conclusions	98
7.1	Recommendations for Future Developments	100
A	Connector	104
B	Varactor diode	105
	Bibliography	108

List of Figures

1.1	SIW topology	3
1.2	Variants of SIW (a) FSIW (b) RSIW	4
1.3	Top conductor layout of Corrugated Substrate Integrated Waveguide topology	5
1.4	Decoupled empty SIW.	6
1.5	Slow-Wave SIW.	7
1.6	Planar waveguides derived from the gap waveguide. (a) Printed Ridge Gap Waveguide. (b) Substrate Integrated Gap Waveguide.	8
2.1	Rectangular Waveguide	13
2.2	Operating principle of the GW. (a) PEC and PMC plate at a distance h apart. (b) Bottom PEC plate embedded by PMC on both sides.	15
2.3	A cross section of the GW.	15
2.4	PEC/PMC strip representing an ideal soft and hard surfaces. The red and green arrows represent the direction of propagation of the waves of the soft and hard surface respectively	17
2.5	Geometry of pin lattice and mushroom-type EBG layers realised within parallel-plate waveguide	18

2.6	Geometry of the mushroom-type EBG realised on multi layer PCB process. (a) EBG consisting of a catch pad and via to ground. (b) Embedded EBG within the parallel plate	19
2.7	Cross section of the GGWG for (a) Horizontal and (b) Vertical polarisation	20
2.8	Cross section of the GGWG for horizontal polarization.	21
2.9	Cross section of the RGW with e-field of the fundamental propagating mode.	22
2.10	Cross section of the suspended microstrip line within the GW	23
2.11	Cross section of the different microstrip line implementation within the GW	24
2.12	SIW tunable resonant cavity showing the centre conducting post and the floating metal patches	26
3.1	Cross-section view of the PGGWG with layer stackup. All layers have the same relative permittivity	30
3.2	Physical GGWG layouts (a) 3D view of a micro-machined GGWG (b) PGGWG derivative	31
3.3	Embedded EBG structure unit cell as adopted in the PGGWG structure. This also shows the lumped element model of the structure.	32
3.4	A side view showing the simulation setup used to extract the bandgap of an array of EBG cells within parallel plate structure using S-parameters.	33
3.5	S-parameters; S_{11} (dB) and S_{21} (dB) for the setup in Figure 3.4. The embedded EBG mushroom type structure has the following dimensions: $h = 0.508$ mm, $h_a = 0.106$ mm, $v_d = 0.3$ mm, $p_d = 0.8$ mm, $p = 0.95$ mm, $\epsilon_r = 3.5$, $\tan\delta = 0.004$	34

3.6	Magnitude of S_{21} (dB) for different number of unit cells with the following dimensions: $h = 0.508$ mm, $h_a = 0.106$ mm, $v_d = 0.3$ mm, $p_d = 0.9$ mm, $p = 0.95$ mm, $\epsilon_r = 3.5$, $\tan\delta = 0.004$	35
3.7	Magnitude of S_{21} (dB) for different via height h of the EBG unit cells with the following dimensions: $h_a = 0.106$ mm, $v_d = 0.3$ mm, $p_d = 0.8$ mm, $p = 0.95$ mm, $\epsilon_r = 3.5$, $\tan\delta = 0.004$	36
3.8	Magnitude of S_{21} (dB) for different the gap height h_a of embedded EBG unit cells with the following dimensions: $h = 0.508$ mm, $v_d = 0.3$ mm, $p_d = 0.8$ mm, $p = 0.95$ mm, $\epsilon_r = 3.5$, $\tan\delta = 0.004$	37
3.9	Magnitude of S_{21} (dB) for different values of pitch p of the EBG unit cells with the following dimensions: $h_a = 0.106$ mm $h = 0.508$ mm, $v_d = 0.3$ mm, $p_d = 0.8$ mm, $\epsilon_r = 3.5$, $\tan\delta = 0.004$	38
3.10	Magnitude of S_{21} (dB) for different via diameter, v_d of the EBG unit cells with the following dimensions: $h_a = 0.106$ mm $h = 0.508$ mm, $p_d = 0.8$ mm, $p = 0.95$ mm, $\epsilon_r = 3.5$, $\tan\delta = 0.004$	39
3.11	Magnitude of S_{21} (dB) for different embedded EBG structures in parallel planes showing the effect of different pad diameter and patch sizes	40
3.12	Magnitude of S_{21} (dB) for different substrate material of ϵ_r . The dimensions of the EBG unit cell are: $h_a = 0.106$ mm $h = 0.508$ mm, $p_d = 0.8$ mm, $p = 0.95$ mm.	41
3.13	Magnitude of S_{21} (dB) for different substrate heights h . The dimensions of the EBG unit cell are: $h_a = 0.106$ mm $h = 0.508$ mm, $p_d = 0.8$ mm, $p = 0.95$ mm, $\epsilon_r = 3.5$	42
3.14	The 3D model setup used in extracting the propagating modes within the PGGWG for plotting the dispersion diagram. The waveguide dimensions are: $h = 0.508$, $w = 4.5$ mm, $h_a = 0.106$ mm, $v_d = 0.3$ mm, $p_d = 0.8$ mm, $p = 0.95$ mm, $\epsilon_r = 3.5$, $\tan\delta = 0.004$, $l = 10$ mm.	43

3.15	Dispersion diagram showing the propagation of the fundamental mode and parallel plate modes within the PGGWG structure. The groove width $w = 5.48$ mm.	44
3.16	A cross-section of the PGGWG showing the E-field distribution of its fundamental propagating mode.	45
3.17	Dispersion diagram showing the propagation of the fundamental mode and with varying groove width w . Other dimensions kept constant are: $h = 0.508$ mm, $h_a = 0.106$ mm, $v_d = 0.3$ mm, $p_d = 0.9$ mm, $\epsilon_r = 3.5$, $\tan\delta = 0.004$, $l = 10$ mm.	46
3.18	Electric field distributions within the PGGWG at different frequency points of observation	47
3.19	3D view of the PGGWG structure excited with waveguide ports in CST	48
3.20	3D view of the PGGWG showing the E-field distribution of the TE ₁₀ mode excitation at the port plane.	49
3.21	S-parameter (dB) results of the PGGWG simulation with waveguide port excitation. The dimensions of the PGGWG are: $h = 0.508$ mm, $h_a = 0.106$ mm, $v_d = 0.3$ mm, $p_d = 0.7$ mm, $p = 0.95$, $w = 5.48$ mm, $\epsilon_r = 3.5$ and $\tan\delta = 0.004$	50
3.22	S_{21} (dB) of simulated PGGWG using waveguide ports and that of the stopband of an array of EBG unit cell embedded within parallel plates.	50
4.1	CPW to PGGWG transition with the prototype PGGWG circuit showing the top and bottom view attached to the end-launch connector.	54

4.2	The CPW to PGGWG transition implementation in CST. (a) Bottom view with the CPW coupling slot. (b) Top view with the end-connector attached. (c) 3D view of the CPW to PGGWG transition.	56
4.3	E-field and surface current plot of the CPW - PGGWG transition. (a) Quasi-TEM field in the CPW transition. (b) TE_{10} mode in the PGGWG. (c) Surface current along the bottom plane. (d) Surface current along the top plane.	56
4.4	Simulated S-parameters of the CPW-PGGWG transition over the band of interest	57
4.5	TRL error model	58
4.6	Schematic drawing of standard (a) Thru, (b) Line and (c) Reflect.	59
4.7	Stack-up used in the fabrication of the PGGWG.	60
4.8	Fabricated PGGWG TRL standards.	61
4.9	Microscopic picture showing the cross section of the fabricated circuit. (a) PGGWG circuit. (b) Cross section X-X'. (c) Cross section $X'_1-X'_1$	62
4.10	Experimental set-up for measuring the PGGWG circuits and TRL standards using the PNA-X N5247A network analyzer.	63
4.11	PGGWG simulation and measurement performance including the CPW-PGGWG transition of Figure 4.1.	64
4.12	PGGWG simulation and measurement of S-parameter magnitudes with the CPW-PGGWG transition de-embedded.	65
4.13	Transmission phase of the PGGWG simulation and measurement S-parameter magnitudes with the CPW-PGGWG transition de-embedded.	65

5.1	PGGWG transmission line of different lengths. (a) A section of the de-embedded PGGWG line length, l_1 . (b) A section of the de-embedded PGGWG line length, l_2	68
5.2	Fabricated prototype of the transmission lines. (a) PGGWG showing the bottom and top views with connector attachment. (b) SIW lines.	69
5.3	Attenuation constant(Np/m) of PGGWG and SIW	70
5.4	Phase constant (β /m) of PGGWG and SIW	71
5.5	Phase velocity (v_c/c) of PGGWG and SIW	71
5.6	Transmission line Q-factor of PGGWG and comparable SIW	72
5.7	Different PGGWG resonant cavity arrangements with electric field distributions. (a) Rectangular cavity. (b) Square cavity. (c) Circular cavity.	73
5.8	Resonant cavities with geometry layout, dimensions and magnitude of the electric field of the fundamental TE_{101} resonant mode (a) PGGWG rectangular cavity (b) SIW rectangular cavity.	76
5.9	Guided wavelength, λ_g , of PGGWG and comparable SIW, extracted from the phase constant of PGGWG and SIW.	77
5.10	S_{21} (dB) of the 2-port excitation for the weakly excited rectangular resonant cavities (a) PGGWG (b) SIW.	78
6.1	PGGWG rectangular resonant cavity structure showing the top and bottom of the cavity with the isolated floating metal patch on the top plane.	81
6.2	PGGWG rectangular resonant cavity. (a) Bottom view of the cavity. (b) Electric field vector plot inside the cavity from cross section view X-X'. (c) Magnitude of S_{21} (dB).	83

6.3	Illustration of the DC and RF paths in PGGWG and SIW	84
6.4	PGGWG rectangular resonant cavity structure. (a) Top view showing the connection of the varactor diode. (b) Bottom view.	87
6.5	SPICE model of the MACOM 46580-276 varactor diode.	87
6.6	Simulation results obtained using lumped element capacitance, C_o , applied to the PGGWG resonant cavity	88
6.7	3D EM-circuit Co-simulation set-up showing the equivalent circuit model for MACOM 46461-276 varactor diode connected.	89
6.8	EM co-simulation result of S_{21} (dB) of the 2-port loaded rectangular PGGWG cavity using the equivalent circuit model of MACOM 46580 varactor diode.	90
6.9	3D models of different PGGWG resonant cavities. (a) Square patch EBG implementation of a rectangular cavity. (b) Square resonant cavity with a round EBG patch implementation (c) Circular resonant cavity with a round EBG patch implementation.	91
6.10	EM co-simulation result of S_{21} (dB) of the PGGWG cavity using the equivalent circuit model of MACOM 46580 varactor diode. (a) Rectangular cavity with a square patch EBG implementation. (b) Square cavity. (c) Circular PGGWG cavity.	92
6.11	Fabricated PGGWG rectangular cavity with varactor diode inclusion.	94
6.12	Measured S_{21} (dB) of the PGGWG resonant cavity.	95
6.13	Cross section $X-X'$ and $X_1 - X'_1$ showing the microscopic image of the PGGWG sidewall and the cut through the fabricated circuit.	96

7.1	4-pole conceptual narrowband PGGWG tunable filter.(a) Cavity arrangement show the cavity length and inter-resonator coupling. (b) Center cavity post and catch pad. (c) Top view showing the varactor diode attachment to the top plate.	101
7.2	PGGWG resonance cavity. (a) PGGWG cavity with center conductor. (b) Top view of the cavity. (c) View of the center conductor and catch pad.	102
7.3	Conceptual layout of PGGWG VCO implementation	102

List of Tables

2.1	A qualitative comparison of the different tuning methods applied to SIW resonant cavities.	27
3.1	Suppression bandwidth of the EBG unit cell arrangement for varying relative permittivity ϵ_r , substrate thickness h and catch pad diameter p_d	42
4.1	Optimized dimensions for the CPW to PGGWG transition	55
5.1	Dimensions of PGGWG resonant cavities	74
5.2	Dimensions of the rectangular resonant cavities in PGGWG and SIW	77
5.3	Q-factor comparison between PGGWG and SIW from rectangular resonant cavities implemented using the same substrate material and identical stackup	79
6.1	Dimensions of the tunable PGGWG rectangular resonant cavity	82
6.2	Q-factor comparison between different resonant cavities	93
6.3	A comparison between simulated and measured results of the tunable K_a -band resonant cavity.	95

List of Acronyms

AMC	Artificial Magnetic Conductors.
CPW	Coplanar Waveguide.
CR	Cognitive Radio.
CSIW	Corrugated Substrate Integrated Waveguide.
DESIW	Decoupled Empty SIW.
EBG	Electromagnetic Band Gap.
FSIW	Folded Substrate Integrated Waveguide.
FSIW	Ridged Substrate Integrated Waveguide.
GCPW	Grounded Coplanar Waveguide.
GGWG	Groove Gap Waveguide.
GW	Gap Waveguide.
HMSIW	Half Mode Substrate Integrated Waveguide.
MGW	Microstrip Gap Waveguides.
MMIC	Monolithic Microwave Integrated Circuit.
NR	New Radio.
PEC	Perfect Electrical Conductor.
PGGWG	Planar Groove Gap Waveguide.
PMC	Perfect Magnetic Conductor.
PRGW	Printed Ridge Gap Waveguide.
RGW	Ridge Gap Waveguide.
SIW	Substrate Integrated Waveguide.
TE	Transverse Electric.
TEM	Transverse Electric Magnetic.
TM	Transverse Magnetic.

VCO Voltage Controlled Oscillator.

Chapter 1

Introduction

Planar waveguide technology has, in recent times, been in the forefront of millimeter wave research. The need for implementations of waveguides with ease of fabrication and the ability to integrate with planar circuitry has led to intensive research and development of planar waveguide technologies [1]. Planar waveguide topologies provide size reduction compared to metallic waveguides and allow for different miniaturization techniques to further reduce the size of transmission line elements used in the design of filters, antennas and oscillators in millimeter wave systems [2].

The integration of multi-band functionality and coexistence of multiple standards into a single wireless device has resulted in significant research interest in frequency agile as well as miniaturized front-end components [3]. Compared to the classical filter banks in a telecommunication receiver systems, frequency agile filters that tune to different frequency bands have the advantage of reduced system size and complexity. This is important for the integration in highly compact and portable wireless devices [4].

Frequency agile planar passive devices [5] can be used in multi-band transceivers, **Cognitive Radio (CR)** systems, wide-band radars and satellite payloads [4]. Several of the proposed 5G **New Radio (NR)** bands are located in the K_a -band (26.5 - 40 GHz). It is envisaged that 5G communication front-haul networking will make

extensive use of K_a -band channels [6]. To achieve greater flexibility in system design, frequency agility in the front-end components would be advantageous.

At millimeter wave frequencies, planar waveguide structures such as the Substrate Integrated Waveguide (SIW) are often preferred to planar transmission lines such as microstrip lines [7]. This is because at millimeter wave frequencies, microstrip lines are prone to radiation loss [1]. The development of SIW, which is a direct planar derivative of the metallic rectangular waveguide, allows for the development of frequency agile millimeter wave components such as voltage controlled oscillators [4], millimeter wave bandpass filters [7] and antennas [4], [8] amongst others. However, due to the lack of DC isolation between the top and bottom conducting planes of SIW [9], bridging wires or multi-layer routing is often required for the biasing of active devices.

A recently developed waveguide referred to as GGWG [10] provides DC isolated upper conducting plane, which can be advantageous in biasing of active devices in frequency agile applications. It is therefore of interest in this work to develop a planar variant of the GGWG and explore the DC isolated planes with a tunable resonant cavity.

1.1 Background

Planar varieties of machined waveguide media offer a compromise between price and performance compared to traditional planar transmission lines such as microstrip and Coplanar Waveguide (CPW) [1]. The equivalents of conventional rectangular [11] and ridged waveguide [12] have been reproduced in PCB technology using SIW technologies [13]. SIW consist of a planar dielectric substrate with top and bottom metal layers perforated with metallized holes as seen in Figure 1.1. SIW is compact, low loss, flexible, and provides a cheaper solution for integrating active circuits and passive components on the same substrate [13, 14, 15, 16].

SIW exhibits propagation characteristics similar to conventional rectangular

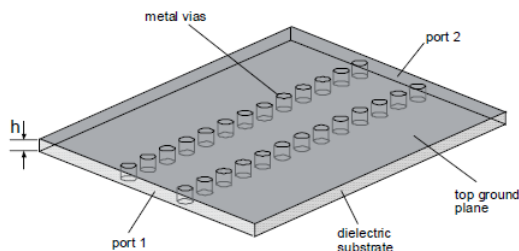


Figure 1.1: SIW topology. Taken from [14], © 2009 Radioengineering.

waveguide [1], allowing for empirical dimensional equivalent formulas between SIW and a conventional rectangular waveguide to be developed [13]. The geometry of the SIW structure allows for the propagation of **Transverse Electric (TE)** propagating modes, similar to that in a rectangular waveguide, but not **Transverse Magnetic (TM)** modes. This is due to continuous side walls in rectangular waveguide being replaced with metalized via holes in SIW [13].

Different variations of SIW have emerged from various miniaturization techniques, including **Folded Substrate Integrated Waveguide (FSIW)** [17,18], **Ridged Substrate Integrated Waveguide (RSIW)** [19] and the **Half Mode Substrate Integrated Waveguide (HMSIW)** [20].

The FSIW [17, 18] is derived by folding the sides of the SIW underneath the central part as seen in Figure 1.2(a). This method reduces the effective width of the waveguide; however, the thickness of the FSIW is twice that of the SIW. The RSIW (Figure 1.2(b)), on the other hand, is similar to SIW but has a centre row of vias along the waveguide. These vias are such that one end of the via is connected to the bottom layer of the waveguide while the other end is embedded in the substrate [17]. Compared to SIW, RSIW is more compact [17]. By having the metal strip, mode-spacing between the fundamental mode and the second mode can be increased, thus increasing the bandwidth over which the waveguide can function effectively.

FSIW and RSIW can also be used in combination to reduce the size of the waveguide [18]. An example of a filter implementation that exploits the use of both topologies to achieve miniaturization is an evanescent mode filter presented

in [21].

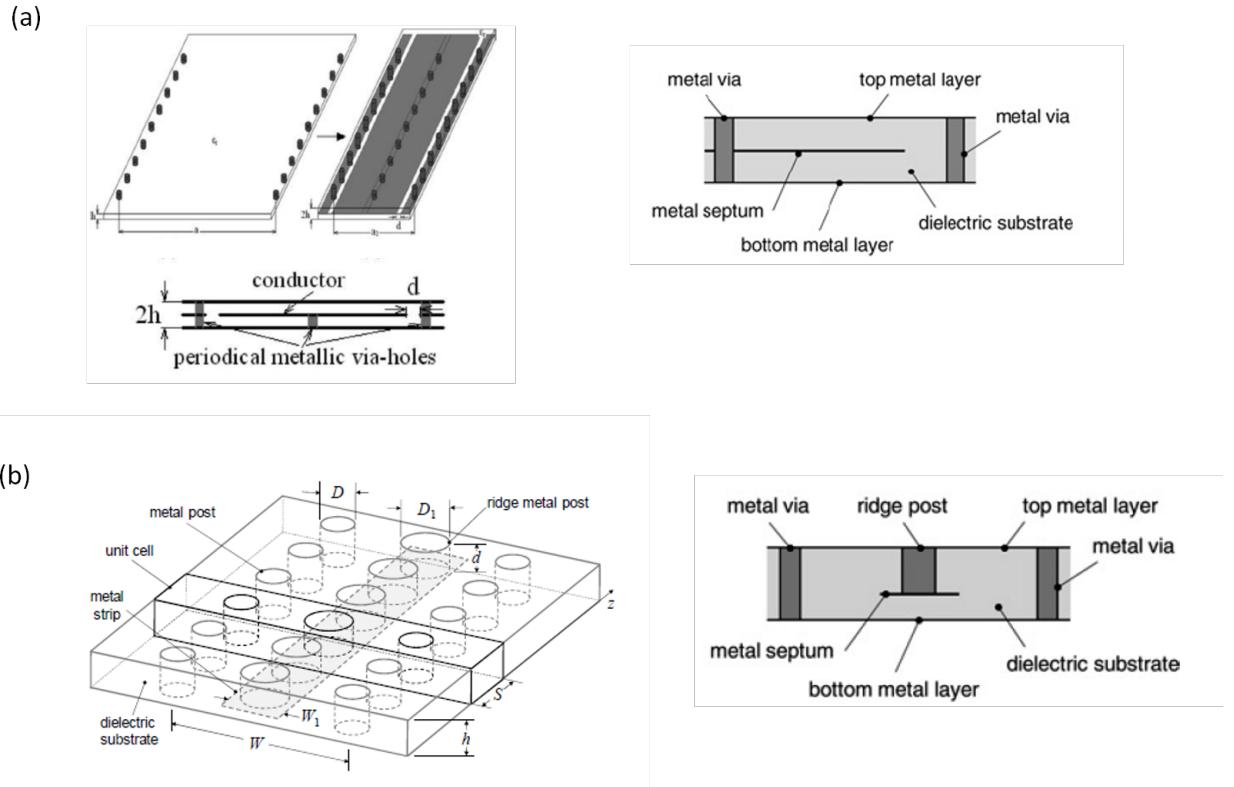


Figure 1.2: Variants of SIW (a) FSIW. Taken from [22], © 2012 IEEE, [1], © 2011 IEEE. (b) RSIW. Taken from [17], © 2009 IEEE, [1], © 2011 IEEE

The HMSIW is achieved by cutting the SIW in half along the transverse plane [20]. By enforcing an open boundary along the symmetry plane, the open wall acts like an effective magnetic wall. By placing a magnetic boundary condition along the symmetric (transverse) plane, the half-mode SIW will be able to keep half of the dominant propagating mode TE_{10} field unchanged [23], [24].

The integration of SIW circuits with active components requires DC-biasing but, the metallic vias causes an inherent DC short-circuit between top and bottom plane of the waveguide [9], [25]. This problem led to the development of the [Corrugated Substrate Integrated Waveguide \(CSIW\)](#) [9] which eliminates the use of metallic post.

Figure 1.3 shows the geometry of the CSIW topology [9]. The CSIW structure is etched on a top conductor of a substrate height h . The open-circuited quarter-wavelength stubs row acts as an electric sidewall similar to the conducting vias in the SIW structure, but does not require conducting vias to achieve the required boundary conditions at the side wall. This topology also supports the TE_{10} mode of propagation similar to SIW.

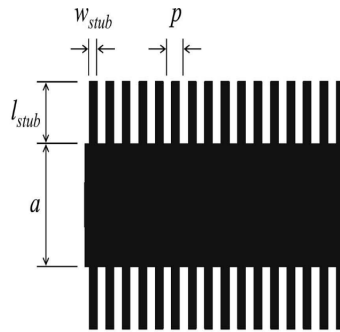


Figure 1.3: Top conductor layout of Corrugated Substrate Integrated Waveguide topology. Taken from [9], © 2012 IEEE.

However, a constraint to this topology is its narrow usable passband compared to SIW. The mode spacing of the TE_{10} and TE_{20} of the CSIW is less than in SIW. This is because the stub admittance varies with increasing frequency; the short-circuit positions move, thereby increasing the effective width of the waveguide. Also, this topology has no cut-off frequency and spurious modes can propagate [9].

A recently developed [Decoupled Empty SIW \(DESIW\)](#) structure [26] (as shown in Figure 1.4) enables AC/DC decoupling, which is beneficial in biasing of active devices in the manufacturing of frequency agile and reconfigurable devices. This structure is developed in three different layers: the top and bottom conducting planes, and the middle layer which forms the body of the waveguide. In Order for there to be continuous electric contact, the top and bottom metal layers (Figure 1.4(a) and(b))are soldered to the main body of the line (Figure 1.4(c)). Although the structure is AC/DC decoupled, it is not entirely manufactured in a PCB process and therefore presents a challenge with the integration of other planar circuitry.

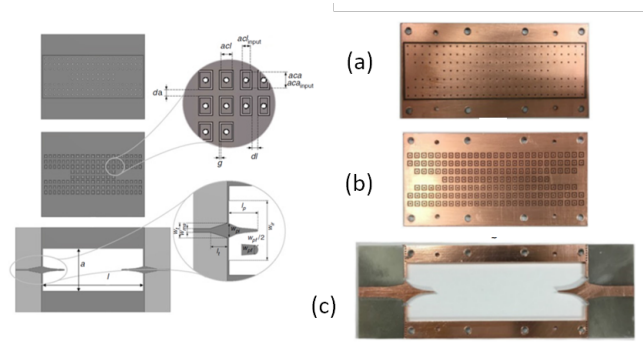


Figure 1.4: Decoupled empty SIW. (a) Top view of the top cover. (b) Bottom view of the top cover. (c) Top view of the body of the line. Taken from [26], © 2017 IET.

Other variants of SIW include the slow-wave SIW (SW-SIW) [27] (Figure 1.5). This is obtained by placing several metalized blind vias within the cavity of the SIW structure to concentrate the electric field above the embedded vias and the top metal plate. As a result, the SW-SIW exhibits a high per unit length distributed capacitance which reduces the transversal and longitudinal dimensions of the structure. It is reported that up to 40% reduction in the longitudinal dimension can be obtained [27]. This, however, still places the top and bottom conductor of the SW-SIW at the same DC potential. Although a reduction in size is obtained, frequency agile application using this structure will require isolation of the DC path for the biasing of active devices.

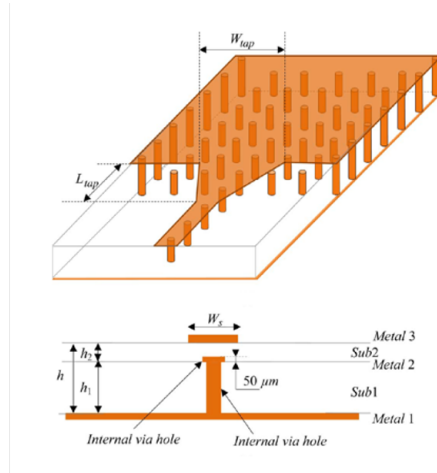


Figure 1.5: Schematic diagram of the Slow-Wave SIW. Taken from [27], © 2014 IEEE.

Another planar waveguide which has been proposed recently is developed from the [Gap Waveguide \(GW\)](#). This uses [Artificial Magnetic Conductors \(AMC\)](#) within parallel plate conductors to create a contact-less waveguide medium and it is shown in Figure 1.6. The [Printed Ridge Gap Waveguide \(PRGW\)](#) in Figure 1.6(a) utilizes a double-ridge waveguide layout, replacing the upper conductor with an AMC surface [28]. The ridge is therefore surrounded by the AMC surfaces in the upper and lower sides of the structure. This enables the propagation of a [Transverse Electric Magnetic \(TEM\)](#) transmission mode along the ridge. Although this was implemented on planar substrate with the use of fasteners to hold the pieces together, the medium is made up of individual pieces which increases the probability of assembly errors. The top and bottom plates are, however, DC isolated, but the structure does not make use of the groove width within the GGWG and does not support transverse electric propagating modes.

In Figure 1.6(b), a TEM transmission line included in GW structure and implemented entirely in a multi-layer PCB process is demonstrated. The AMC within the parallel plates are used to enforce a parallel plate mode cut-off thus allowing for a quasi-TEM mode to exist along the ridge supported with metalized vias along the groove of the waveguide.

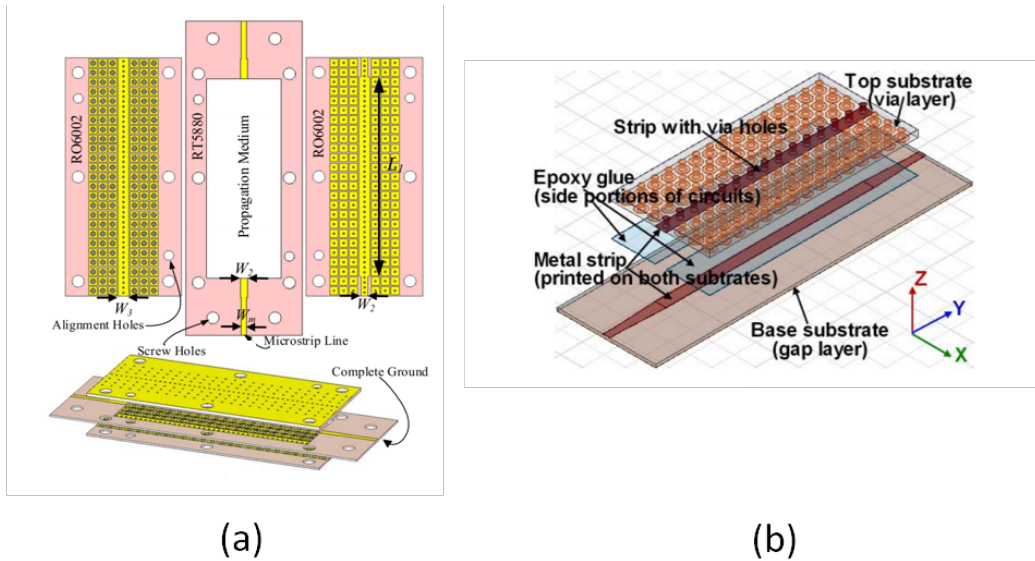


Figure 1.6: Planar waveguides derived from the gap waveguide. (a) Printed Ridge Gap Waveguide. Taken from [28], © 2018 IEEE. (b) Substrate Integrated Gap Waveguide. Taken from [29], © 2016 IEEE.

For frequency agile applications, DC isolation between the conducting planes is desirable to bias active devices such as varactor diodes. In current frequency agile applications using the SIW topology, bridging wires [30] or multiple cuts [31] on the structure are required to create DC isolation between the diode contact terminals.

1.2 Problem Statement

Planar integration media provide numerous advantages over machined metallic waveguide, including low production cost and small size. SIW, as the most popular planar medium, has been used extensively for the design of passive and frequency agile front-end microwave components. However, due to the lack of DC isolation between the top and bottom conducting planes of SIW, bridging wires or multi-layer routing is required to connect the DC bias lines to the active device

which complicates the implementation of frequency agile front-end components.

The research question is therefore:

Is it possible to develop a planar waveguide medium derived from the gap groove waveguide using the hollow groove width between Artificial Magnetic Conducting sidewalls in an all PCB implementation having DC isolated conducting plate

1.3 Objectives of Research

This dissertation proposes a planar waveguide implementation referred to as Planar Groove Gap Waveguide (PGGWG). This is derived from the micro-machined GGWG but manufactured in a multi-layer PCB process.

The objectives of this research are as outlined as follows:

- Develop a new planar waveguide structure based on the GGWG. The machined GGWG offers DC isolated ground plates making it advantageous in frequency agile application.
- Develop a wideband transition to excite the dominant propagating mode of the PGGWG structure while maintaining the DC isolation properties of the structure.
- Characterise the PGGWG propagation constant (phase and attenuation constant) and directly compare to SIW on the same substrate and over the same frequency range.
- Characterise different PGGWG resonant cavities and compare the unloaded quality factor obtained to that of SIW.
- Develop and demonstrate a tunable cavity in PGGWG, illustrating the benefits of DC isolation.

1.4 Original Contributions

- A novel broadband planar waveguide structure with two DC isolation planes. This planar waveguide medium has propagation characteristics comparable to SIW as demonstrated in this work.
- A CPW feed network that maintains the DC isolation.
- Experimental validation of the medium's broadband propagation characteristics and narrowband cavity resonance properties.
- A simple DC biasing scheme for biasing tunable PGGWG resonant cavities, with experimental validation.

1.5 Publications

The published research outputs from this thesis are listed below.

- T. Oyedokun, R. Geschke and T. Stander, "Experimental characterisation of planar groove gap waveguide and cavity," *2017 47th European Microwave Conference (EuMC)*, Nuremberg, 2017, pp. 436-439.
- T. Oyedokun, R. Geschke and T. Stander, "A tunable Ka-band planar groove gap waveguide resonant cavity," *2017 IEEE Radio and Antenna Days of the Indian Ocean (RADIO)*, Cape Town, 2017, pp. 1-2.
- T. Oyedokun, R. Geschke, and T. Stander, (2018). "A Geometric Study of Tunable Planar Groove Gap Waveguide Cavities." *IOP Conference Series: Materials Science and Engineering* 321(1): 012008.

1.6 Outline of the Thesis

Chapter 2 presents a brief review of the conventional metallic rectangular waveguide structure. This is followed by the theory and operation of the gap waveguide,

its implementation, advantages as well as the different variants of the waveguide that can be obtained. Electromagnetic bandgap structures as used in the GW are also discussed. A review of GGWG, highlighting its advantages and the potential benefits of a novel planar implementation of this waveguide, is presented.

Chapter 3 presents the proposed PGGWG structure with detailed design guidelines and numerical analysis of the structure. The dispersion diagram of the waveguide is presented to show the fundamental TE_{10} propagating mode. The simulated S-parameters of the PGGWG using waveguide ports are also presented.

A wideband CPW to PGGWG transition used to excite the PGGWG is implemented in Chapter 4. Simulation results, as well as fabrication procedure and measurements results of the waveguide are also presented.

Further analysis of the waveguide is presented in Chapter 5. This presents the propagation constant (phase and attenuation) analysis of the PGGWG in direct comparison to SIW. A resonant cavity in PGGWG is characterized with its unloaded quality factor compared to that of SIW cavity.

Chapter 6 presents a tunable K_a -band PGGWG resonant cavity with detail analysis of the cavity geometry. The DC-biasing scheme applied to a varactor diode highlighting the benefits of the DC isolation of PGGWG, is also presented. Measurement results of the prototype is presented with a comparison of the unloaded Q-factor between measured and simulated result.

Chapter 7 draw conclusions from the development of the new planar waveguide media, highlighting the advantages the structure has over existing SIW planar media. This chapter concludes with a discussion of future work.

Chapter 2

Literature Review

2.1 Introduction

A brief review of the rectangular waveguide is presented with its geometry and dimensions. This is followed by a review of the basic theory of the Gap Waveguide (GW) technology. The different variations of the GW such as the Groove Gap Waveguide (GGWG), Gap Ridge Waveguide (GRW) and Microstrip Gap Waveguide (MGW) are presented with dimensions of the design and operation of each. Various millimeter wave front-end applications using the GW technology are also discussed, highlighting the advantage of the GW over conventional rectangular waveguide.

[Electromagnetic Band Gap \(EBG\)](#) structures, as employed in the GW technology, are reviewed. The implementation of the EBG cell within parallel plate waveguide as well as planar implementation on multi layer dielectric substrate material, are also discussed.

This chapter concludes with a review of the various approaches by which frequency agility using SIW are obtained. A summary of the current solutions is presented, highlighting the need for a planar waveguide with DC isolated planes for frequency agile applications.

2.2 Rectangular Waveguide

Waveguides are guided media, often made from hollow metal pipes, that guide the propagation of electromagnetic waves [11]. They are of two types in general: rectangular waveguide and circular waveguide [11].

In microwave systems, such as communication links and radars, waveguides form an integral part of the system [32]. RF components such as couplers [33], filters [34] and circulators [35] are also designed using waveguides. This is mainly because waveguides provides high power handling capabilities and present low loss [11] .

The diagram of the rectangular waveguide as shown in Figure 2.1 is a metallic pipe with dimensions a and b ; the width and height of the waveguide respectively.

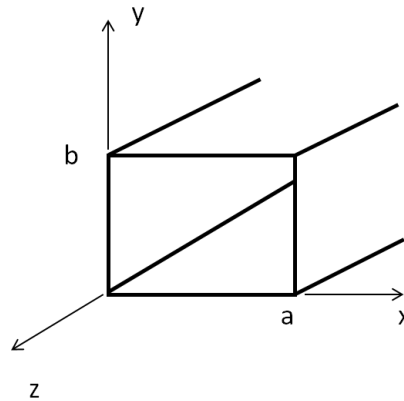


Figure 2.1: Geometry of the Rectangular Waveguide.

Rectangular waveguide allows for the propagation of TE and TM propagating modes. The TE modes are electromagnetic waves such that the electric field component in the direction of propagation, $\overline{E}_z = 0$ while the magnetic field component in the direction of propagation $\overline{M}_z \neq 0$. TM modes on the other hand, the magnetic field component $\overline{E}_z = 0$ while electric field component, $\overline{E}_z \neq 0$ [11].

The rectangular waveguide has a cut-off frequency which is calculated by;

$$f_c = \frac{c}{2\pi\sqrt{\epsilon_r}} \sqrt{\left(\frac{m\pi}{a}\right)^2 + \left(\frac{n\pi}{b}\right)^2} \quad (2.1)$$

The manufacturing process of the rectangular waveguide requires high precision to ensure electric contact between the top conducting plate and the electric sidewalls. At millimeter wave frequencies, the wavelength is inevitably small and thus increases the manufacturing complexity of RF front-end components at such frequencies [36] [37]. These challenges lead to the development of the GW [36].

The geometry of the rectangular waveguide consist of one hollow metallic structure that is not DC isolated. Similarly, SIW as direct derivative of the rectangular waveguide as discussed in Section 1.1, uses plated holes for the sidewalls.

2.3 Gap Waveguide Technology

GW technology has, over the last decade attracted much research interest, especially in the design of low-loss circuits at millimeter and sub-millimeter wave frequencies [36, 38, 39]. This technology, initially proposed in [40], exploits the periodic 'texture' of metal-materials, which create a high impedance surface that inhibit local traveling waves between two parallel plate waveguide guide [40].

In parallel plate waveguide, as shown in Figure 2.2(a), parallel plate modes between the **Perfect Electrical Conductor (PEC)** and **Perfect Magnetic Conductor (PMC)** plates will not propagate if the separation distance h , between the PEC and PMC plates is less than a quarter wavelength. If, however, the bottom PEC plate is surrounded by a PMC as shown in Figure 2.2(b), then a TEM mode will propagate in the gap between the two PEC layers [36]. As a result of this phenomenon, the GW was introduced [41].

The basic geometry of the GW is presented in Figure 2.3. The GW consist of

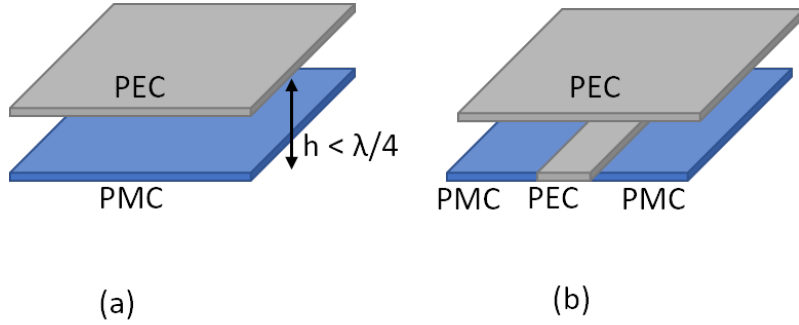


Figure 2.2: Operating principle of the GW. (a) PEC and PMC plate at a distance h apart. (b) Bottom PEC plate embedded by a PMC on both sides. Adapted from [41].

two parallel PEC conducting surfaces. One of the plates is filled with periodic textured EBG unit cells creating an AMC surface while the other is placed above the AMC surface separated by an air gap. The dimensions as shown are as follows: p is the pitch between adjacent EBG pin, w is width of the EBG pin, h is the height of the EBG pin, h_a is the height of the air gap between the textured surface and the top PEC plate. Based on the geometry of the EBG unit cell, a lower and upper frequency stopband can be identified within the parallel propagating mode.

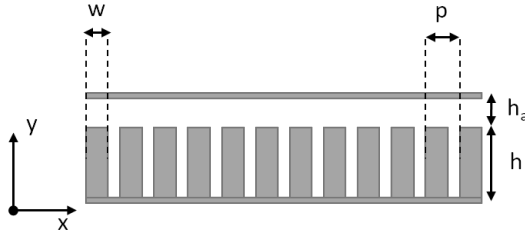


Figure 2.3: A cross section of the GW [36].

As opposed to the conventional rectangular waveguide, the top and bottom plate of the GW structure are isolated with no electric contact between the plates. The design of the GW avoids the unwanted radiation which may occur in standard waveguide flanges [41], and circumvents the problem of high contact resistance seam. This unique property of the GW makes a very attractive waveguide media

[40].

The stopband of the parallel plate mode in GW can be exploited for packaging of both passive and active microwave circuits [42, 43]. This is done to avoid resonant modes, as demonstrated in microstrip lines in [44], and also in baluns of active microstrip circuits with [Monolithic Microwave Integrated Circuit \(MMIC\)](#) amplifier chains in [43].

Some applications of GW in microwave component design include GW power dividers [45], packaging of SIW filters [42], packaging of microstrip filters [46] and microstrip antennas [47].

There are three different major configuration of the GW namely; [Ridge Gap Waveguide \(RGW\)](#) [39], [GGWG](#) (which can use either horizontal and vertical polarization [38], [48]) and [Microstrip Gap Waveguides \(MGW\)](#) [49], [50].

2.4 Artificial Magnetic Conductors and Electromagnetic Bandgaps

Electromagnetic bandgap structures are employed in the design of the GW [51]. The ability to create metamaterial surfaces that can generate magnetic conductivity artificially known as artificial magnetic conductor (AMC), led to the development of soft and hard surfaces [52].

The ideal soft and hard surface can be described in terms of PMC and PEC strips [53]. This is a grid of parallel strips, with an interchange between PEC and PMC, as illustrated in Figure 2.4 [53]. The strips have anisotropic boundary conditions allowing for the propagation of surface waves along the strips (hard surface) and prohibiting waves in other directions along the surface orthogonal to the strips (soft surface) [54]. This soft and hard surfaces could also be in effect created by using PEC and PMC strips on a grounded PCB [55].

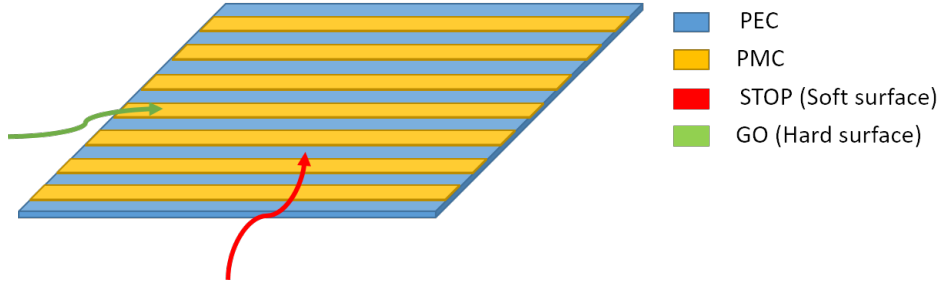


Figure 2.4: PEC/PMC strip representing an ideal soft and hard surfaces. The red and green arrows represent the direction of propagation of the waves of the soft and hard surface respectively. Adapted from [53], © 2003 ACES.

EBG's are used in the GW to create an AMC surface [56]. The EBG unit cells are design to suppress the propagation of parallel plate modes between the AMC surface and a top PEC plate with the top PEC plate placed at a distance less than a quarter wavelength above the AMC [36]. The EBG surface employed in the GW can be of different shapes and types. The most commonly used in literature are the periodic metal pins (Bed of nails) [57] and mushroom-type EBG textures [56] shown in Figure 2.5. The mushroom-type EBG surfaces are periodic metallic patches connected to a reference plane through shorted stubs or plated through-holes in the case of a dielectric inclusion. The bed of nails are also connected to the reference plane [56] but without a wider connecting pad at the top.

The geometrical features of the EBG unit cell are directly related to the frequency range of the stopband [58]. These parameters include the size of individual catch pads in the case of the mushroom-type EBG, the gap between adjacent catch pads g , the diameter of stubs (vias), and the height, d of the EBG inclusion. The height of the pin, d as depicted in Figure 2.5, is chosen to be less than $\lambda/4$ at the centre frequency of the unit cell stop band. This is to transform the short circuit (PEC) to an open circuit (PMC) at the upper plate. The air gap height h is also chosen to be smaller than $\lambda/4$. Studies on the achievable bandgap of these EBG unit cells have been presented in [56].

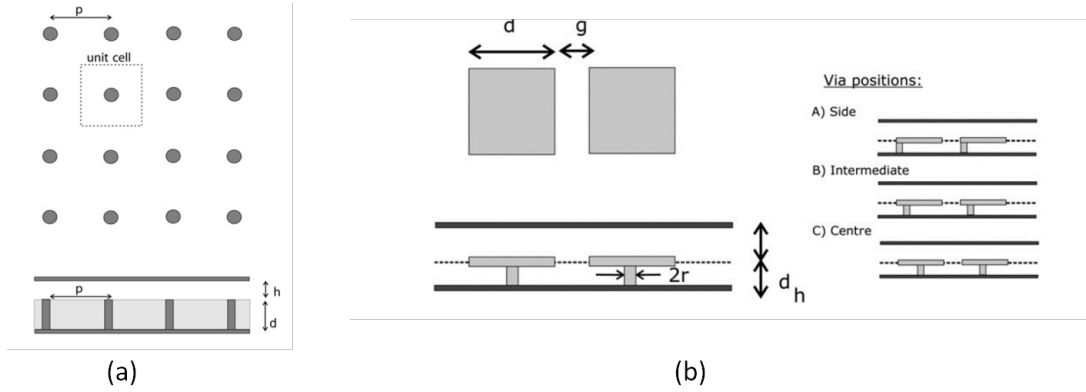


Figure 2.5: Geometry of pin lattice and mushroom-type EBG layers realised within parallel-plate waveguide. (a) Bed of nails arrangement. (b) Mushroom-type arrangement with the catch pad. Taken from [56], © 2011 IET.

The mushroom-type can also be realized in PCB technology where the catch pad is grounded to the bottom metal plate using metallised via holes as illustrated in Figure 2.6(a) [53]. The frequency stopband is determined by the width of the catch pad, the height of the substrate, h and the relative permittivity, ϵ_r of the substrate material used. The height $h = \lambda_0/4(\sqrt{\epsilon_{eff}})$ is related to the guided wavelength of the medium. This allows for a compact implementation of the EBG structure [53]. The catch pad acts as a resonant parallel LC circuit with L representing the inductance of the via and C , the capacitance between the ground plane and the catch pad. At resonance, the surface impedance is approximately the same as the impedance of the LC circuit, thereby, thereby creating the high impedance mushroom surface [51], [58].

Figure 2.6(b) shows the embedded mushroom-type EBG within parallel plate. The catch pad is embedded between two metallic layers, with the catch pad grounded to one of the plates using metalized vias. The dielectric substrate material used for height h and h_a could either be of different relative permittivity or the same. The frequency stopband created by a unit cell can be examined by the dispersion diagram of the unit cell [58].

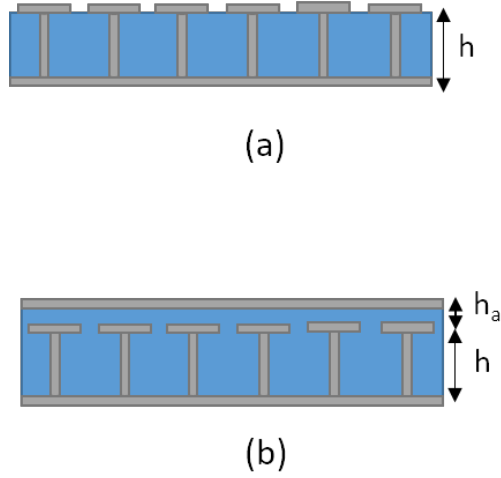


Figure 2.6: Geometry of mushroom-type EBG realised within on multi layer PCB process. (a) EBG consisting of a catch pad and via to ground. (b) Embedded EBG within the parallel plate. Adapted from [58].

2.5 Groove Gap Waveguide

The GGWG [10] as shown in Figure 2.7 is a variant of the GW [40]. Its structure is formed by placing rows of EBG unit cells on either side of a groove of width w . Parallel plate modes above the AMC surface are suppressed creating a frequency stopband. This is made possible if the air gap between the upper conducting plate and the surface of the AMC is smaller than $\lambda_g/4$ at the centre of the operating frequency band [10].

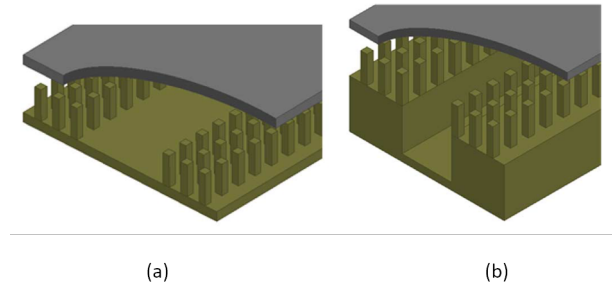


Figure 2.7: Cross section of the GGWG for (a) Horizontal and (b) Vertical polarisation. Taken from [48], © 2015 IEEE.

The key geometrical parameters used in controlling the stopband are the height of the air gap, h_a , the height, h of the EBG pin and the size of the pins, d . By numerical analysis on an EBG unit cell, the stopband created by the EBGs in the GGWG can be determined [38].

The groove allows for the propagation of the TE_{10} mode [48] similar to that in conventional rectangular waveguide as well as its planar variant, SIW [1]. Figure 2.8(a) shows a cross section of the GGWG for horizontal polarization. Figure 2.8(b) shows the 3D view of the GGWG with the field distribution of the fundamental mode in Figure 2.8(c).

GGWG is dispersive, similar to rectangular waveguide. However, unlike rectangular waveguide, the cut-off frequency of the fundamental TE_{10} propagating mode of the GGWG falls within the suppression band of the parallel plate mode and by controlling the width of the groove a , the cut-off of the fundamental mode can be shifted [48]. This is in contrast to [60], where the band gap structure is used to enforce an open boundary at the sidewalls, leading to the propagation of a parallel plate TEM mode.

An advantage GGWG has over rectangular waveguide is that there is no electrical contact between the upper and lower plates constituting the waveguide [38]. Conventional rectangular waveguide requires good electric contact between the adjoining metal pieces if the roof of the waveguide is attached to the sidewalls after manufacturing [38]. In GGWG, on the other hand, the metal plates are

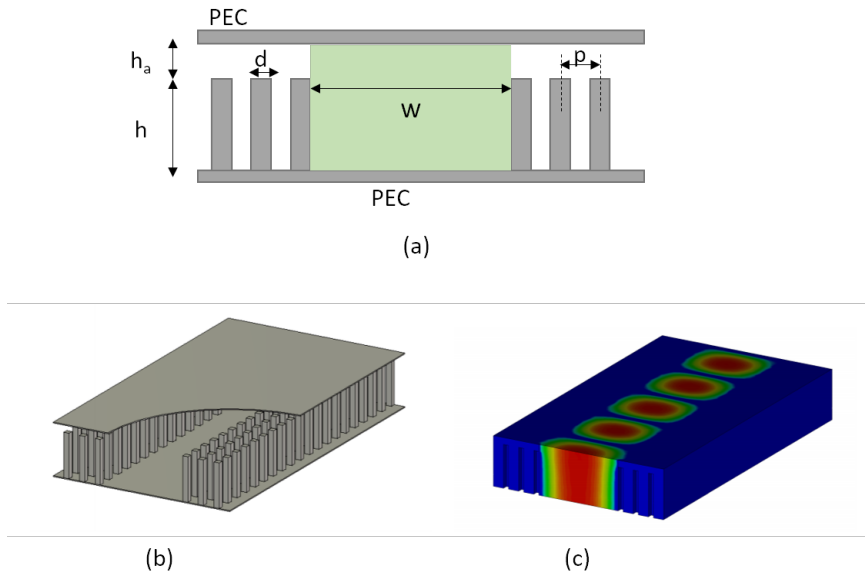


Figure 2.8: Cross section of the GGWG for horizontal polarization. (a) Cross section of the GGWG for horizontal polarization. (b) 3D view showing the groove within the GGWG [59]. (c) E-field distribution within the groove [59].

not in physical contact, posing fewer assembly challenges [38, 61].

A bandpass filter using GGWG at K_a band was designed in [61]. A fractional bandwidth of 2.5% was achieved. The Q-factors of GGWG and rectangular waveguide are very similar. It was reported that, although the loss in GGWG is slightly higher than in rectangular waveguide, it was better than in MGW and in the RGW [61].

In [62], a narrow band filter using the GGWG was designed and reported to have lower insertion loss than other rectangular waveguide bandpass filters at V-band. More bandpass filters at millimeter wave frequencies using GW are also reported in [63, 64].

2.6 Ridge Gap Waveguide

The RGW [59], as shown in Figure 2.9, consist of a metallic ridge of width w on the same plane as the AMC surface of the GW assembly. With the ridge in place, a propagation channel is created between the ridge top and the top metal PEC plate. At the sides, the AMC sidewalls suppress the parallel plate modes, allowing a local quasi-TEM mode to propagating along the ridge [39].

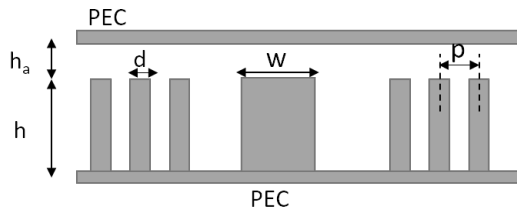


Figure 2.9: Cross section of the RGW with E-field of the fundamental propagating mode [59].

Although some modifications can be made, generally, the ridge has the same height as the pins [39]. The dimensions of the RGW are similar to that of the GW. The height of the EBG unit cell h , is chosen to be less than $\lambda/4$. The air gap height, h_a is also kept at less than $\lambda/4$ at the centre frequency of the stopband. The EBG unit cell is designed to ensure that the frequency stopband of the parallel plate mode is at the desired frequency range. The width, w of the ridge can be varied to achieve the desired characteristic impedance [65].

The ridge can take on any shape, including bends and branches, because the fields follows the path of the ridge. This has been demonstrated in passive components such as a branch line coupler [66], power divider [65] and microwave filter [67].

2.7 Microstrip Gap Waveguide

Another application of GW techniques is to lunch a TEM transmission line mode within the air gap above the AMC texture surface and the top metal PEC plate.

Since the GW allows a quasi-TEM mode in the gap between parallel metal plates, the geometry allows for the realization of an inverted microstrip line to be inserted within this gap as shown in Figure 2.10. This is referred to as microstrip gap waveguide (MGW) [50], [49].

The bed of nails can be replaced with a mushroom-type AMC implemented on PCB [68]. An air gap is created between the microstrip patches and the top cover plate. It was reported in [69] that the suspended MGW has lower insertion loss than the conventional microstrip line implemented on PCB. This is due to the propagation of the quasi-TEM mode in the air gap as opposed to propagation within substrate. The air gap also ensures lower dielectric losses [50]. In addition, it is also possible to use wider strip width for impedance matching [68].

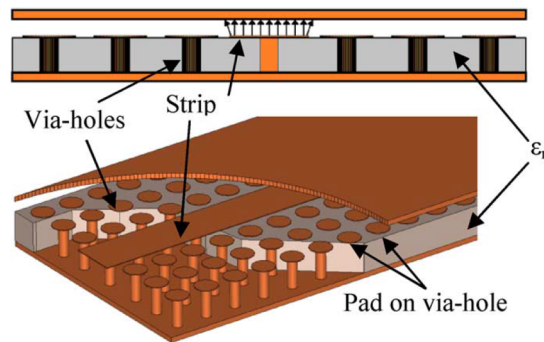


Figure 2.10: Cross section of the suspended microstrip line within the GW. Taken from [68], © 2014 IEEE.

There are different versions of the MGW reported in literature, differentiated by the AMC geometry adopted [50]. In Figure 2.11(a), the EBG structure is used to support the dielectric substrate on which the microstrip is etched. In Figure 2.11(b), the microstrip line is placed above the mushroom-type EBG surface with a substrate thickness t between the EBG surface and the microstrip line. In Figure 2.11(c), the microstrip line is implemented on the same layer as the mushroom-type EBG [70].

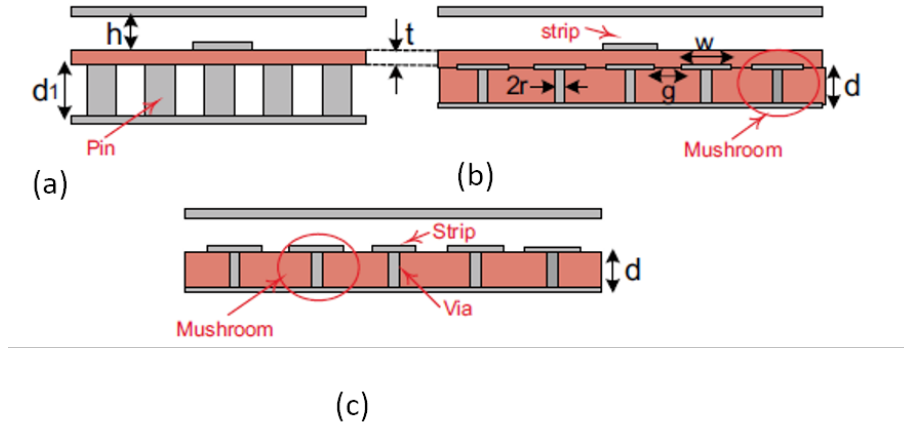


Figure 2.11: Cross section of the different microstrip line implementation within the GW. Taken from [50], © 2011 IEEE.

Analysis have been performed to determine the achievable bandwidth in [69]. It was found that the bandwidth is mostly determined by the air gap, h and the height, d_1 of the metallic pins in Figure 2.11(a). However, in the case of the microstrip implemented on the same substrate layer as the EBG (Figure 2.11(c)), the size of the mushroom catch pads affect the achievable bandwidth in addition to the air gap and the substrate thickness [68]. The MRG has been used in a slot array antenna [71] and recently in a PCB implementation [29].

2.8 Tunable Substrate Integrated Waveguide Structures

Frequency agility plays an important role in a dynamic receiver system [4]. The ability to control the frequency response of a component is often beneficial and provides the flexibility of post-fabrication fine-tuning in addition to the advantage of reconfigurability of the band in the case of a bandpass microwave filters [15, 30, 31, 72].

SIW, among the other planar transmission media, has a high-Q continuous tuning

range with varactor loaded cavities [4]. This has been demonstrated for [Voltage Controlled Oscillator \(VCO\)](#) [4], SIW tunable antennas [8] and bandpass microwave filters [31]. Frequency agility has also been demonstrated in microstrip technology using varactor diodes [3]; however, for millimeter wave applications, microstrip technology becomes less desirable due to radiation losses.

By changing the frequency response of one or more cavities, either by using varactor diodes [31], RF-MEMS switches [73] or PIN diodes [15] the centre frequency of the bandpass filter can be reconfigured [4]. However, there is often a compromise between the tuning range and the quality factor of the resonator, with the quality factor of the resonator reduced by a wider tuning range [4].

In [8], a tuning method was proposed for an SIW cavity oscillator. An opening at the side of the SIW cavity is created. This allows for a varactor diode to be coupled to the cavity. The loading effect of the diode is applied at maximum E-field distribution in the cavity to change the frequency response. This method reportedly offers approximately 2% tuning range.

Another method proposed in [31], and commonly used in the tuning of SIW filters [74] is inserting a metallized via post in the centre of the cavity connected to a metallized floating patch. This floating centre metallic patch (Figure 2.12) is used to load the centre via post with a varactor diode. By varying the capacitance between the floating metal patch and the top conductor of the SIW with a varactor diode, the capacitive loading in the cavity is perturbed. This creates a cavity with static capacitive loading which can be dynamically controlled, thereby creating a shift in the resonant frequency. This method often requires multiple cuts or bridging wires as shown in Figure 2.12 to separate the SIW planes for DC biasing of the varactor diode [30, 31, 75, 76].

The geometrical arrangement of SIW does not allow for DC isolation between the top and bottom plates. This often complicates the DC biasing of active devices such as varactor diodes [9].

The concept of magnetic tuning using ferrite has also been explored with SIW [77]. Due to the fact that the magnetic field of the fundamental mode is at

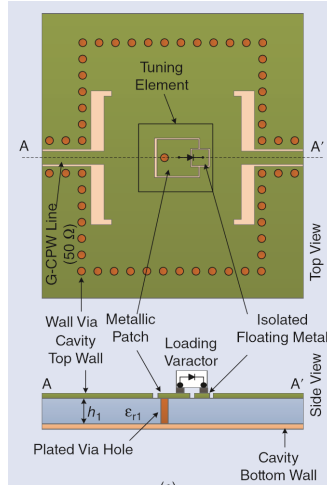


Figure 2.12: SIW tunable resonant cavity showing the centre conducting post and the floating metal patches. Taken from [4], © 2015 IEEE.

maximum along the sidewalls of the cavity and the E-field is maximum at the centre of the cavity, ferrite slabs can be placed along the side walls. Magnetic tuning of the cavity is therefore achieved by varying the magnetic fields. This method has been shown to provide a wider tuning range than a reactively loaded SIW tunable resonator. However, the implementation of this on SIW structure is quite challenging due to the inclusion of the ferrite slabs, as compared to loading the resonant cavity with a centre conductor [77], [4].

Another method presented in literature is the introduction of mechanically controlled via post connected to a screw at the center of the cavity [78]. The screw is isolated from the top of the SIW plate by using multiple annular ring cutouts. Tuning the screw alters the E-field distribution in the cavity thereby changing the resonant frequency of the cavity. This method provides moderate tuning range, and it is complicated by inserting the tuning screw within the SIW structure [4].

Table 2.1 shows a qualitative comparison of the different tuning methods applied to SIW resonant cavities. In all of these methods that include active devices, different ways have been employed to ensure the biasing of the active component.

GW offers DC isolated conducting planes. This is beneficial to the biasing of an active device as bridging wires or multiple cuts can be avoided. There has

Table 2.1: A qualitative comparison of the different tuning methods applied to SIW resonant cavities. Adapted from [4], © 2015 IEEE.

Tuning Basis	Tuned Mode	Tuning Range	Quality Factor	Fabrication Complexity
Side-coupled with varactor diode [8]	Electrical (varactor diode)	Low	Highest	Simple
Switchable perturbing via post [15]	Electrical (PIN diodes/RF MEMS switches)	High	High	Moderate
Tuning perturbing via post [31]	Electrical (varactor diodes)	Moderate	Moderate	Simple
Ferrite-based tuning with tunable perturbing via post [77]	Electrical (varactor diodes) with magnetic (ferrite slabs)	High	High	Complex
Mechanically tuned/perturbing via post [78]	Mechanical	Low	Moderate	Complex
Surface ring gap loaded with varactor diodes [79]	Electrical	Highest	High	Simple

been no published literature demonstrating frequency agility on a planar gap waveguide form exploiting the DC isolation of the structure.

2.9 Conclusion

A review of the basic theory of GW was presented with the different variants of the waveguide. GW as an alternative to the rectangular waveguide, provides DC isolated conducting planes. GW is realized within parallel plate waveguide with the top and bottom conducting plates isolated.

Recently developed planar variants of GW and MRG as presented in Section 1.1, show the implementation of GW on PCB, and are used to launch quasi-TEM lines within the medium. No paper was found in literature that implements the GGWG entirely on PCB or explores the DC isolation for frequency agile applications.

A review of the different tuning methods employed in the tuning of SIW resonant cavities was also presented. SIW has been extensively discussed in literature for frequency agile demonstrations but mostly with multiple etched rings and bridging wires needed for DC biasing.

Chapter 3

Propagation Characterisation of a Planar Groove Gap Waveguide

3.1 Introduction

This chapter presents comprehensive simulation characterisation of planar groove gap waveguide (PGGWG) [80]. The structural layout of the proposed PGGWG is presented with design guidelines of each dimension. The characterisation of the embedded EBG within the parallel plate waveguide, as employed in PGGWG, is also presented here with a numerical analysis of how each geometric parameter of a unit cell, as well as the relative permittivity of the dielectric substrate material, influences the achieved stopband. This is followed by the dispersion diagram of the PGGWG structure, modal properties, and S-parameter simulation of the proposed planar waveguide.

3.2 Basic Geometry

The transverse view of the proposed PGGWG implemented on multilayer dielectric substrate is shown in Figure 3.1.

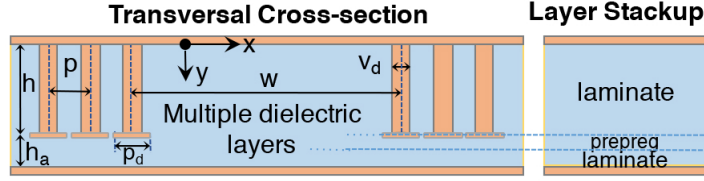


Figure 3.1: Cross-section of the PGGWG with layer stackup. All layers have the same relative permittivity.

The structure is formed by placing rows of blind vias with diameter v_d , each capped by a round catch pad of diameter p_d , at either side of a groove gap of width w . The embedded blind vias and catch pads constitute an EBG structure within the parallel plate waveguide. In this way, no wave can propagate in the region over a certain frequency range defined by the geometry of the EBG structure.

In the bandgap defined by the geometry of the EBG unit cell, the EBGs are used as AMCs to form the sidewalls of the waveguide. This is done to replace the electrical conductive sidewalls of the conventional rectangular waveguide and also the through-hole vias used in the case of SIW, thereby enabling the realisation of a rectangular waveguide structure within parallel plate waveguide with no DC connection between the top and bottom plates.

This embedded EBG structure can be of a mushroom-type [58], either having a round catch pad or square catch pad [56] as discussed in Section 2.3. The EBG with round catch pad has been adopted here in the analysis of the unit cell.

The arrangement of the PGGWG in Figure 3.2(b) is similar to the 3D micro-machined GGWG structure in Figure 3.2(a) which makes use of square pin EBG cells to form the AMC sidewalls of the waveguide [59]. A frequency bandgap is created within parallel plate propagating modes by placing a metal plate above the pins at a distance less than a quarter of the guided wavelength of the medium [56].

In the PGGWG arrangement, a substrate material is used in place of the air medium above the EBG surface and the top PEC plane, unlike in the conven-

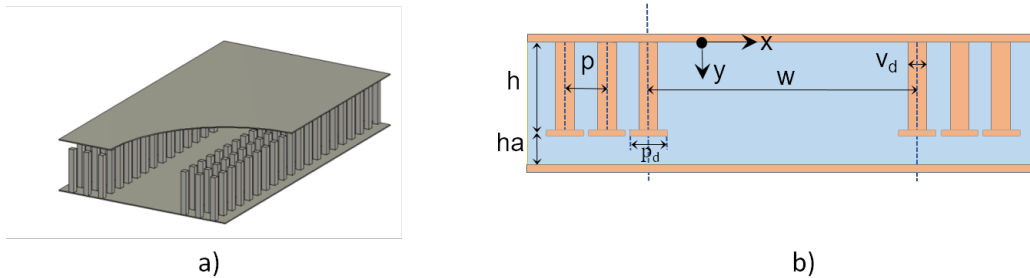


Figure 3.2: Physical GGWG layouts (a) 3D view of a micro-machined GGWG [59] (b) PGGWG derivative.

tional GGWG. This could either be of a different dielectric material or of same as the bottom substrate. The arrangement here allows for the implementation of the PGGWG entirely on a multilayer PCB stack without needing to create an air gap above the EBG surface.

The dielectric substrate height h is chosen to be less than $\lambda_g/4$ of the guided wavelength at the band centre. This is to suppress parallel plate modes propagating over the AMC surface. The height h of the dielectric substrate is the same as the height of the EBG as seen in Figure 3.1.

The dielectric substrate thickness, h_a , between the AMC surface and the bottom conducting plate, is also kept at a thickness less than $\lambda_g/4$ of the guided wavelength. For ease of manufacturability, this height can be chosen to match readily available dielectric laminate thickness. The thickness of the prepreg is accounted for within the substrate thickness h_a . Prepregs of same dielectric properties as the substrate material could be used to fill up the gap height h_a .

The stopband that the EBG unit cell creates can be controlled by varying the geometric parameters of the unit cell. By changing the size of the catch pad and both the height and the width of the via, the capacitance and inductance of the cell changes and therefore, the bandgap that the EBG creates is altered. It is, therefore, possible to control the bandgap accurately with v_d and p_d while keeping h and h_a to be equal to readily available laminate thickness.

The groove created within the rows of the EBG vias creates a propagation chan-

nel similar to that in a rectangular waveguide. It will be shown that within this groove, a transverse electric (TE) propagation mode can propagate in the medium. The groove width w can be selected to ensure that the fundamental TE_{10} mode, similar to that obtained in SIW, propagates within the stopband of the parallel plate mode; the frequency range where the EBG cells form AMC sidewalls.

3.3 Simulation Analysis of the Embedded EBG Structure

The achieved frequency bandgap of an EBG unit cell is directly related to the geometrical parameters of the unit cell arrangement and the substrate material of the host medium [81]. The EBG structure can be modelled as an electrically small resonator and within the bandgap where they provide wave suppression, their size is much smaller than the wavelength [58], [51].

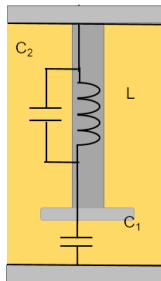


Figure 3.3: Embedded EBG structure unit cell as adopted in the PGGWG structure. This also shows the lumped element model of the structure.

The resonant frequency of the EBG unit cell used in the PGGWG as shown in Figure 3.3 can be represented by

$$f_c = \frac{1}{2\pi\sqrt{L(C_1 + C_2)}} \quad (3.1)$$

where C_1 represents the capacitance between the EBG catch pad and the bottom

conducting plate, C_2 represents the capacitance between the EBG catch pad and the top plane, and L represents the inductance of the metalized via.

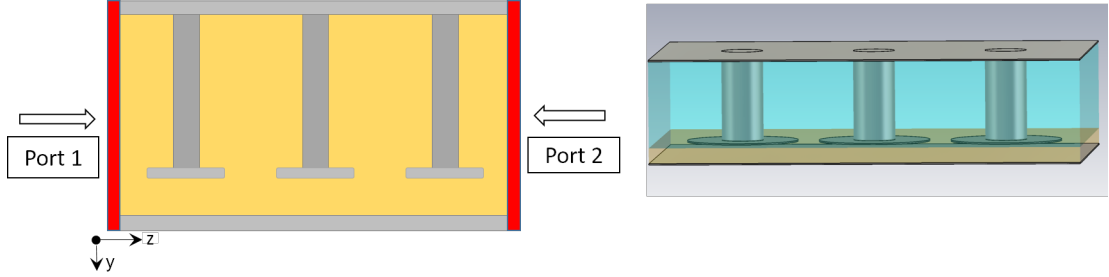


Figure 3.4: A side view showing the simulation setup used to extract the bandgap of an array of EBG cells within parallel plate structure using S-parameters.

The guided wavelength of the medium at different frequency points is given as

$$\lambda_g = \frac{c}{f\sqrt{\epsilon_r}}$$

where ϵ_r is the relative permittivity of the dielectric material used.

EM simulation study was performed using the time domain solver in CST Microwave Studio 2016 package. The bandgap can be extracted by simulating the S-parameters between two waveguide ports placed on either side of a row of embedded EBG unit cells.

The computational domain in Figure 3.4 is limited by PEC boundaries on the xz planes at $y = 0$ and $y = h + h_a$. PMC boundaries are applied on the yz plane at $x = 0$ and $x = p_d$. The transmission coefficient S_{21} (dB) is extracted for the EBG in the K_a frequency band. Figure 3.5 shows the S_{21} (dB) of the EBG unit cell arrangement of Figure 3.4. The bandgap can be observed between 23 GHz and 45 GHz.

The bandgap definition used throughout this study is the frequency range where S_{21} is below 20 dB. The two frequency points defining the edges of the bandgap will be referred to as the lower and the upper-frequency points respectively. To analyse the effect of a change in geometrical parameters of the EBG structure

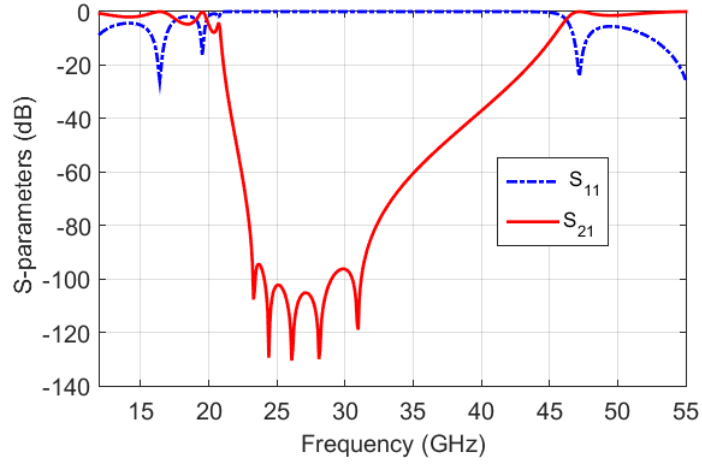


Figure 3.5: S-parameters; S_{11} (dB) and S_{21} (dB) for the setup in Figure 3.4. The embedded EBG mushroom type structure has the following dimensions: $h = 0.508$ mm, $h_a = 0.106$ mm, $v_d = 0.3$ mm, $p_d = 0.8$ mm, $p = 0.95$ mm, $\epsilon_r = 3.5$, $\tan\delta = 0.004$

on the bandgap, the different geometric parameters of the unit cell are varied, and their effects studied.

3.3.1 Effect of the number of EBG rows on attenuation

The suppression of parallel plate modes depends on the number of embedded EBG unit cells placed in a row within the parallel plate waveguide. A unit cell creates a frequency band gap; however, to increase the suppression bandwidth, the number of unit cells in a row should be increased.

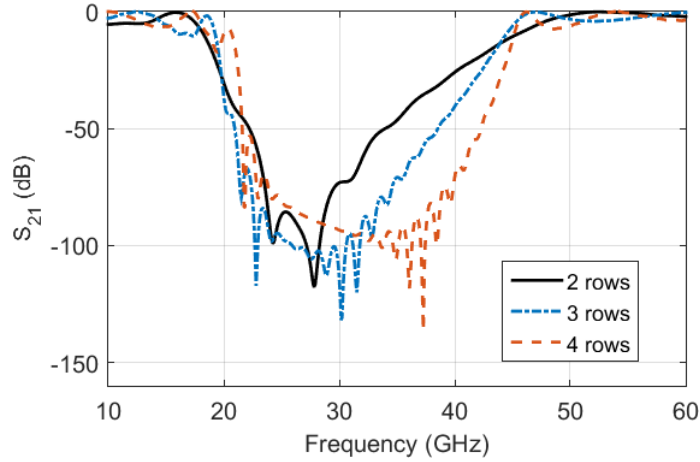


Figure 3.6: Magnitude of S_{21} (dB) for different number of unit cells with the following dimensions: $h = 0.508$ mm, $h_a = 0.106$ mm, $v_d = 0.3$ mm, $p_d = 0.9$ mm, $p = 0.95$ mm, $\epsilon_r = 3.5$, $\tan\delta = 0.004$.

Here, the geometry of the unit cells is kept constant while only varying the number of EBG unit cells along the z-axis as depicted in Figure 3.4. The substrate height, $h = 0.508$ mm while $h_a = 0.106$ mm.

As observed in Figure 3.6, a wider stopband is achieved with more than one row of embedded EBG vias. We observed that the bandwidth increases from 21 GHz using two rows to 25 GHz with four rows. With this in mind, three cells of embedded EBG structures are considered in the design of the PGGWG and also for further analysis in this work.

3.3.2 Effect of varying the height h on the stopband

The height h of the embedded EBG refers to the height of the via between the catch pad and the bottom conducting plane as seen in Figure 3.1. The relationship between the suppression band and the height h , with the other parameters keep constant, is shown in Figure 3.7.

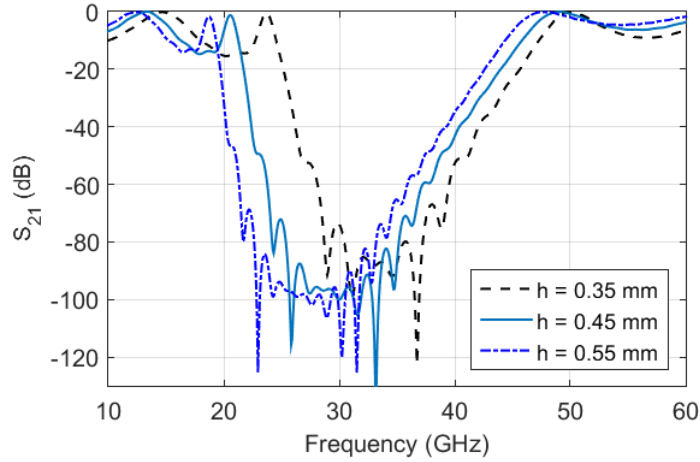


Figure 3.7: Magnitude of S_{21} (dB) for different via height h of the EBG unit cells with the following dimensions: $h_a = 0.106$ mm, $v_d = 0.3$ mm, $p_d = 0.8$ mm, $p = 0.95$ mm, $\epsilon_r = 3.5$, $\tan\delta = 0.004$.

As observed, increasing the height h increases the gap between the bottom conducting plane and the round catch pad, thereby reducing the effective capacitance between the two surfaces. As a result, the resonant frequency of the unit cell shifts to a lower frequency. The bandwidth varies from 20 GHz to 23 GHz with h varying from 0.35 mm to 0.55 mm.

The substrate height, h is a key geometric parameter as it determines the lower and upper-frequency limit of the bandgap. h can be set to a desired and readily available substrate thickness for ease of manufacturing while ensuring that its kept at less than $\lambda_g/4$ of the guided wavelength.

3.3.3 Effect of varying the gap height h_a on the stopband

The gap height h_a between the top of the round catch pad and the bottom conducting plane of the PGGWG in Figure 3.1 must be kept at a distance less than the $\lambda_g/4$ at the centre frequency of the band. This is done to ensure the suppression of surface waves that may exist in the gap between the two parallel plates while allowing waves to propagate in the desired direction along the groove

of the PGGWG.

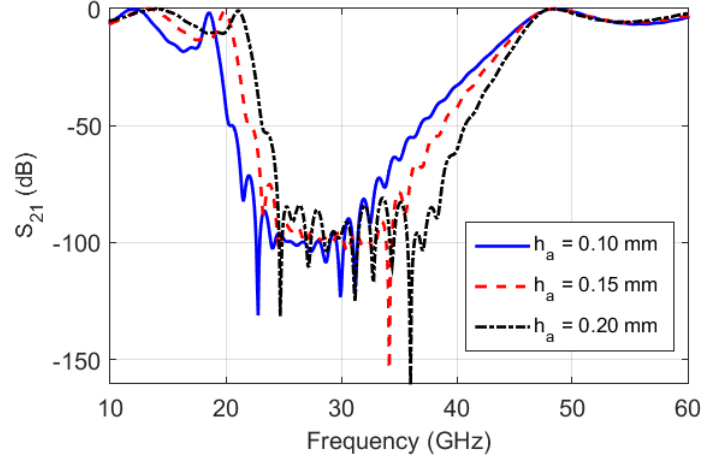


Figure 3.8: Magnitude of S_{21} (dB) for different the gap height h_a of embedded EBG unit cells with the following dimensions: $h = 0.508$ mm, $v_d = 0.3$ mm, $p_d = 0.8$ mm, $p = 0.95$ mm, $\epsilon_r = 3.5$, $\tan\delta = 0.004$.

It can be seen in Figure 3.8 that the suppression band is reduced by increasing h_a . This is because h_a changes the capacitance between the round catch pad and the top conducting plane resulting in a shift in the resonant frequency.

A decrease in the bandwidth is also observed from 24 GHz for $h_a = 0.10$ mm to 22 GHz with $h_a = 0.20$ mm. As the gap height increases, the bandgap created by the suppression of parallel plate mode reduces.

3.3.4 Effect of pitch p variation on the stopband

The pitch p determines the spacing between consecutive EBG unit cell rows within an array of unit cells. The dimension, $g = p - p_d$ (where p is the pitch and p_d is catch pad diameter) defines the gap between adjacent round catch pad.

Increasing the pitch increases the separation gap, g between consecutive EBG cells. Figure 3.9 shows the variation of the pitch p from 0.9 mm to 1.9 mm. This corresponds to a separation gap, g varying from 0.1 mm to 1.1 mm. We

observe that increasing the pitch reduces the effective stopband bandwidth. The bandwidth is reduced from 24 GHz with a gap $g = 0.1$ mm to 18 GHz for $g = 1.1$ mm.

For wider separation gaps, a second bandgap is created at 50 GHz with a pitch p of 1.9 mm. It is, therefore, important to keep the gap close enough to avoid leakage in order to maintain a single distinct bandgap from the EBG structure.

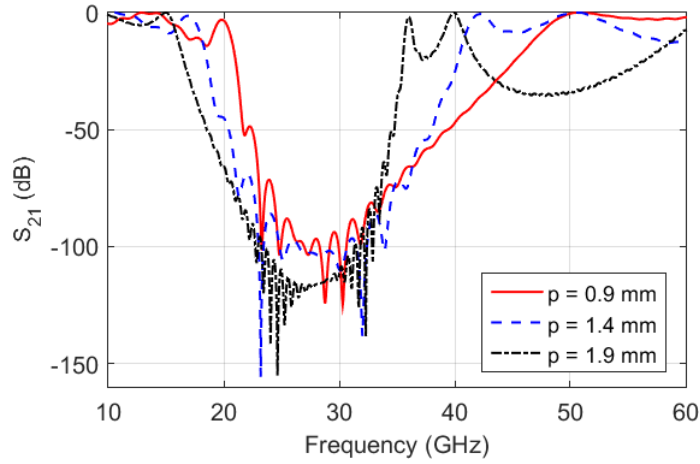


Figure 3.9: Magnitude of S_{21} (dB) for different values of pitch p of the EBG unit cells with the following dimensions: $h_a = 0.106$ mm $h = 0.508$ mm, $v_d = 0.3$ mm, $p_d = 0.8$ mm, $\epsilon_r = 3.5$, $\tan\delta = 0.004$.

3.3.5 Effect of varying the via diameter v_d on the stopband

As observed in Figure 3.10, by altering the inductance L of the resonator, the resonant frequency of the unit cell is altered. By reducing the via diameter, we observe a shift of the bandgap to lower frequencies. This is as a result of the increased EBG cell inductance. The bandwidth decreased from 31 GHz to 23 GHz by varying the via diameter, v_d from 0.35 mm to 0.15 mm, indicating that stronger loading increases the Q-factor of the resonator.

The design of the PGGWG for manufacturability will require the selection of

an appropriate via diameter based on the manufacturer's fabrication capabilities, with the other parameters of the unit cell adjusted to achieve the desired suppression of the parallel plate modes.

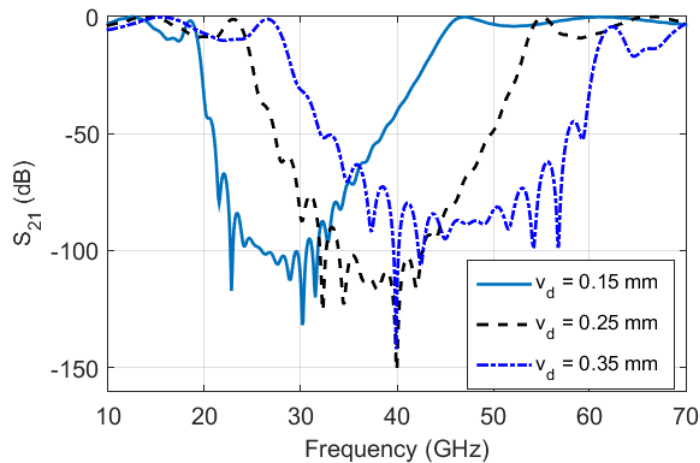


Figure 3.10: Magnitude of S_{21} (dB) for different via diameter, v_d of the EBG unit cells with the following dimensions: $h_a = 0.106$ mm, $h = 0.508$ mm, $p_d = 0.8$ mm, $p = 0.95$ mm, $\epsilon_r = 3.5$, $\tan\delta = 0.004$.

3.3.6 Effect of varying the catch pad p_d surface area

The EBG unit cell can either be implemented with a square or a round catch pad, as shown in the inset of Figure 3.11.

In this parametric experiment, the unit cell geometry is kept constant at $h_a = 0.106$ mm, $v_d = 0.3$ mm, $h = 0.508$ mm, $p = 0.95$ mm with the diameter of the round catch pad, p_d as well as the size of the square patch varied. We can observe from Figure 3.11 that, as the surface area of the catch pad increases, the effective capacitive load between EBG surface and the top conducting plate changes, thereby creating a shift in the resonant frequency of the unit cell. An increase in the size of the pad lowers the suppression band as expected from Equation 3.1 when the capacitance C_1 and C_2 are increased.

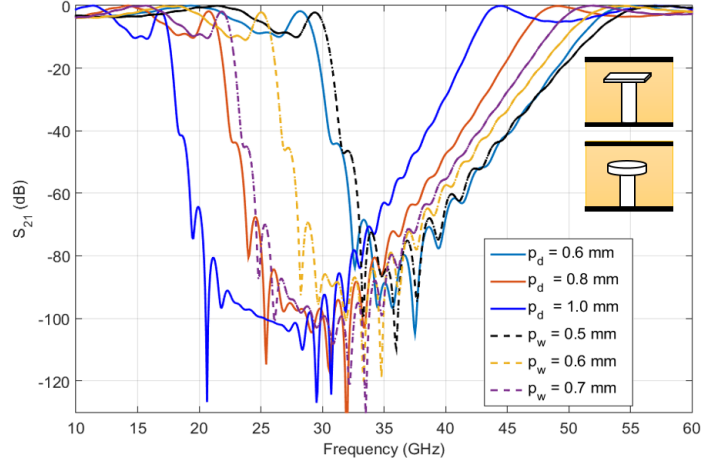


Figure 3.11: Magnitude of S_{21} (dB) for the different embedded EBG structures in parallel planes showing the effect of different pad diameter and patch sizes [82].

The insert in Figure 3.11 shows the EBG unit cell for round and square mushroom-type cells where p_d is the diameter of the round pad and p_w the width of the square patch. The dimensions of unit cell are: $h_a = 0.106$ mm, $v_d = 0.3$ mm, $h = 0.508$ mm, $p = 0.95$ mm. By increasing the capacitive load (C_1 and C_2) or the inductive load L in the case of varying the via diameter, the bandgap can be controlled effectively irrespective of h and h_a .

3.3.7 Effect of the dielectric constant ϵ_r on the bandgap

Substrate materials of different relative permittivity ϵ_r , and loss tangent $\tan\delta$ can be used in the design of PGGWG.

As observed in Figure 3.12, an increase in the relative permittivity, ϵ_r , of the substrate, moves the stopband to lower frequencies. A 60% reduction in the bandwidth is observed by increasing ϵ_r from 3.5 to 31.5. This result is obtained while keeping the dimensions of the unit cell arrangement constant at $h = 0.508$ mm, $h_a = 0.106$ mm, $v_d = 0.3$ mm, $p = 0.95$ mm, $p_d = 0.8$ mm and $\tan \delta = 0.004$.

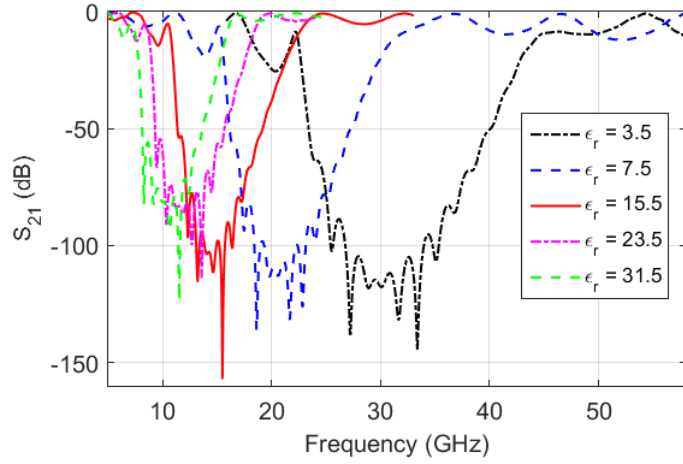


Figure 3.12: Magnitude of S_{21} (dB) for different substrate material of ϵ_r . The dimensions of the EBG unit cell are: $h_a = 0.106$ mm $h = 0.508$ mm, $p_d = 0.8$ mm, $p = 0.95$ mm.

This is a particularly important observation in the development of the PGGWG taking into consideration the miniaturisation of the physical structure. Depending on the frequency of operation, the bandgap can be achieved either by choosing a suitable dielectric substrate material as observed in Figure 3.13 or increasing the substrate thickness h .

Table 3.1 summarizes the achievable suppression bands obtained by changing the substrate thickness, h or increasing the relative permittivity of the substrate material. A bandwidth of 28 GHz (12 GHz to 40 GHz) is obtained using a thicker substrate as opposed to a thinner substrate. There is, therefore, a trade-off between the substrate thickness and the relative permittivity of the substrate material which will influence the design choice.

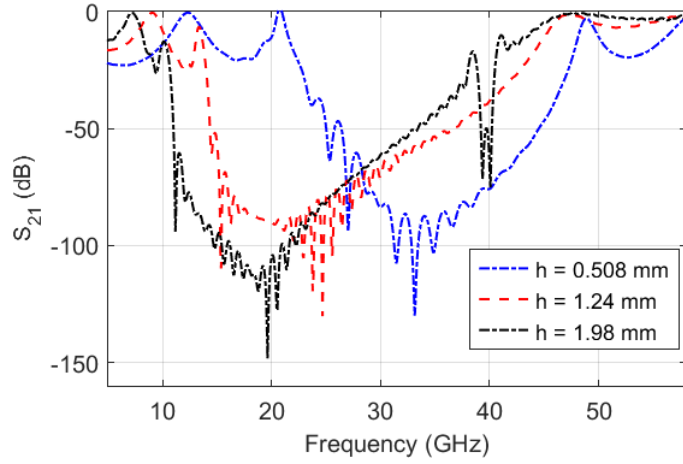


Figure 3.13: Magnitude of S_{21} (dB) for different substrate heights h . The dimensions of the EBG unit cell are: $h_a = 0.106$ mm $h = 0.508$ mm, $p_d = 0.8$ mm, $p = 0.95$ mm, $\epsilon_r = 3.5$

Table 3.1: Suppression bandwidth of the EBG unit cell arrangement for varying relative permittivity ϵ_r , substrate thickness h and catch pad diameter p_d .

h (mm)	ϵ_r	h_a (mm)	p_d (mm)	v_d (mm)	p (mm)	Suppression Band (GHz)
0.508	31.5	0.106	0.8	0.35	0.95	8 - 16
0.508	23.5	0.106	0.8	0.35	0.95	9 - 18
0.508	15.5	0.106	0.8	0.35	0.95	11 - 22
0.508	7.5	0.106	0.8	0.35	0.95	15 - 30
0.508	3.5	0.106	0.8	0.35	0.95	22 - 43
1.24	3.5	0.106	0.8	0.35	0.95	14 - 43
1.980	3.5	0.106	0.8	0.35	0.95	10 - 40

3.4 Dispersion Diagram

The dispersion diagram is computed for the PGGWG arrangement as shown in Figure 3.14. This was done using full-wave Eigenmode simulations carried out in CST Microwave Studio 2016. The simulated model includes three rows of embedded EBG unit cells on either side of the groove. The PGGWG structure is periodic in the z -direction with the propagation channels of the groove also along the z -axis. Thus the phase shift in the z -direction is considered.

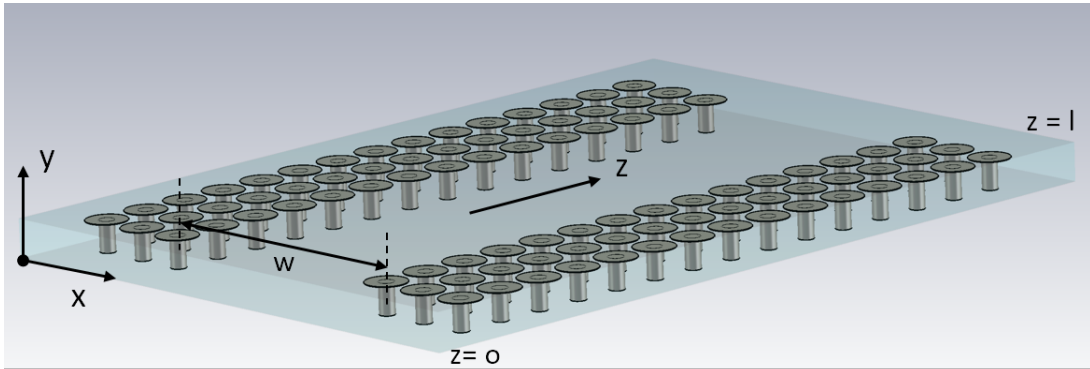


Figure 3.14: The 3D model setup used in extracting the propagating modes within the PGGWG for plotting the dispersion diagram. The waveguide dimensions are: $h = 0.508$, $w = 4.5$ mm, $h_a = 0.106$ mm, $v_d = 0.3$ mm, $p_d = 0.8$ mm, $p = 0.95$ mm, $\epsilon_r = 3.5$, $\tan\delta = 0.004$, $l = 10$ mm.

Boundary conditions at $z = 0$ and $z = l$ in the model are set to periodic in CST Eigenmode solver, in order to model an infinite extent of the PGGWG in the z -direction.

The open boundary condition is chosen at x_{min} and x_{max} of the model. This is in accordance with the PGGWG physical geometry to ensure that there is no electric contact between the top and bottom plate. The PEC boundary condition is chosen at y_{min} and y_{max} .

The phase shift ϕ of the propagating wave in the z -direction is related to the

phase constant β by:

$$\beta = \frac{\phi(rad)}{l}$$

where l is the distance between the planes that define the phase shift. That is p , the pitch, in the z -direction. For certain values of the phase shift, CST Eigenmode solver determines the frequency at which a mode is propagating with a phase constant that produces the specified value of phase shift.

The groove width, w , of the PGGWG can be varied. This is similar to the case of the GGWG [48] and rectangular waveguide [38]. In GGWG, the width of the groove is used to determine the cutoff frequency of the fundamental TE_{10} propagating mode while the dimensions of the EBG unit cells controls the lower and upper operating frequency of the GGWG.

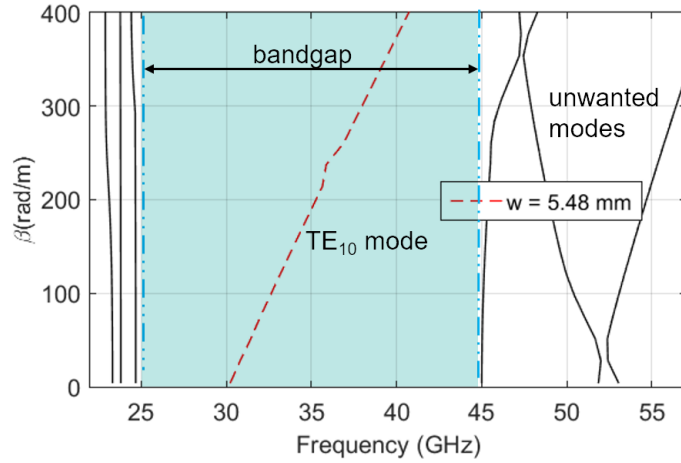


Figure 3.15: Dispersion diagram showing the propagation of the fundamental mode and parallel plate modes within the PGGWG structure. The groove width $w = 5.48 \text{ mm}$.

With the dimensions of the PGGWG set at: $h = 0.508 \text{ mm}$, $h_a = 0.106 \text{ mm}$, $v_d = 0.3 \text{ mm}$, $p_d = 0.8 \text{ mm}$, $p = 0.95 \text{ mm}$, $\epsilon_r = 3.5$, $\tan\delta = 0.004$, $l = 10 \text{ mm}$ and the width $w = 5.48 \text{ mm}$, we observe the parallel plate mode below 25 GHz with the bandgap between 25 to 45 GHz from the dispersion diagram plot in Figure 3.15. Below 25 GHz, the PGGWG is not usable as the parallel plate modes are

no longer suppressed. This is due to the design of the EBG unit cell, which no longer acts as AMC sidewall. Also, above the upper limit of the stopband of the EBG, the PGGWG waveguide is similarly unusable for the same reason. Within the stopband, however, the fundamental propagating mode (TE_{10}) is clearly visible with a cutoff frequency at 30 GHz.

Figure 3.16(a) shows a cross-section of the PGGWG with the electric field distribution of the fundamental propagating mode shown. It can be observed that the field distribution of this fundamental mode has similar characteristics to that of the TE_{10} propagating mode of the rectangular waveguide. The electric field components (Figure 3.16(c)) are perpendicular to the z -axis, which is, the direction of propagation. The attenuation of the electric fields at the AMC sidewalls is also visible from Figure 3.16(b).

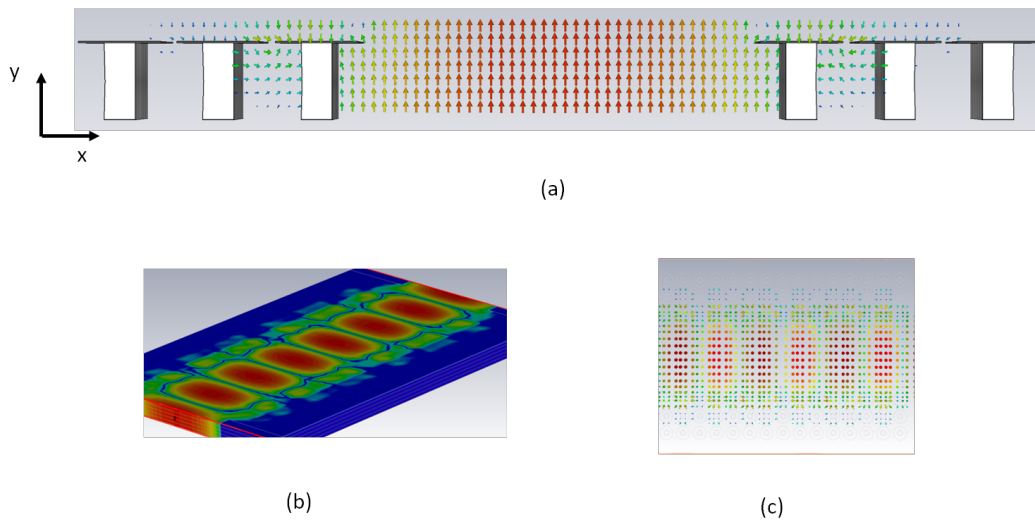


Figure 3.16: A cross section view of the PGGWG showing the E-field distribution of its fundamental propagating mode (TE_{10}). (a) E-fields lines. (b) Magnitude of the E-field from a sectional view along the y -axis. (c) E-fields lines from the top view of the structure.

By varying the width w of the groove, the fundamental propagating mode can be designed to fall within the EBG stopband. As shown in Figure 3.17, by reducing the width w , the cut-off frequency of the fundamental mode increases.

This variation is only effective within the confines of the parallel plate suppression bandgap.

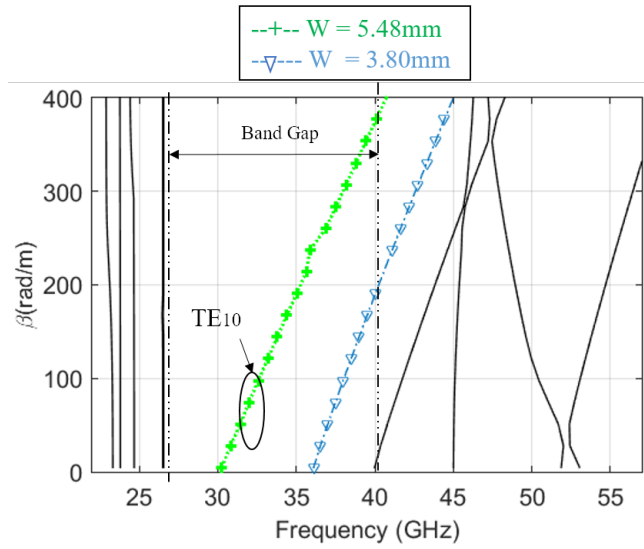


Figure 3.17: Dispersion diagram showing the propagation of the fundamental mode and with varying groove width w . Other dimensions kept constant are: $h = 0.508$ mm, $h_a = 0.106$ mm, $v_d = 0.3$ mm, $p_d = 0.9$ mm, $\epsilon_r = 3.5$, $\tan\delta = 0.004$, $l = 10$ mm.

3.5 Modal Analysis

The electric field distribution within the PGGWG structure is observed at different frequencies for the waveguide dimensions as presented in Section 3.4.

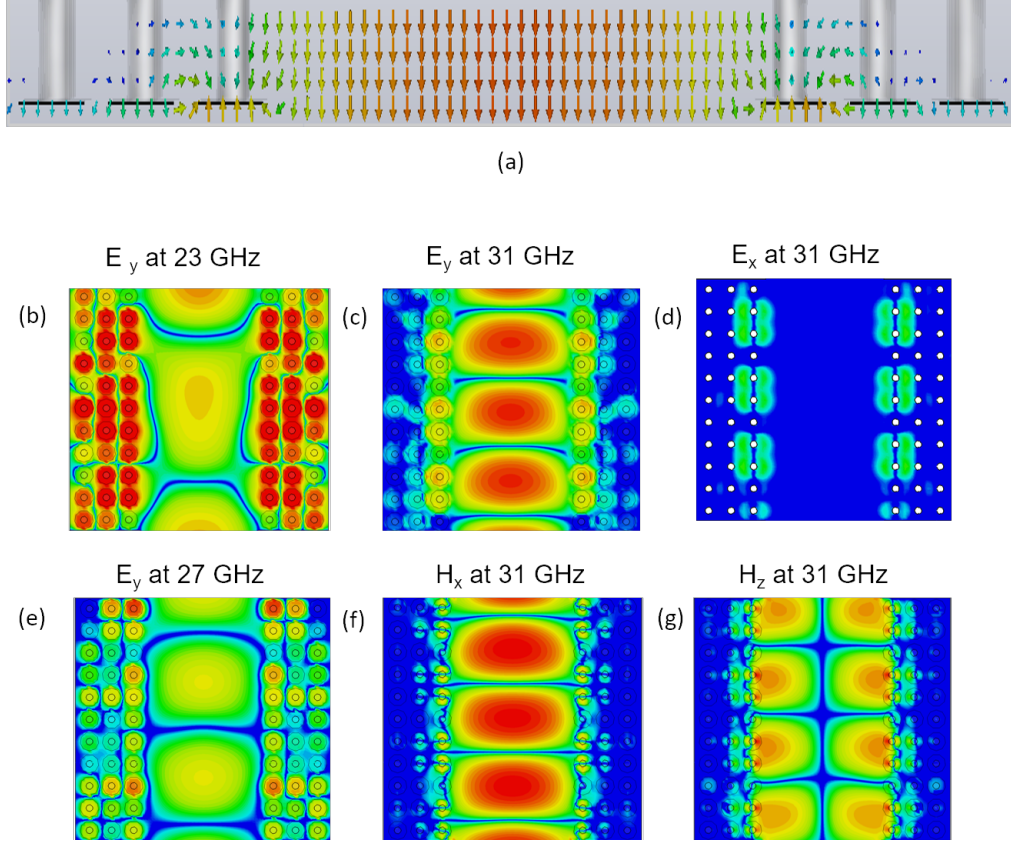


Figure 3.18: E-field distributions within the PGGWG at different frequency points of observation. (a) A cross-section of the E-field at 31 GHz. (b) The magnitude of the E-fields, E_y below the parallel plate suppression band (23 GHz). (c) The magnitude of the E-field, E_y of the TE_{10} mode. (d) The magnitude of the E-field, E_x of the TE_{10} mode. (e) The magnitude of the E-field, E_y above the lower limit of the bandgap but below the fundamental mode (27 GHz). (f) The magnitude of the magnetic field H_x of the TE_{10} mode. (g) The magnitude of the magnetic field H_z of the TE_{10} mode.

Figure 3.18(a) shows the vector electric field distribution of the desired dominant

TE₁₀ mode in a cross-section of the waveguide. Figure 3.18(b) shows the E-field of a propagating parallel-plate mode below the parallel plate bandgap ($f = 23$ GHz) and a suppressed parallel plate mode inside the bandgap but below f_c of the TE₁₀ mode $f = 27$ GHz in Figure 3.18(e). The non-zero field components of the fundamental mode inside the bandgap (31 GHz) is shown in Figure 3.18(c) with the electric field distribution, E_x in Figure 3.18(d) zero.

Figure 3.18(f) shows the magnetic field H_x at 31 GHz of the fundamental propagating mode with the H_z component shown in Figure 3.18(g)

These plots of the electric and magnetic field distributions indicate a propagating TE₁₀ mode in the groove of the waveguide.

3.6 S-Parameter Analysis

The PGGWG structure is excited with waveguide ports in CST Microwave Studio as shown in Figure 3.19. The open boundary condition is set at x_{min} and x_{max} . PEC boundary conditions are set on the y-plane (y_{min} and y_{max}). The port planes, z_{min} and z_{max} are set to open boundaries.

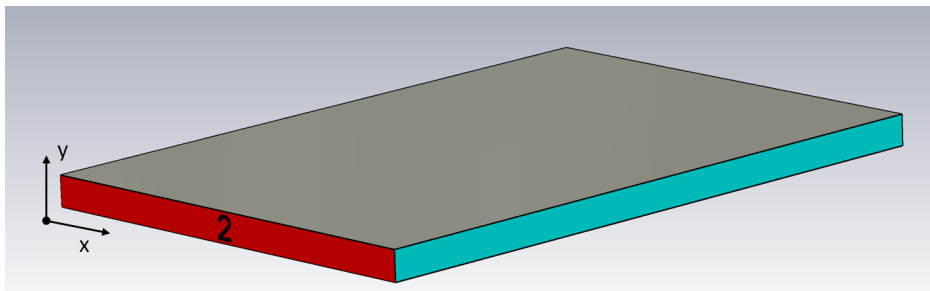


Figure 3.19: 3D view of the PGGWG structure excited with waveguide ports in CST with dimensions; $h = 0.508$ mm, $h_a = 0.106$ mm, $v_d = 0.3$ mm, $p_d = 0.7$ mm, $p = 0.95$ mm, $\epsilon_r = 3.5$ and $\tan\delta = 0.004$.

The TE₁₀ mode excitation can be observed at the port plane of the PGGWG as shown in Figure 3.20, with the S-parameter result of the PGGWG simulation in Figure 3.21. We observe from this result that the lower frequency limit of the

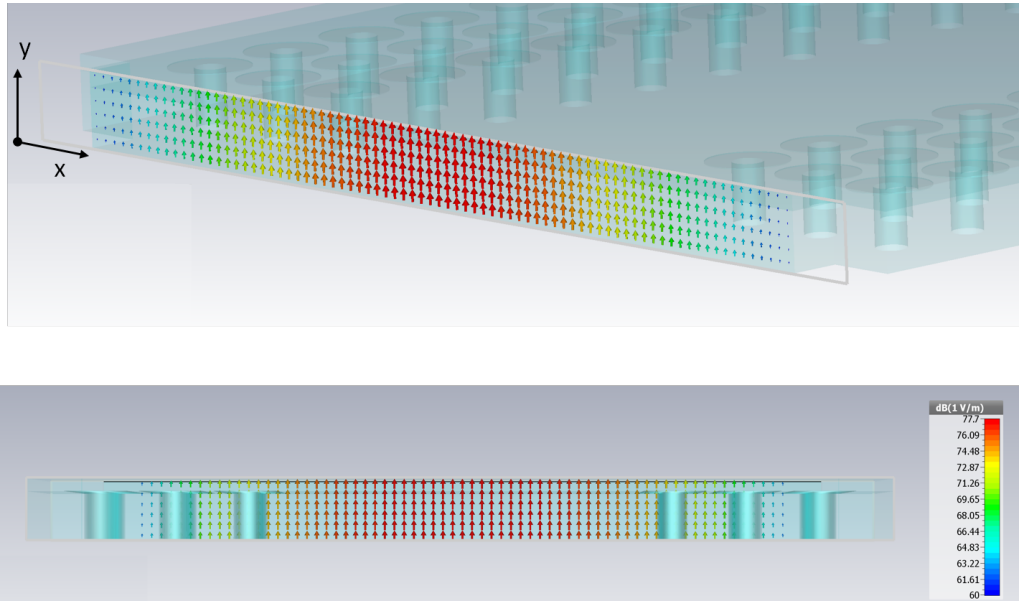


Figure 3.20: 3D view of the PGGWG showing the E-field distribution of the TE₁₀ mode excitation at the port plane.

waveguide is at 25 GHz and the upper limit at 43 GHz. The S_{11} (dB) is below 40 dB over the band of interest.

We also note that the usable passband of the PGGWG corresponds to the suppression band of the EBG unit cell as shown in Figure 3.22, with the lower and upper-frequency limits of the waveguide determined by the geometry of the embedded EBG unit cell.

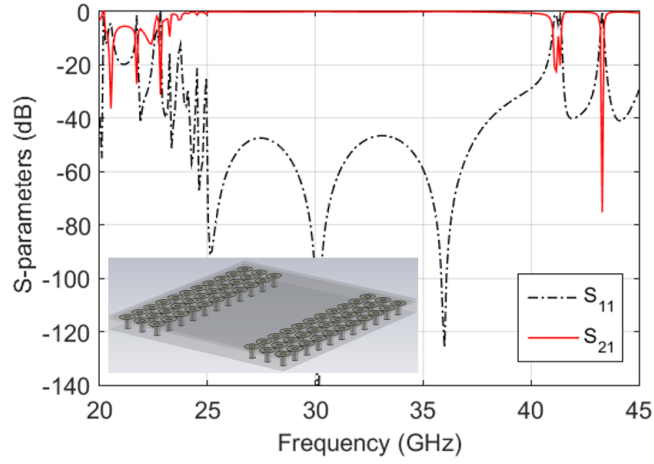


Figure 3.21: S-parameter (dB) results of the PGGWG simulation with waveguide port excitation. The dimensions of the PGGWG are: $h = 0.508$ mm, $h_a = 0.106$ mm, $v_d = 0.3$ mm, $p_d = 0.7$ mm, $p = 0.95$, $w = 5.48$ mm, $\epsilon_r = 3.5$ and $\tan\delta = 0.004$.

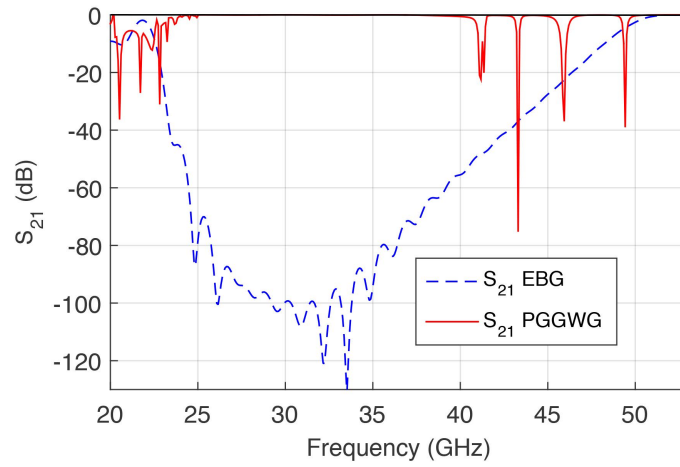


Figure 3.22: S_{21} (dB) of simulated PGGWG using waveguide ports and that of the stopband of an array of EBG unit cell embedded within parallel plates.

3.7 Conclusion

It has been shown that the proposed PGGWG exhibits similar propagation characteristics to that of a rectangular waveguide. Unlike SIW, the planar equivalent of the rectangular waveguide, PGGWG provides DC isolated planes, making use of an EBG structure to provide AMC side walls replacing the through hole vias of SIW.

The fundamental propagating mode within the groove of the PGGWG exhibits similar propagating characteristics as that of a rectangular waveguide with the TE_{10} frequency cutoff of the mode related to the width of the groove. As seen in Section 3.3, the design of the embedded EBG unit cell plays a vital role in determining the suppression of parallel plate mode within the parallel plate waveguide. This, in turn, determines the lower and upper frequency limits of the PGGWG and can be designed for any reasonable desired frequency band of interest.

An S-parameter simulation of the PGGWG with waveguide ports using full wave simulation shows a passband between the upper and lower frequency limit of the bandgap.

A summary of the design processes of the PGGWG is outlined as follows:

- Determine the required frequency of operation of the PGGWG.
- Determine the manufacturing limitations. This will help with the appropriate selection of the substrate height and via diameter.
- Analyze the unit cell arrangement to determine the suppression bandwidth taking into consideration the design guidelines of the EBG structure. The numerical study should be done by changing parameters such as the patch width, the via diameter and the substrate height h_a and h .
- The relative permittivity of the substrate material also influences the passband of the unit cell. Higher ϵ_r values of the dielectric substrate result in a lower placed stopband. This is of importance as a trade-off can be made

between either increasing the substrate thickness h or using a substrate material of higher ϵ_r to achieve miniaturisation.

- The effective width of the groove w can be determined numerically by observing the propagation of the fundamental mode within the parallel plate modes from the dispersion diagram of the structure using the previously determined EBG dimensions.

The appropriate design of the EBG unit cell can enable one to extend the suppression bandwidth. As discussed in Section 3.3, the via diameter v_d , the substrate thickness h , and diameter of the round catch pad p_d , as well as the relative permittivity ϵ_r , of the substrate material play a role in determining the EBG band.

Chapter 4

PGGWG Prototyping and Measurement

4.1 Introduction

A wideband transition from coplanar waveguide (CPW) to the PGGWG is presented in this chapter and the manufacturing process is discussed. The transition is designed to maintain the DC isolation between the top and bottom plane of the PGGWG while using a Southwest Microwave 1.85mm jack end-launch connector (datasheet of the connector is available in Appendix A) to enable coaxial measurement. The Thru-Reflect-Line (TRL) calibration method is used to extract the transmission characteristics of the PGGWG and the design and layout of the standards are presented. The de-embedded S-parameter measurements of the PGGWG are shown and compared to simulated results.

4.2 Wideband Coplanar Waveguide to PGGWG Transition

The geometry of the proposed wideband transition from CPW to PGGWG is shown in Figure 4.1. It is based on a similar transition proposed in [83] which integrates the coupling slot and impedance transformer into one tapered coupling slot to achieve a wide bandwidth. This enables the integration of the PGGWG with a 50Ω CPW feed allowing for the 1.85mm coaxial connector to be connected to the CPW end of the PGGWG circuit.

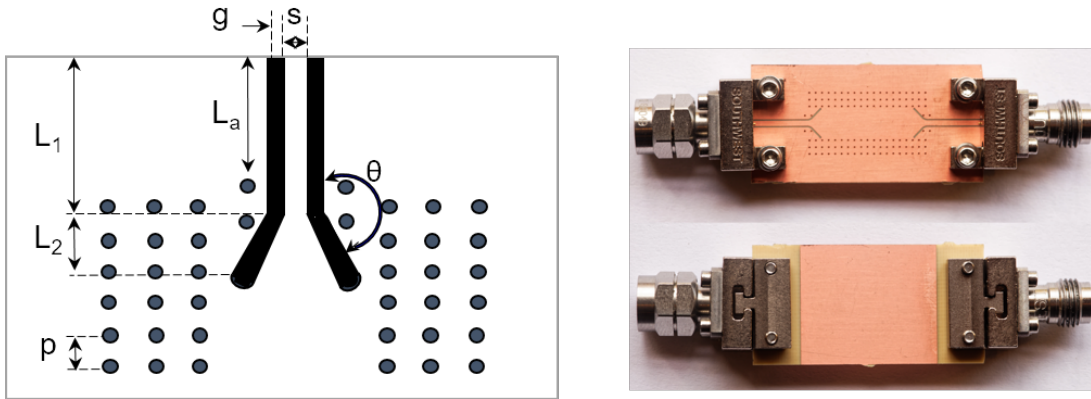


Figure 4.1: CPW to PGGWG transition with the prototype PGGWG circuit showing the top and bottom view attached to the end-launch connector.

The CPW transition is etched from the bottom conductor (at $y = 0$) of the PGGWG circuit as seen in Figure 4.1, the side to which the EBG vias are attached to the bottom plate. This is done to allow the flow of surface current from the port through the EBG cells and thus excite the modes within the groove of the PGGWG. The copper of the top plane ($y = h_a + h$) is etched away to allow the end-launch connector to be clamped on the PCB without creating a DC connection between the planes.

The dimensions of the optimized CPW to PGGWG transition are given in Table 4.1. Figures 4.2(a),(b) and (c) show the bottom, top and 3D view of the transi-

tion simulation model, respectively. EBGs, similar as that used for the sidewall of the PGGWG, are placed along the CPW length to provide better impedance matching and suppress possible resonance within the operating band of the transition. The tapered coupling slot of length $\lambda_g/4$ acts as an impedance transformer to convert the impedance of the PGGWG to the CPW port impedance.

Table 4.1: Optimized dimensions for the CPW to PGGWG transition

Dimension	mm
g	0.13
s	0.8
Θ	135°
L_1	4.5
L_2	1.6
p	0.95
L_a	3.5
v_d	0.3
p_d	0.7
h	0.508
h_a	0.168

In Figure 4.3(a), we observe the TEM mode electric field at the CPW port plane of the transition. This mode then transforms to a TE₁₀ propagating mode in the PGGWG medium (Figure 4.3(b)). Figure 4.3(c) and (d) shows the surface current along the top and bottom conducting plate of the transition.

The S-parameters of the transition from CPW to PGGWG is as shown in Figure 4.4. A wide passband from 25 GHz to 44 GHz is observed. The return loss of the transition is better than -10 dB over the passband of with the transmission response relatively flat at -2 dB over the range.

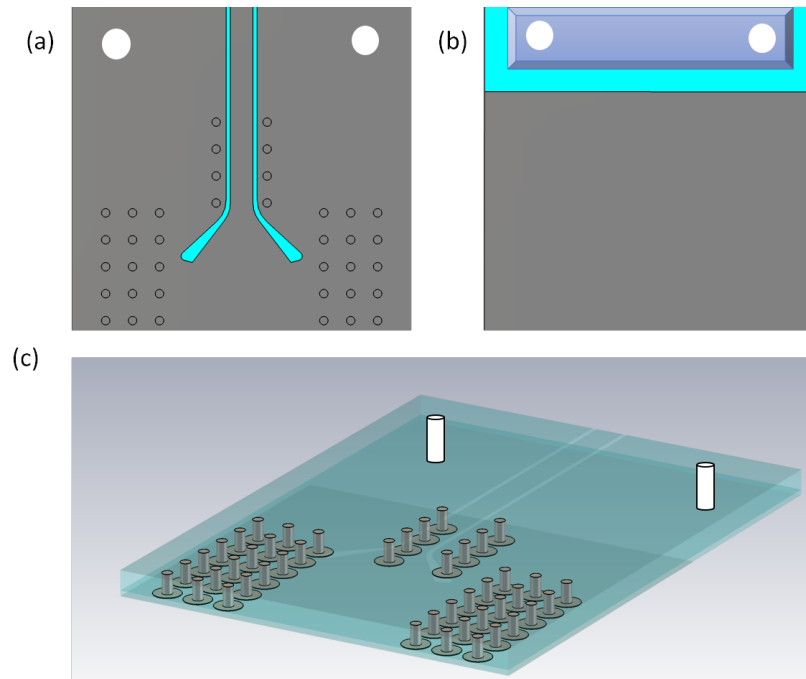


Figure 4.2: The CPW to PGGWG transition implementation in CST. (a) Bottom view with the CPW coupling slot. (b) Top view with the end-connector attached. (c) 3D view of the CPW to PGGWG transition.

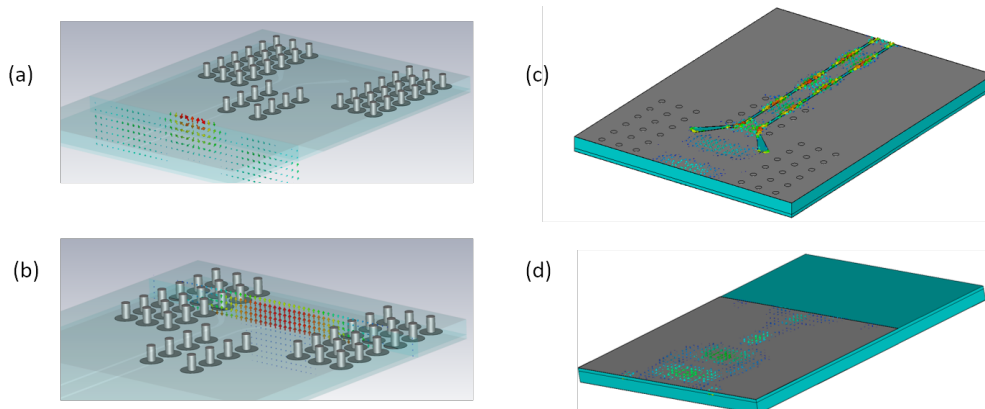


Figure 4.3: E-field and surface current plot of the CPW - PGGWG transition. (a) Quasi-TEM field in the CPW transition. (b) TE_{10} mode in the PGGWG. (c) Surface current along the bottom plane. (d) Surface current along the top plane.

Although the transition has relatively high insertion loss of approximately 2 dB, the combined effects of the connector and the CPW-PGGWG transition is calibrated out to extract transmission parameters of the PGGWG section alone. The de-embedding method employed for measurement of the PGGWG is discussed in the next section.

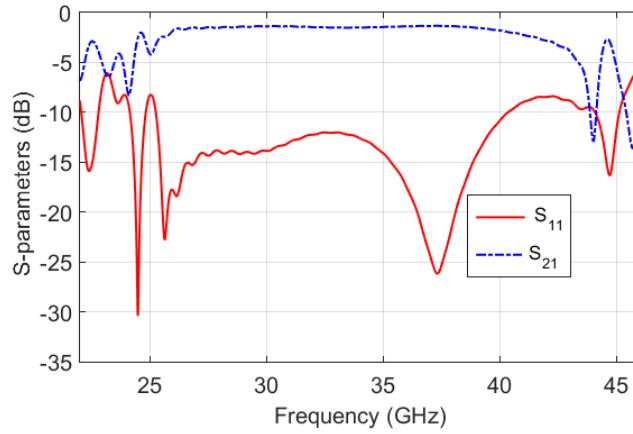


Figure 4.4: Simulated S-parameters of the CPW-PGGWG transition over the band of interest

4.3 PGGWG Calibration Standards

A Thru-Line-Reflect (TRL) calibration method, as described in [84], is employed to remove the combined effect of the coax connector and the CPW-PGGWG transition from measurement, allowing for the extraction of the transmission characteristics of the PGGWG alone.

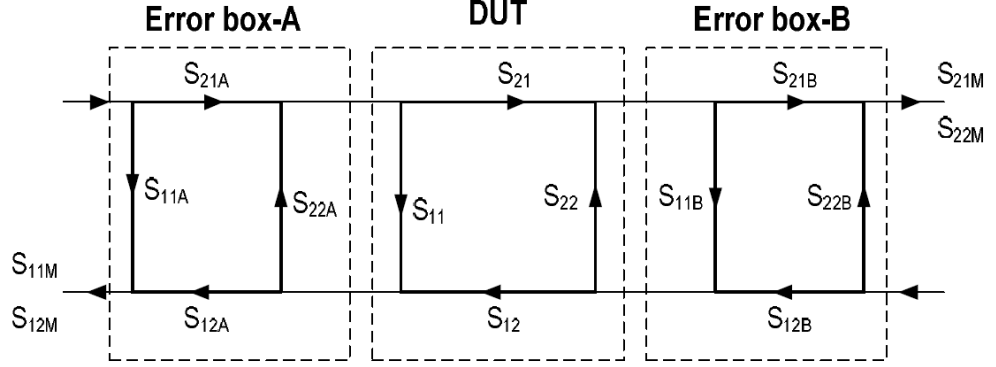


Figure 4.5: TRL error model. Taken from [85], © 2010 IEEE.

The PGGWG with the transition can be represented by the error model shown in Figure 4.5 [85]. The error model of box A and box B represents the transition from CPW to PGGWG which can be de-embedded to extract the desired characteristics of the PGGWG.

The cascaded ABCD-parameters of the measured response can be expressed in matrices as:

$$T_m = T_A T_{DUT} T_B$$

where T_A and T_B are virtual error transmission box related to the transition from CPW to the GGWG as discussed in Section 4.2. T_{DUT} represent the actual matrix of the device under test (DUT), the section of the PGGWG.

This method as described in [86] results in eight linear independent error terms of T_A and T_B and can be solved by the design and measurement of THRU, REFLECT and LINE standards. Thereafter, the DUT can be extracted as

$$T_{DUT} = T_A^{-1} T_m^{-1} T_B^{-1}$$

The THRU standard consist of a non-zero length of transmission line which sets the reference plane of the measurement at the middle of the standard. Figure 4.6(a) shows the layout of the THRU standards used. The THRU standard consist of a back-to-back CPW-PGGWG transitions.

The LINE standard as shown in Figure 4.6(b)) is $L_{ext} = \lambda/4$ longer than the THRU length at the geometrical mean of the frequency span at 33 GHz. The difference between the LINE and THRU is kept between 20° to 160° of the electrical length.

The REFLECT standard for this work is a short circuit as shown in Figure 4.6(c), with a short wall implemented in PGGWG consisting of three rows of round pad EBG's across the width of the groove.

A second TRL calibration kit in CPW is designed, setting the reference plane to the coaxial input. This is to enable the measurement and inclusion of the PGGWG transition. This was used to de-embed the effect of the connectors, moving the calibration plane to the CPW input of the transition.

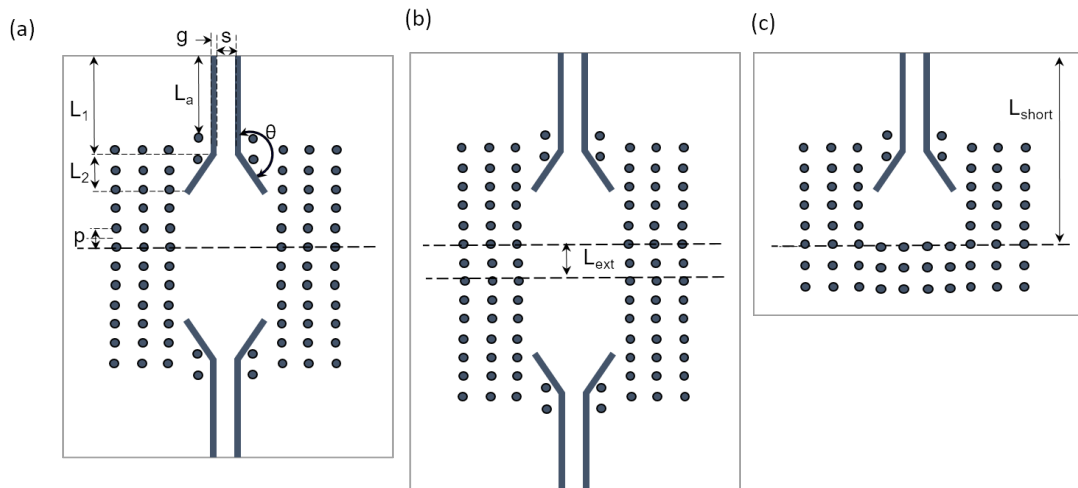


Figure 4.6: Schematic drawing of standard (a) Thru, (b) Line and (c) Reflect.

4.4 Fabrication Processes and Measurement Setup

A simple sequential build process using Park Electrochemical MercuryWave 9350 substrate material with $\epsilon_r = 3.5$ and loss tangent of 0.004, is used to manufacture the PGGWG.

The build stack-up is as shown in Figure 4.7. The EBG via holes are drilled through a thickness $h = 0.508$ mm of a single layer substrate core. These via holes are then electroplated with 17 micron copper. The round catch pad of the EBG is then etched on top of the vias as annular rings using a direct imaging method and copper plated. This is then followed by laminating a layer of prepreg (bond layer) with the same dielectric properties as that of the substrate material. The height of the prepreg filling is h_a . Finally, a 17-micron copper cladding is added onto the top of the prepreg surface for the top plate of the PGGWG structure. The fabricated TRL standards are shown in Figure 4.8.

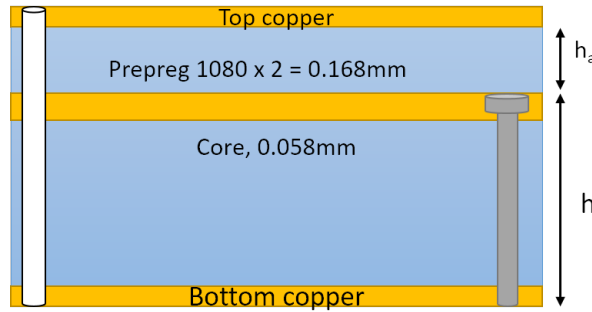


Figure 4.7: Stack-up used in the fabrication of the PGGWG.

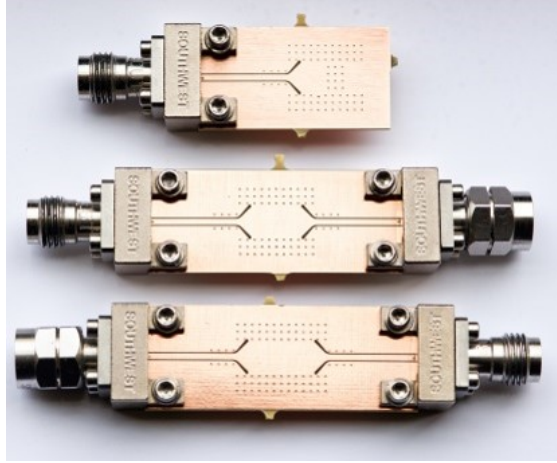


Figure 4.8: Fabricated PGGWG TRL standards.

There are however limitations to the fabrication process. A high level of fabrication precision is required to ensure the catch pad is kept at the same thickness through the entire structure to avoid a variation of impedance across the transmission line. The plating process creates an annular ring around the plated hole to form the round catch pad. This process does deposit additional copper, adding to the thickness of the round pad. This had to be sanded down to remove the excess copper, to ensure that the round catch pads are all levelled as well as maintain the gap height h_a across the structure.

Figure 4.9 shows the microscopic picture taken for the different sectional cuts of the PGGWG. Figure 4.9(b) shows the section cut X-X' across the CPW feedline. Figure 4.9(c) shows the sectional cut $X'_1-X'_1$.

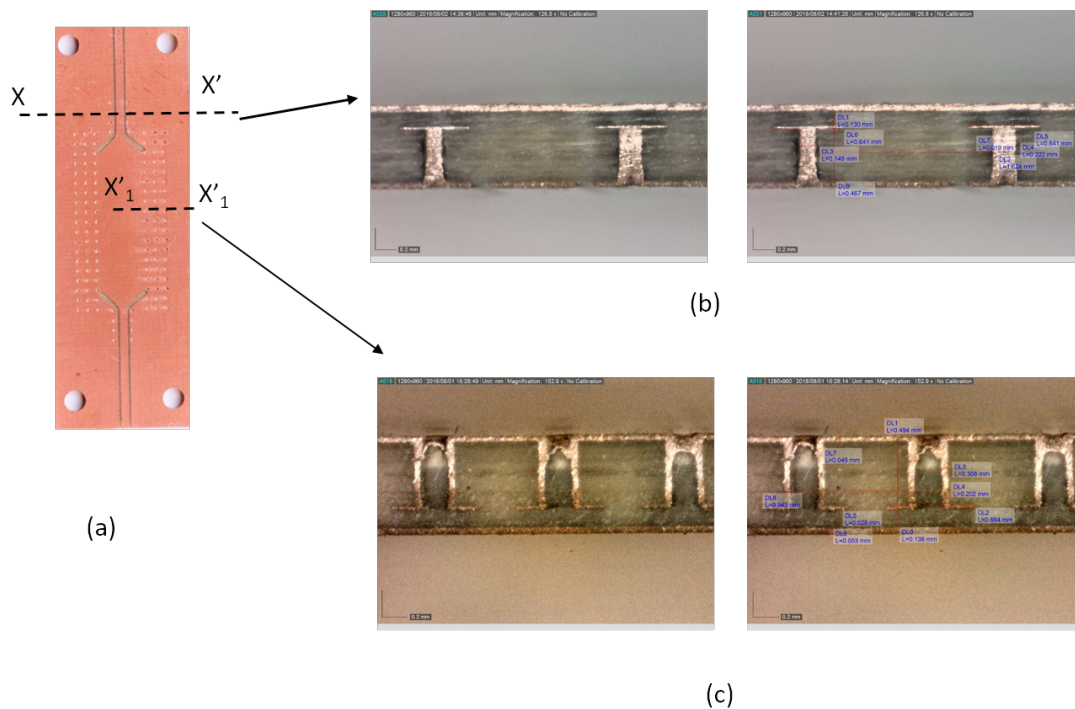


Figure 4.9: Microscopic picture showing the cross section of the fabricated circuit. (a) PGGWG circuit. (b) Cross section $X-X'$. (c) Cross section $X'_1-X'_1'$

As observed, there is some discrepancy in dimensions of the fabricated circuit as compared to simulated values in Table 4.1.

Non-plated holes corresponding to the connectors' mount positions were drilled on each PGGWG circuit to enable the clamping of the connector into position for measuring the circuits. This connector is specified for frequencies up to 67 GHz and is chosen over solder mount SMA connectors for ease of measuring the various PGGWG circuits.

A Keysight PNA-X N5247A vector network analyzer (VNA) was used to measure the circuits. An electronic calibration kit was used to move the calibration plane to the tip of the coaxial cable attached to the VNA. Figure 4.10 shows the lab setup.

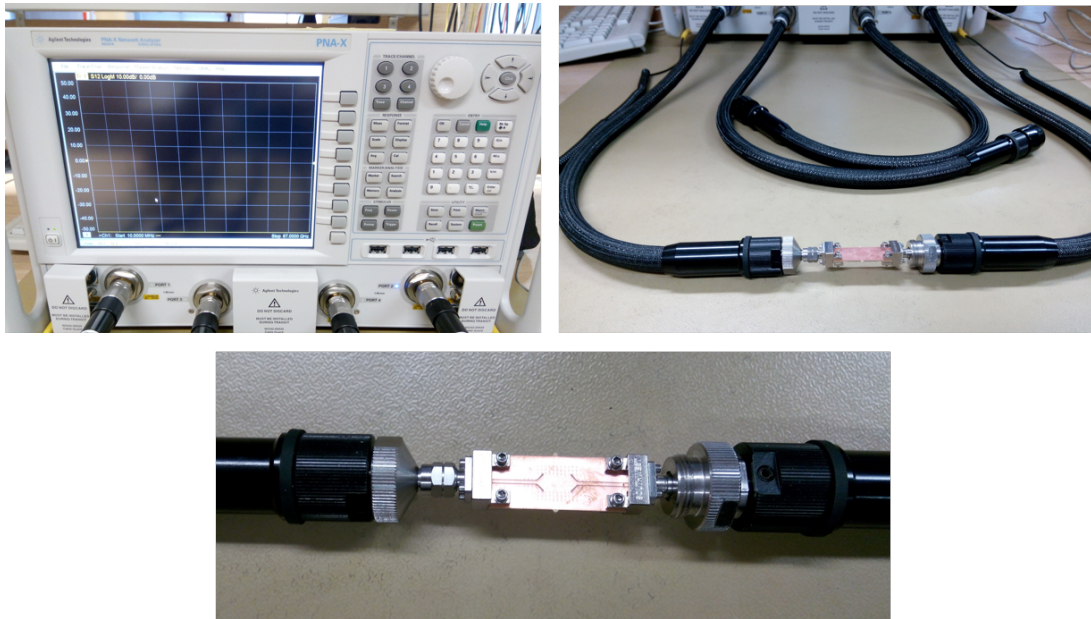


Figure 4.10: Experimental set-up for measuring the PGGWG circuits and TRL standards using the PNA-X N5247A network analyzer.

4.5 PGGWG Measurement Results and Comparison to Simulation

Figure 4.11 shows the measured S-parameters of the PGGWG with the transition from CPW to PGGWG included that is, de-embedded up to the CPW feed point. The CPW TRL calibration kit as discussed in Section 4.3 is used to de-embed the effect of the connectors in post-processing.

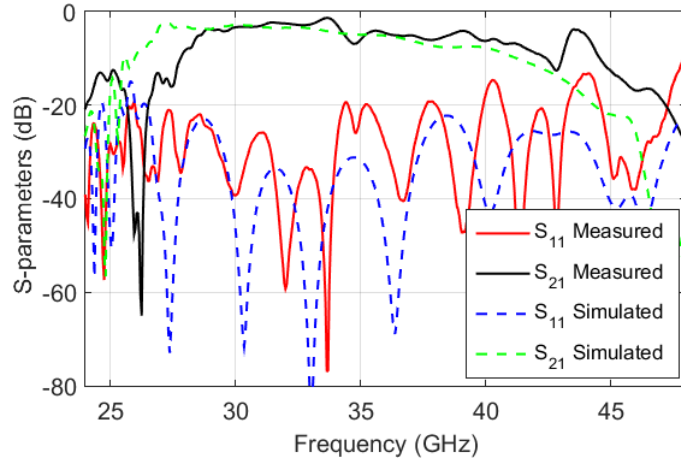


Figure 4.11: PGGWG simulation and measurement performance including the CPW-PGGWG transition of Figure 4.1.

From Figure 4.11, we observe the lower and upper frequency limit of the K_a -band PGGWG design example having dimensions $h = 0.508$ mm, $h_a = 0.168$ mm, $v_d = 0.3$ mm, $p_d = 0.7$ mm, $p = 0.95$ mm, $\epsilon_r = 3.5$ and $\tan\delta = 0.004$ and length of 28.26 mm. These results indicate that the CPW to PGGWG transition is effective at exciting the waveguide, as is evident from the agreement between the measured and simulated responses. The results present a wide passband from 28 GHz to 40 GHz, with 2.5 dB average insertion loss and 0.5 dB loss variation.

In Figure 4.12, the effect of both the coax connector and CPW-PGGWG transition are de-embedded using the method described in Section 4.3. It can be observed after TRL de-embedding in post processing on a 9.20 mm length of PGGWG that the waveguide features a passband with 1.2 dB average insertion loss and 0.5 dB insertion loss variation across the 28 GHz to 40 GHz band. The phase response of the PGGWG is shown in Figure 4.13. Good agreement between the simulated and measured de-embedded results were observed. This would indicate that the majority of the insertion loss observed in Figure 4.11 may, therefore, be attributed to the transition.

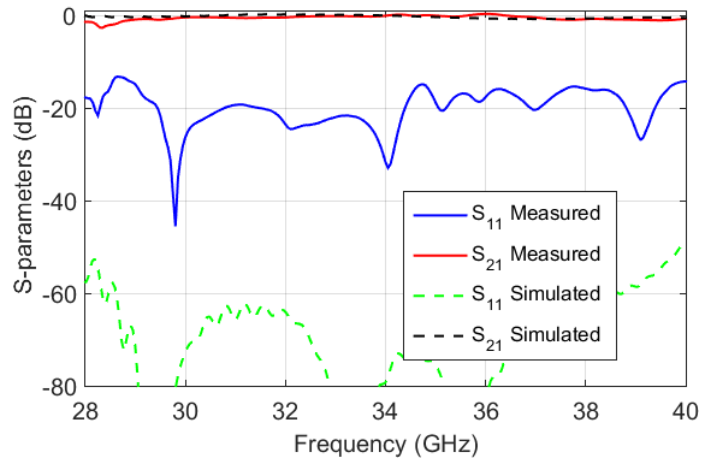


Figure 4.12: PGGWG simulation and measurement of S-parameter magnitudes with the CPW-PGGWG transition de-embedded.

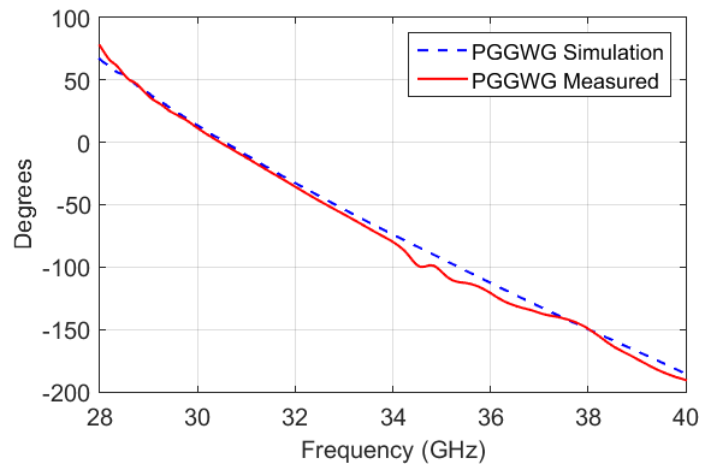


Figure 4.13: Transmission phase of the PGGWG simulation and measurement S-parameter magnitudes with the CPW-PGGWG transition de-embedded.

4.6 Conclusion

The proposed wideband transition from CPW to PGGWG presented here is shown to be an effective way to excite the fundamental TE_{10} mode within the PGGWG medium. By avoiding an electrical connection between the top and bottom conductors, DC isolation is maintained in the structure. Measured de-embedded results indicate an average insertion of 1.2 dB across the passband 28 to 40 GHz passband with a return loss of 18 dB for a length of PGGWG 9.20 mm.

Chapter 5 will present broadband propagation constant characterisation of the PGGWG, in comparison to SIW, based on these S-parameters.

Chapter 5

Broadband Propagation and Resonant Characterisation of Planar Groove Gap Waveguide

5.1 Introduction

This chapter presents the broadband propagation characterisation (28-40 GHz) of the PGGWG medium and a comparison to SIW implemented using identical substrates. It will be shown that the phase constant of PGGWG is nearly double that of comparable SIW, which may prove valuable in system miniaturisation.

This chapter also presents the arrangement of different PGGWG resonant cavities, showing the electric field of the fundamental TE_{101} resonant mode within the cavity. The unloaded quality factor of a rectangular PGGWG cavity is compared ¹ to an SIW rectangular cavity fabricated on the same soft substrate and stack-up arrangement.

¹ Comparable means the PGGWG and SIW were manufactured on the same substrate and for the same frequency band.

5.2 Propagation Constant Analysis of PGGWG

The propagation characteristics of a lossy transmission line of length l , in terms of attenuation constant α and phase constant β , can be characterized in matrix form as;

$$S_1 = \begin{bmatrix} 0 & e^{-\alpha l_1} e^{-j\beta l_1} \\ e^{-\alpha l_1} e^{-j\beta l_1} & 0 \end{bmatrix}$$

where $e^{-(\alpha+j\beta)l}$ is the S_{21} parameter of the transmission line S_1 . $\gamma = \alpha + j\beta$ is the complex propagation constant. l_1 is the length of the de-embedded PGGWG line as illustrated in Figure 5.1.

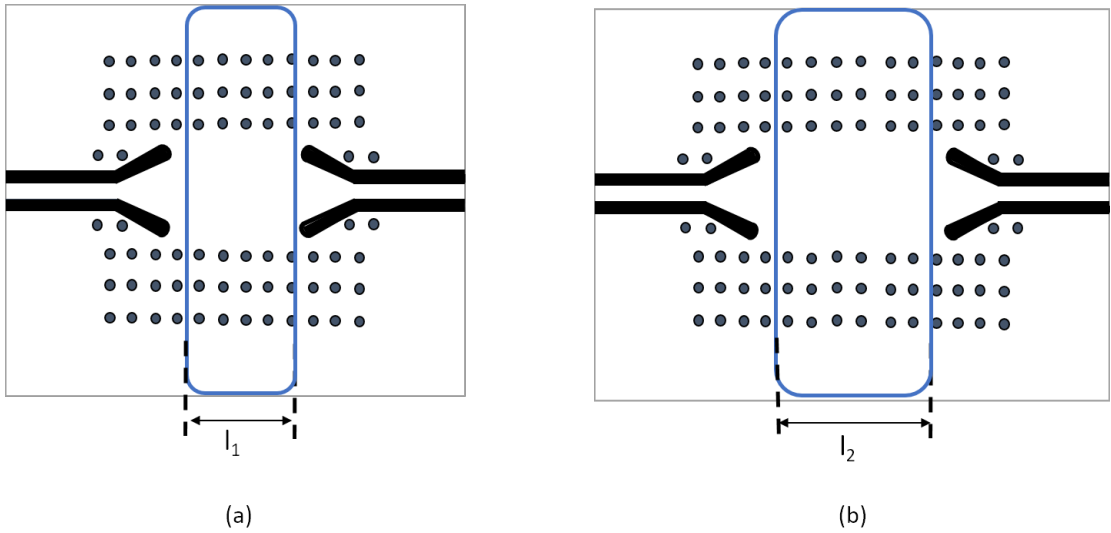


Figure 5.1: PGGWG transmission line of different lengths. (a) A section of the de-embedded PGGWG line length, l_1 . (b) A section of the de-embedded PGGWG line length, l_2 .

By applying the TRL de-embedding method as described in Section 4.3, the response of a section of the PGGWG alone, without the transition and connector, is obtained as shown in Figure 5.1. The attenuation constant, α (Np/m) of the line is extracted from a section of length, l_1 . This method has been used in a

recent developed decoupled empty substrate Integrated waveguide (DESIW) [26] to extract the propagation characteristics of the transmission line.

The phase constant β (rad/m) is derived from the phase difference of the two de-embedded lines l_1 and l_2 (Figure 5.1(a) and (b)) where

$$\beta = \frac{2\pi}{\lambda}$$

The S-parameters of a 7 mm length of PGGWG was obtained as described in Section 4.3. A similar process was followed for a 7 mm length of SIW line with [Grounded Coplanar Waveguide \(GCPW\)](#) transition similarly de-embedded using TRL standards in SIW.

The SIW transmission line was designed to have the TE_{10} mode cut-off at 28 GHz. The SIW line is $a_{siw} = 3.1$ mm wide, and formed by vias of diameter $v_{dsiw} = 0.3$ mm at pitch $p_{siw} = 0.45$ mm. This was implemented on the same substrate material as PGGWG with the same multi-layer stack-up of total height $h_{siw} = 0.618$ mm.

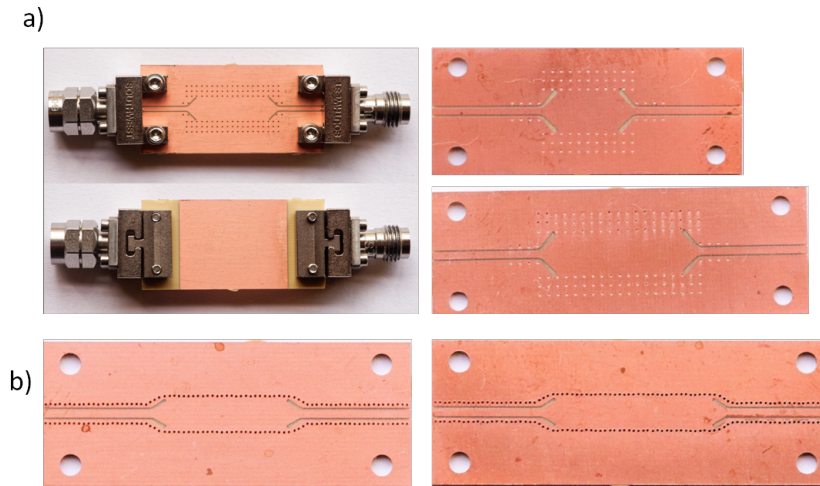


Figure 5.2: Fabricated prototype of the transmission lines. (a) PGGWG showing the bottom and top views with connector attachment. (b) SIW lines.

A series of PGGWG and SIW transmission lines are designed and manufactured as shown in Figure 5.2. The PGGWG line is shown in Figure 5.2(a) which consist

of two line lengths and the SIW lines in Figure 5.2(b).

The extracted attenuation constant α and phase constant β of the PGGWG and SIW are shown in Figure 5.3 and 5.4 respectively. The results indicate that the attenuation constant of PGGWG is higher than, but comparable to that of SIW. The attenuation was observed to be below 2.5 Np/m across the band of interest (28 - 40 GHz)

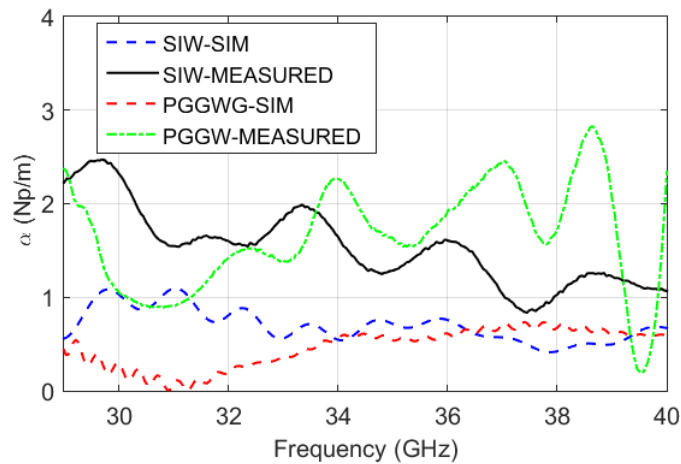


Figure 5.3: Attenuation constant(Np/m) of PGGWG and SIW

The phase constant, β , of the PGGWG in Figure 5.4 as well as the comparable SIW, shows good agreement between the measured and simulated results over the bandwidth of interest. At mid-band, a phase constant of approximately 1100 rad/m is observed.

The slope of the phase constant of the PGGWG is similar to that of SIW, but with an offset. The PGGWG has a higher phase constant, which means that the wavelength is shorter in PGGWG than in SIW at the same frequency. This would indicate, as seen from the phase velocity v/c_o of Figure 5.5, a slow-wave effect in the PGGWG which may be exploited for system miniaturisation.

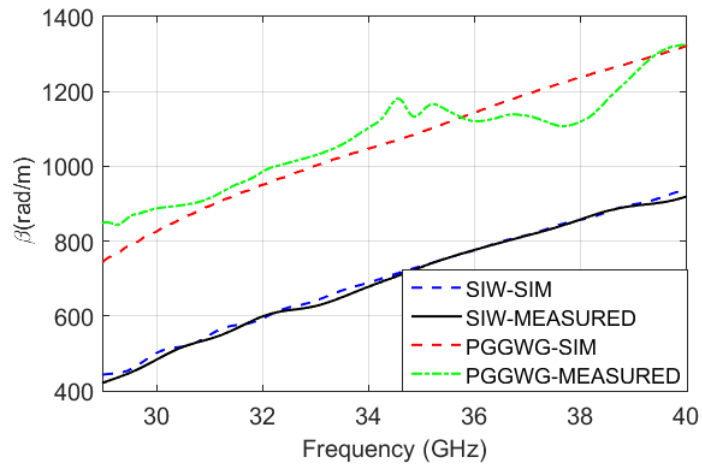


Figure 5.4: Phase constant (β/m) of PGGWG and SIW

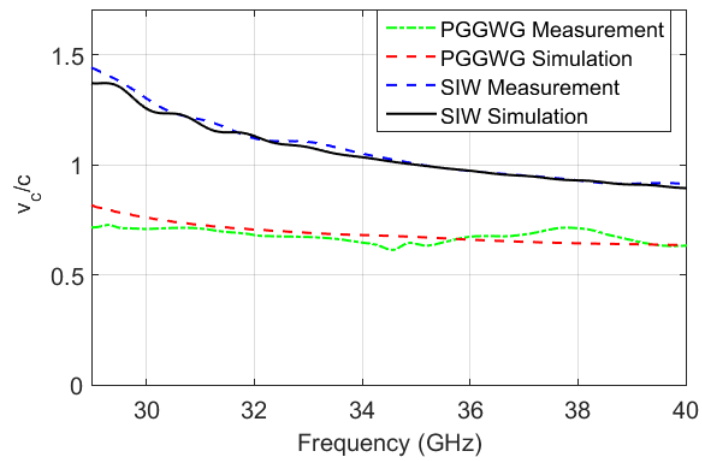


Figure 5.5: Phase velocity (v_c/c) of PGGWG and SIW

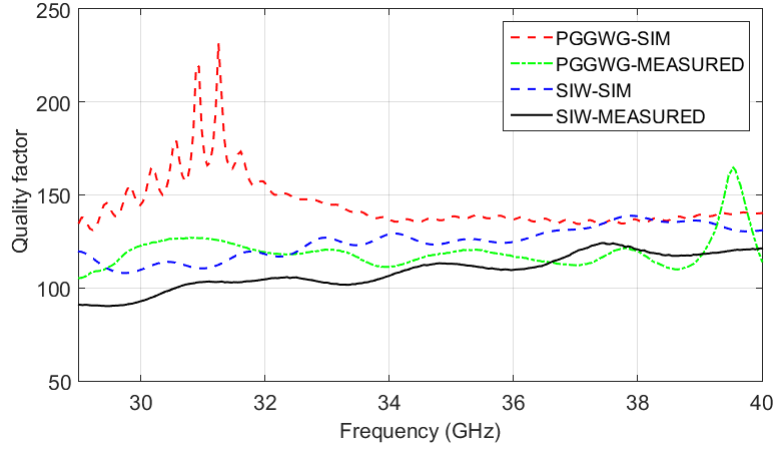


Figure 5.6: Transmission line Q-factor of PGGWG and comparable SIW

The transmission line Q-factor [87] is calculated as

$$Q_{TL} = \frac{\beta}{2\alpha}$$

for PGGWG and SIW, as shown in Fig. 5.6. The Q-factor of the PGGWG simulation result over the usable bandwidth remains fairly constant at $Q_o = 138$. As observed, the Q-factor of PGGWG is slightly higher than SIW over the band of interest with spikes at about 31 GHz of the PGGWG simulation result due to the low extracted value of the attenuation constant.

5.3 Planar Groove Gap Waveguide Resonant Cavities

PGGWG resonant cavities can be formed using the embedded EBGs to form the cavity walls. Different cavity shapes such as a rectangular, square and circular were considered. Figure 5.7 shows these cavities with each cavity wall formed with at least three rows of EBG blind vias. This provides sufficient attenuation of the parallel plate mode, as observed from the corresponding electric field distribution of the fundamental resonant mode within the cavities. Results were obtained using the Eigenmode solver in CST.

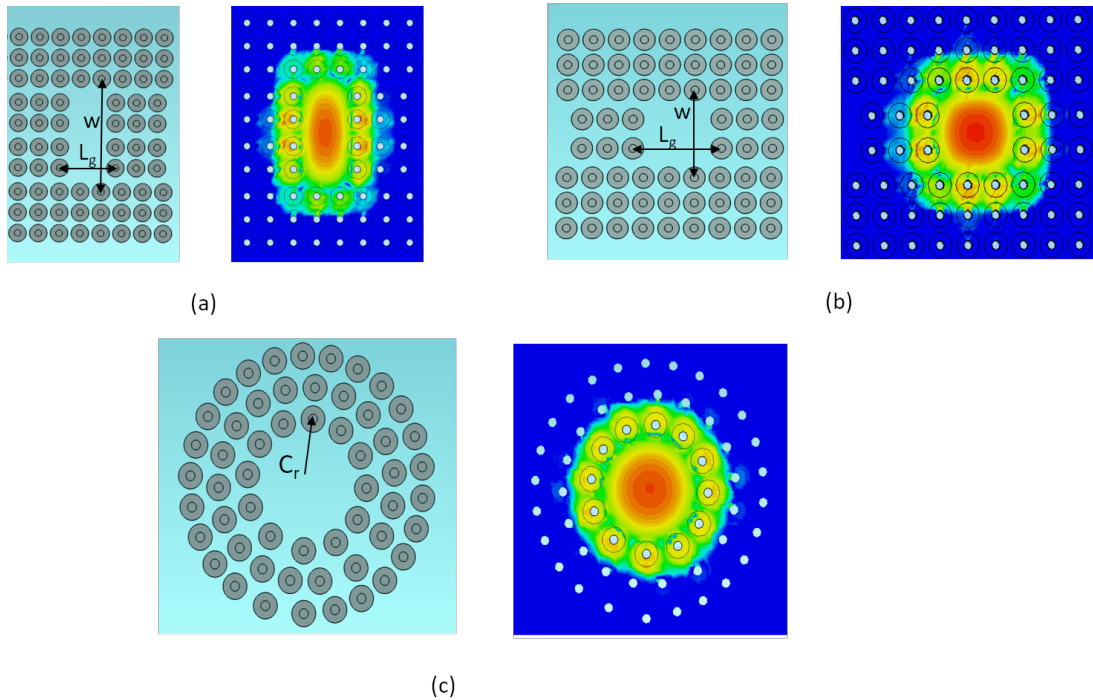


Figure 5.7: Different PGGWG resonant cavity arrangements with electric field distributions. (a) Rectangular cavity. (b) Square cavity. (c) Circular cavity.

The dimensions of the cavities in Figure 5.7 and resonant frequency of their fundamental modes are given in Table 5.1.

Table 5.1: Dimensions of PGGWG resonant cavities

	Dimensions	(mm)	f_o (GHz)
Rectangular Cavity	w	5.20	37.84
	L_g	2.55	
Square Cavity	w	3.30	36.0
	L_g	3.30	
Circular Cavity	C_r	2	33.02

The PGGWG rectangular cavity in Figure 5.7(a) is created in a similar arrangement to that of a rectangular resonant cavity in SIW. The length of the resonant cavity L_g is chosen to be $\lambda_g/2$ at f_o . The magnitude of the electric field distribution of the fundamental TE_{101} resonant mode within the cavity is well confined to the first two rows of the EBG via cavity wall as shown.

Figure 5.7(b) shows the square cavity arrangement where the width, w , of the groove is equal to the length of the resonant cavity $L_g = \lambda_g/2$ at f_o . A reduction in the width of the groove w increases the cut-off frequency of the fundamental propagating mode of the waveguide allowing for a square cavity at the expense of reduced operating bandwidth of the surrounding system. The simulated electric field distribution of the TE_{101} resonant mode is confined within the cavity walls with clear field suppression within the first two EBG via rows.

The circular PGGWG resonant cavity is shown in Figure 5.7(c). The radius of the cavity C_r can be varied to achieve the desired resonant frequency.

5.4 Quality Factor of PGGWG Resonant Cavity

The quality factor Q of a resonator gives much useful information of the loss in a resonant circuit [11]. It is a measure of the energy loss and that dissipated in a resonator relative to the stored energy.

The loaded quality factor $Q(Q_L)$ can be expressed as [11]

$$\frac{1}{Q_L} = \frac{1}{Q_U} + \frac{1}{Q_E} \quad (5.1)$$

where Q_U is the unloaded quality factor, which relates to the loss in the resonant circuit. Q_E is the external quality factor due to the loss contributions by the coupling circuit and the feed network to the resonator. Q_E can be expressed in terms of S_{21} from a 2-port excitation as:

$$S_{21}(dB) = 20 \log\left(\frac{Q_L}{Q_E}\right)$$

with Q_E expressed as

$$Q_E = 10^{-[S_{21}(dB)/20]Q_L}$$

The unloaded Q factor can therefore be expressed as

$$Q_U = \frac{Q_L}{1 - S_{21}}$$

For weakly coupled resonators, such that the amplitude of the transmission coefficient S_{21} is quite small and unaffected by the measurement, Q_U can be approximated to Q_L [88], [89] with

$$Q_L = \frac{f_o}{\Delta f_{3dB}} \quad (5.2)$$

This method was used to extract the unloaded quality factor of the PGGWG resonator, as well as the SIW cavity from the 2-port S-parameter simulation. The PGGWG cavity is excited using a CPW feed through weak input and output coupling while the comparable SIW cavity was fed using a similar GCPW scheme. Light coupling is used to ensure minimal loading effects, making $Q_U \approx Q_L$.

The dimensions of the rectangular resonant cavity for the PGGWG and SIW for comparison are as shown in Table 5.2. Simulations indicate resonant frequencies of 33.64 GHz and 33.46 GHz for the PGGWG and SIW cavities, respectively. Figure 5.8(a) shows the geometry of the PGGWG cavity with L_s representing the length of the SIW cavity while a_{SIW} denotes the width of the SIW in Figure 5.8(b). Also shown in Figure 5.8 is the magnitude of the electric field distribution of the fundamental TE_{10} mode within the PGGWG and SIW cavities. The substrate h_{SIW} is commensurate to the sum of the substrate heights, h and h_a of the PGGWG. The via diameter of the PGGWG circuit and SIW is kept constant.

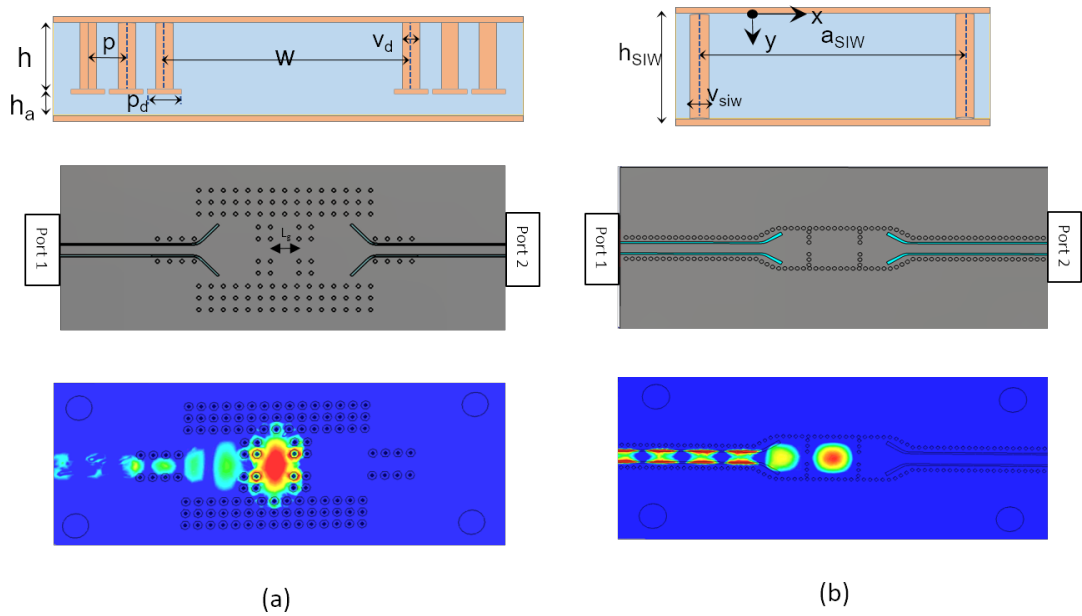


Figure 5.8: Resonant cavities with geometry layout, dimensions and magnitude of the electric field of the fundamental TE_{101} resonant mode (a) PGGWG rectangular cavity (b) SIW rectangular cavity.

Table 5.2: Dimensions of the rectangular resonant cavities in PGGWG and SIW

PGGWG (Dimensions in mm)		SIW (Dimensions in mm)	
h	0.508	h_{siw}	0.618
h_a	0.168	p_{siw}	0.45
w	5.48	a_{siw}	3.40
v_d	0.3	v_{dsiw}	0.3
p_d	0.7		
p	0.95		
L_g ($\lambda_g/2$)	2.80	L_s ($\lambda_g/2$)	3.70
f_o	33.64 GHz	f_o	33.46 GHz

The required length of the cavity, L_g ($\lambda_g/2$), in PGGWG is significantly shorter than that of SIW ($L_s = \lambda_g/2$). This is as a result of PGGWG having a shorter wavelength than that of SIW at the resonant frequency, as observed in Figure 5.9.

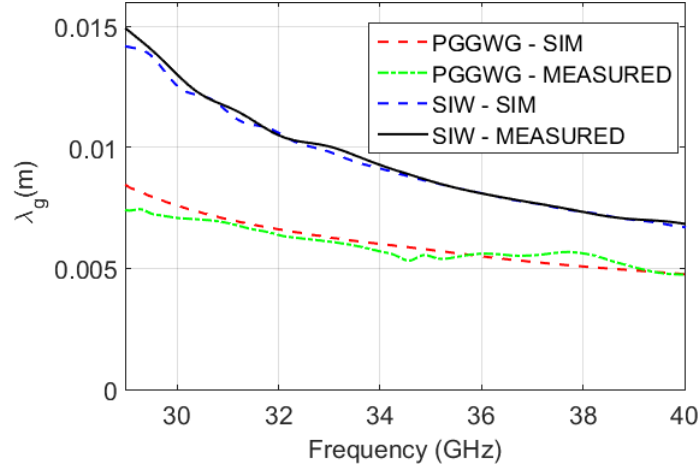


Figure 5.9: Guided wavelength, λ_g , of PGGWG and comparable SIW, extracted from the phase constant of PGGWG and SIW.

Figure 5.10 shows the simulated and measured S_{21} (dB) of the 2-port coupled PGGWG and SIW cavities, as well as the fabricated devices. The measured results are de-embedded to the CPW plane. The frequency shift between mea-

surement and simulation of Figure 5.10(a) is about 0.3%. This difference can be attributed to the fabrication of the PGGWG circuit as described in Section 4.4.

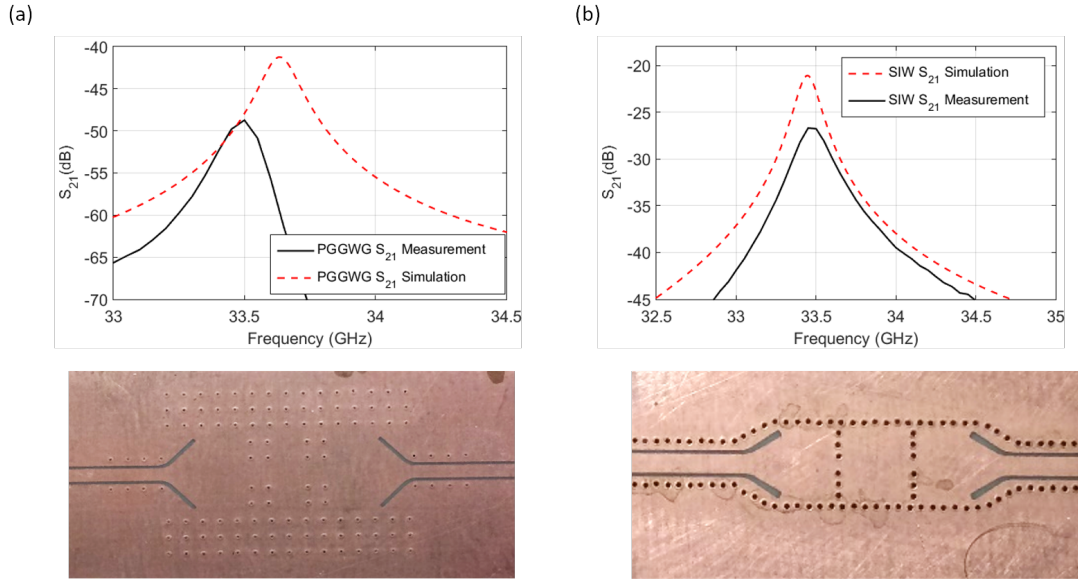


Figure 5.10: S_{21} (dB) of the 2-port excitation for the weakly excited rectangular resonant cavities (a) PGGWG (b) SIW.

Table 5.3 presents a comparison between of the Q -factors obtained from the PGGWG and SIW cavities from the same substrate multilayer stackup. The extracted Q_u values shows that the PGGWG resonator has Q_u of 209 comparable to that of SIW (221). A direct comparison of Ka-band resonator quality factor between PGGWG and SIW indicates comparable performance of 209 and 221 respectively from measured results, at around 33.5 GHz with PGGWG showing high Q_u factor than SIW from simulation. This discrepancy between simulation and measured Q_u factor results of the PGGWG can be attributed to the manufacturing of the PGGWG cavity.

Table 5.3: Q-factor comparison between PGGWG and SIW from rectangular resonant cavities implemented using the same substrate material and identical stackup

	SIMULATION		MEASUREMENT	
	f_0 (GHz)	Q_u	f_0 (GHz)	Q_u
PGGWG	33.64	261	33.51	209
SIW	33.46	223	33.46	221

5.5 Conclusion

This chapter presented the broadband characteristics of the PGGWG in comparison to SIW, implemented on the same multi-layer substrate material and frequency band. It is found that PGGWG exhibits higher but comparable loss, making the PGGWG a viable and competitive planar waveguide medium. In addition, due a higher phase constant of PGGWG, it can be employed for miniaturization depending on the percentage board space occupied by the EBG walls.

It is shown that different resonant cavity shapes can be implemented in PGGWG. A direct comparison of a rectangular resonant cavity at K_a -band shows that lower, but comparable Q_u between PGGWG and SIW is achieved. It was also found that the length of the resonant cavity, $\lambda_g/2$, of PGGWG is shorter than SIW at approximately the same resonant frequency supporting the broadband slow-wave observation.

Chapter 6

Tunable Planar Groove Gap Waveguide Cavity

6.1 Introduction

This chapter presents a tunable PGGWG resonant cavity showing how the DC isolation property can be exploited for device biasing. Details of the varactor inclusion on the resonant cavity are presented and discussed, as well as the simple DC biasing scheme for the varactor diode employed. It is shown that varactor tuning is possible without bridging wires or concentric etched rings.

6.2 Tunable Cavity Geometry

The classical combline resonator topology [90] is adapted here in the design of a continuously tunable PGGWG cavity resonator. This cavity arrangement has been demonstrated in SIW and has been applied in VCOs [91] and SIW combline filters [92].

The geometry of the proposed PGGWG cavity is shown in Figure 6.1. This is a rectangular resonant cavity with EBG via rows each capped with a round catch

pad used to form the cavity walls as described in Section 5.3. The length of the cavity, L_g is set to ensure the fundamental TE_{10} mode resonates in the cavity while the coupling to the cavity, set by the iris width C_g , is intentionally chosen as a low value to minimize loading effects.

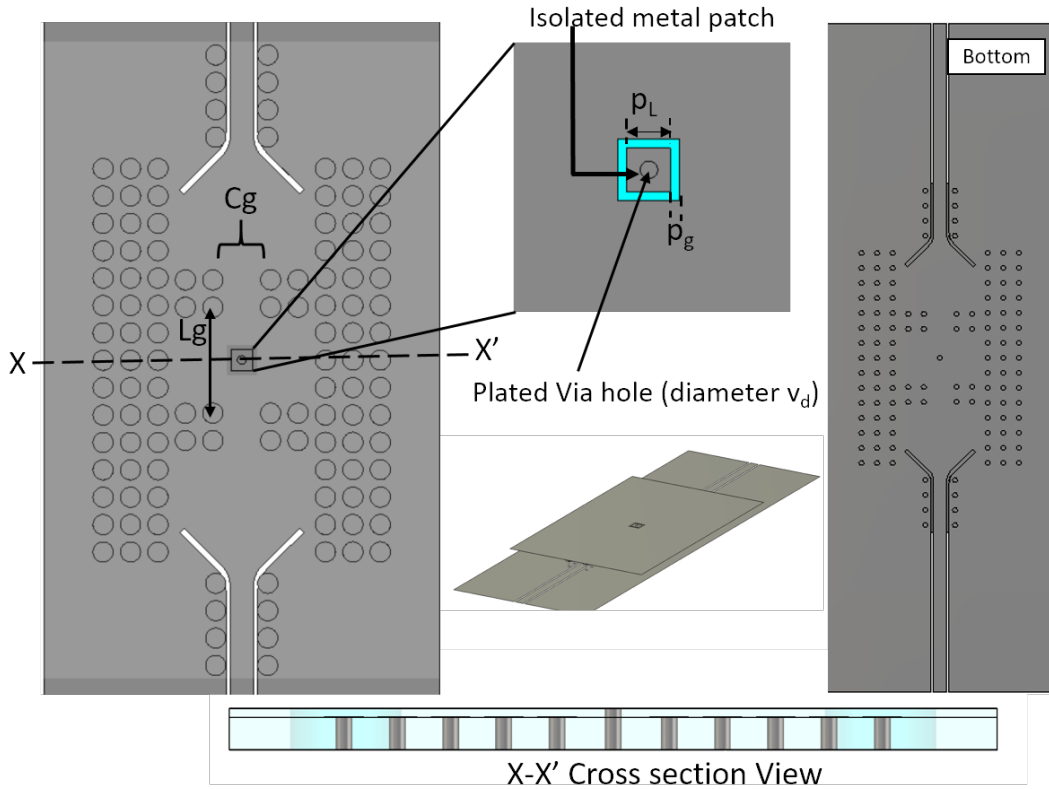


Figure 6.1: PGGWG rectangular resonant cavity structure showing the top and bottom of the cavity with the isolated floating metal patch on the top plane.

A conducting post of diameter $v_d = 0.3$ mm is inserted at the centre of the cavity as a through-hole plated via which connects the isolated patch at the centre of the cavity to the bottom conducting plane of the PGGWG cavity. The etched gap of width p_g ensures DC isolation despite the through-hole via in the middle of the cavity.

The gap, p_g , creates a capacitive loading between the centre post and the top metal layer of the PGGWG through the fringing fields across the gap.

Table 6.1: Dimensions of the tunable PGGWG rectangular resonant cavity

Parameter	Value (mm)
w	5.48
h	0.508
h_a	0.168
v_d	0.3
p_d	0.7
p	0.95
p_L	0.75
p_g	0.15

The cavity is designed on the same PCB stackup used in previous experiment, using MercuryWave 9350 substrate. The dimensions of the PGGWG cavity waveguide are shown in Table 6.1.

Figure 6.2 shows the electric field vector plot inside the cavity from the cross section cut X-X' of the cavity in Figure 6.2(a). It can be seen in Figure 6.2(b) that the E-field is contained within the cavity walls with fringing fields across the gap p_g on the top plate of the PGGWG.

From the plot of S_{21} in Figure 6.2(c), a resonant frequency at 31.61 GHz and an unloaded quality factor Q_u of 140 is calculated, which is lower than the Q_u of 261 calculated in Section 5.4. The reduction in quality factor is attributed to the loading on the cavity, as is evident from the observed radiated E-field in Figure 6.2(b).

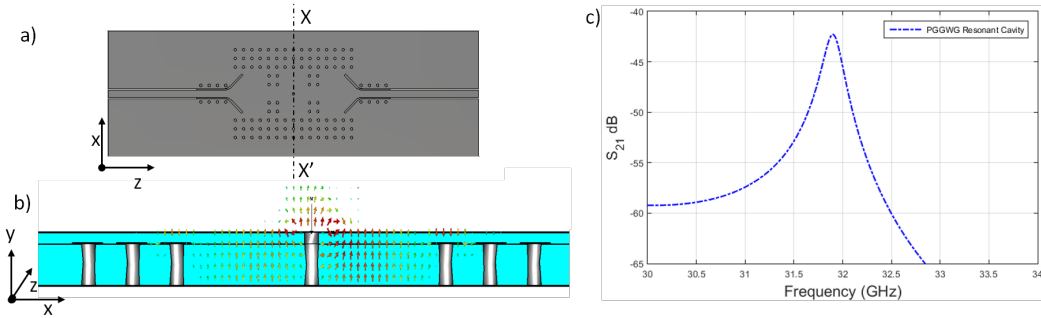


Figure 6.2: PGGWG rectangular resonant cavity. (a) Bottom view of the cavity. (b) Electric field vector plot inside the cavity from cross section view X-X'. (c) Magnitude of S_{21} (dB).

6.3 Varactor Loading and DC Biasing

The loading capacitance C_g between the top isolated patch and the top metal plate of the PGGWG can be controlled electrically by placing a varactor diode in reverse bias across the gap.

As a direct comparison of the DC biasing method applied to SIW resonant cavity in [31], the DC and RF paths for both the SIW and PGGWG resonant cavities are shown in Figure 6.3.

The DC path in PGGWG, as shown in Figure 6.3(a) (obtained from the cross section of the cavity in Figure 6.3(b)), flows from the DC voltage source through a radial stub, then across the varactor diode in reverse bias, down to ground through the centre via of the floating centre square patch and back up through a via outside the PGGWG cavity to the DC source. This is in contrast to the SIW example (Figure 6.3(d)), where multiple cut-outs and a bridging wire are needed on the top conductor to achieve DC isolation for biasing, as the top and bottom conductor are at the same DC potential observed in Figure 6.3(e).

The RF current in the PGGWG (Figure 6.3(a)) flows up through the centre via, through the varactor diode connected across the gap and then through the

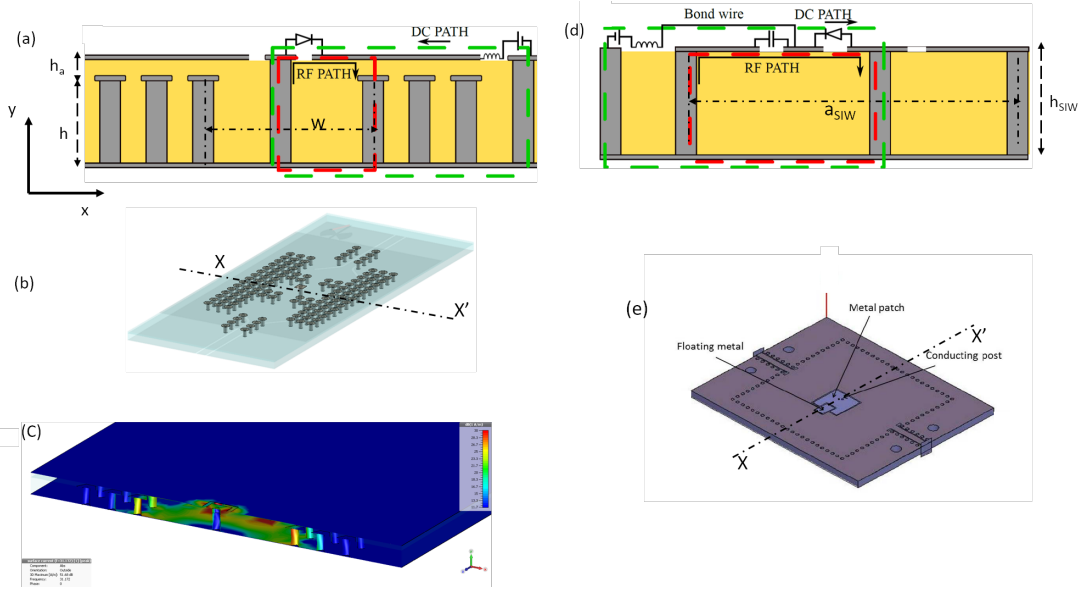


Figure 6.3: Illustration of the DC and RF paths of PGGWG and SIW (a) RF and DC path in PGGWG rectangular resonant cavity from cross section X-X'. (b) 3D view of the PGGWG resonant cavity geometry. (c) Current plot of the cross section X-X'. (d) RF and DC path in SIW rectangular resonant cavity from cross section X-X'. (e) SIW tunable cavity geometry. Taken from [31], ©2011 IEEE.

AMC. This is evident from the surface current plot shown in Figure 6.3(c). The RF path of SIW (Figure 6.3(d)), implemented in [31], requires an additional DC blocking capacitor in series with the varactor diode back to ground. This is used to reduce the capacitive effect of the varactor in order to improve the quality factor of the resonator.

6.3.1 Biasing coupled, cascaded resonators

This biasing scheme is, however, complicated when considering two cascaded resonators requiring separate DC bias tuning. In the PGGWG structure, the z-directed surface current on the broadside walls of the TE_{10} propagating mode would clearly be perturbed by the DC isolating slots required by separate control voltages. This is a limitation in the sequential tuning of the cavities with differ-

ent bias voltages in this structure. This is disadvantageous in realising tunable coupled resonator filters over a wide band, or to control both passband centre frequency and passband bandwidth; especially if not only resonators, but also inter-resonator coupling, has to be tuned [93].

However, for a narrowband filter application, it has been shown in [94] that it is possible to apply the same bias voltage to the resonators and achieve similar tuning range. This was practically demonstrated by a third order filter with a 20% FBW providing a 30% tuning range [94]. The effect of using distinct tuning voltages is also detailed and shows that the improvement is marginal. It is, therefore, not necessary to implement a more complex biasing scheme. It is also possible to control the tuning response for a specific type of wideband filter with a single biasing voltage, as was demonstrated for a radio astronomy receiver filter in [95].

In [3], the effect of using different tuning voltages to tune the bandwidth and center frequency of the filter was explored with a larger tuning ratio obtained with co-tuned voltages.

Thus, simultaneous tuning of the cavities by using the top DC isolated plane for the DC bias line is conceptually possible and could be considered for future work. This is discussed in more detail in Chapter 7.1

6.4 Varactor Diode Selection

The following considerations are made in selecting an appropriate varactor diode for this experiment.

- Abrupt and hyperabrupt junction varactors based on Gallium Arsenide (GaAs) material is best suited to millimeter-wave frequency operation. This is because, at K_a-band, silicon varactor diodes suffer from low Q-factors and are not recommended for high-frequency applications [3].
- The quality factor of the varactor diode affects the unloaded Q of the cavity

resonator. The Q for a tuning varactor is given by $Q_{(-v)} = \frac{1}{2\pi f R_{-v} C_{-v}}$

where f is the operating frequency, C_v is the junction capacitance, and R_v is the series resistance of the diode from the resistance of the undepleted region of the epilayer [96]. From the equation, the Q factor is dependent on the operating frequency as well as the reverse bias voltage applied. A higher Q factor equates to lower energy dissipation and therefore, higher operating frequency limit [96].

- Another important parameter to consider in selecting a suitable varactor diode is the absolute capacitance value as well as the capacitance-to-voltage ratio of the diode. From the capacitance-voltage curves of the varactor diode, the required capacitance range over the DC voltage applied can be deduced [96].
- The packaging parasitic of the varactor diode operating at millimeter wave frequencies needs to be taken into consideration. This data is usually included in the datasheet of the varactor. The package parasitics include the parasitic capacitance and inductance as a result of the geometry of the diode packaging [96, 97]. It is important to take into account this effect in simulation to effectively predict the behavior of the diode.

In this experiment, the MACOM 46580 series varactor diode is used [97]. The SPICE model is shown in Figure 6.5 with the SPICE model parameters values. The package parasitics of the varactor diode, C_p and L_s , parasitic capacitance and inductance respectively are included in the model. The datasheet of the varactor is available in Appendix B. The varactor diode is attached to the PGGWG cavity as shown in Figure 6.4.

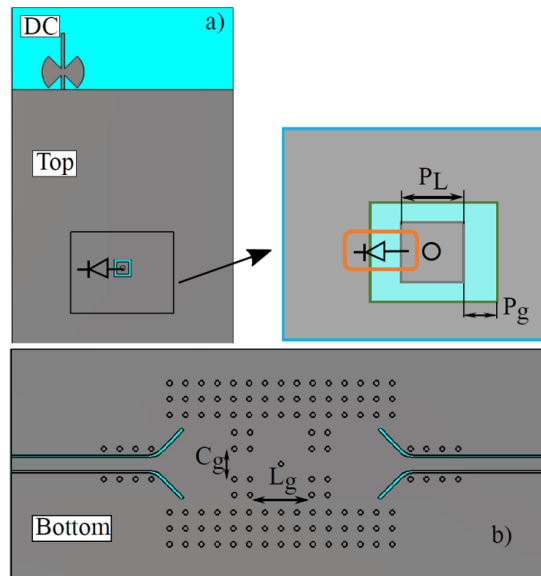


Figure 6.4: PGGWG rectangular resonant cavity structure. (a) Top view showing the connection of the varactor diode. (b) Bottom view.

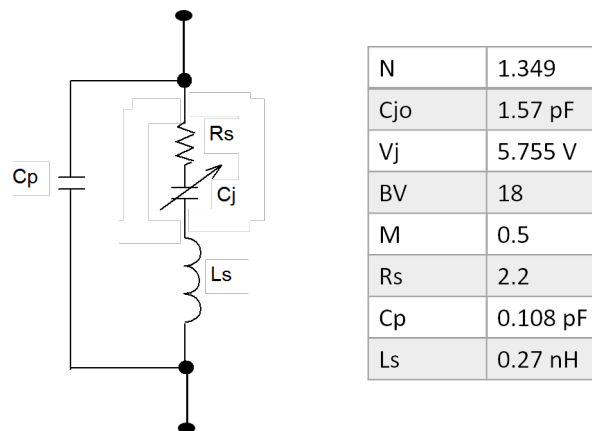


Figure 6.5: SPICE model of the MACOM 46580-276 varactor diode.

A tuning capacitance value of 0.13 pF to 0.45 pF can be obtained with this varactor diode using a reverse bias voltage range of 0V to 16V.

The varactor diode is first modelled as a passive lumped element capacitor placed

across the cut-out gap P_g in the 3D EM simulation model setup of the cavity. The capacitance range C_0 of 0.13 pF to 0.45 pF is simulated to observe the possible tuning range that might be achieved from these values.

Figure 6.6 shows the S_{21} (dB) of the 2-port excited resonant cavity with different values of varactor capacitance. The simulation indicates a continuous tuning range from 31.2 GHz to 32.82 GHz with an unloaded quality factor, Q_u ranging from 143 at higher values of C_0 to 163 for lower values of C_0 . It was also observed that, as the capacitance value C_0 increases from 0.35 pF to 0.45 pF, the variation in the resonant frequency is only 0.83%, with larger tuning range observed from capacitance value of 0.15 pF to 0.35 pF.

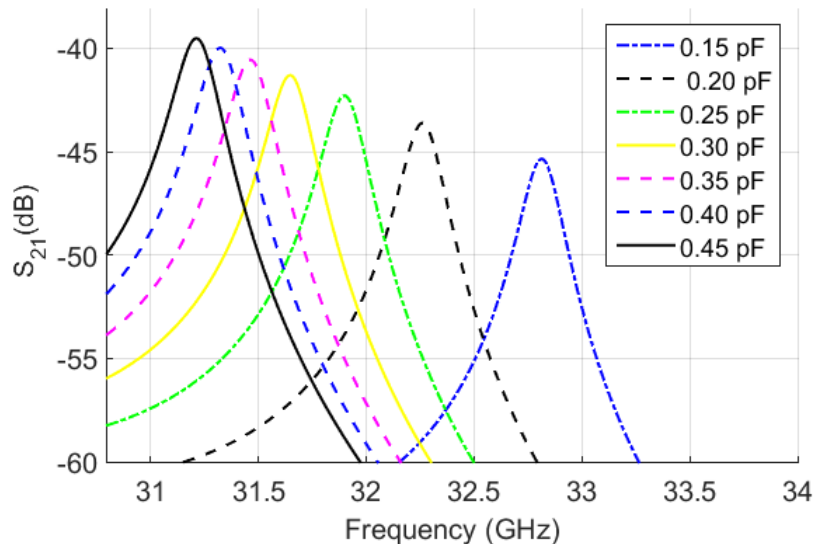


Figure 6.6: Simulation results obtained using lumped element capacitance, C_o , applied to the PGGWG resonant cavity

6.5 Hybrid EM-Circuit Simulation

A hybrid 3D EM-circuit co-simulation is performed in CST Microwave Studio using the time domain solver. The equivalent circuit model of the varactor diode is interfaced with the 3D model in CST Design Studio environment. Internal ports were created (in place of the capacitor used previously) for the varactor

and the input DC voltage. The EM-circuit co-simulation setup is shown in Figure 6.7 with the parasitics of the varactor diode included.

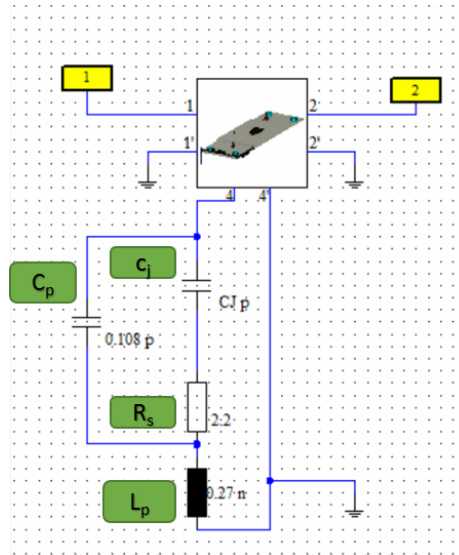


Figure 6.7: 3D EM-circuit Co-simulation set-up showing the equivalent circuit model for MACOM 46461-276 varactor diode connected.

C_p and L_p are the fixed parasitic capacitance and inductance of the diode packaging. R_s is the variable series resistance of the diode die and C_j is the variable junction capacitance of the diode die.

A butterfly stub is designed to present an RF open circuit at the point of contact with the top plate of the PGGWG cavity and an RF short circuit at the DC side of the stub, as shown in Figure 6.4. Due to the DC isolated planes of the PGGWG, the butterfly stub can be attached to any location on the top plane of the PGGWG cavity, eliminating the need for bridging wires to connect the bias line to the varactor diode.

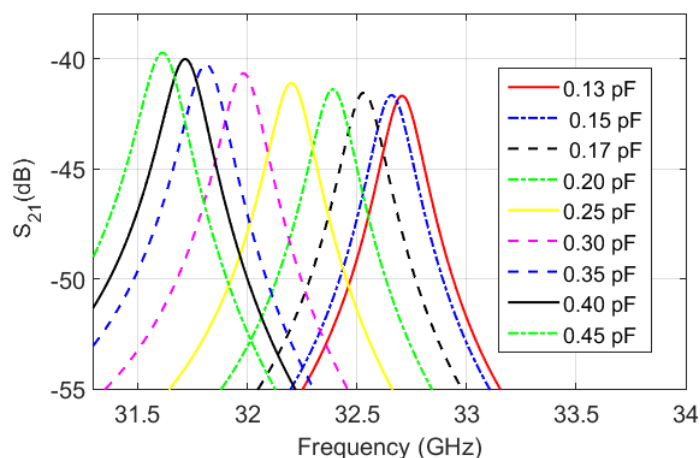


Figure 6.8: EM co-simulation result of S_{21} (dB) of the 2-port loaded rectangular PGGWG cavity using the equivalent circuit model of MACOM 46580 varactor diode.

The varactor diode in reverse bias is connected across port 4-4' (cathode to the bulk upper conductor, anode to the grounded patch). Port 1-1' and port 2-2' are waveguide ports corresponding to the input and output ports of the PGGWG resonant cavity.

The resulting S-parameters in Figure 6.8 indicate that a variation of f_0 from 31.63 to 32.71 GHz (3.36% tuning range) is achieved by varying the junction capacitance from 0.15 pF to 0.45 pF. The unloaded Q-factor varies over the tuning range from 143 to 160.

Different tunable resonant cavity geometries are also investigated, in addition to the rectangular PGGWG cavity. These include a circular PGGWG cavity, a square PGGWG cavity, as well as a rectangular cavity implemented using a square pad EBG embedded structure as opposed to the round pad. The same biasing scheme and varactor is applied to these cavities. Figure 6.9 shows the geometries under test.

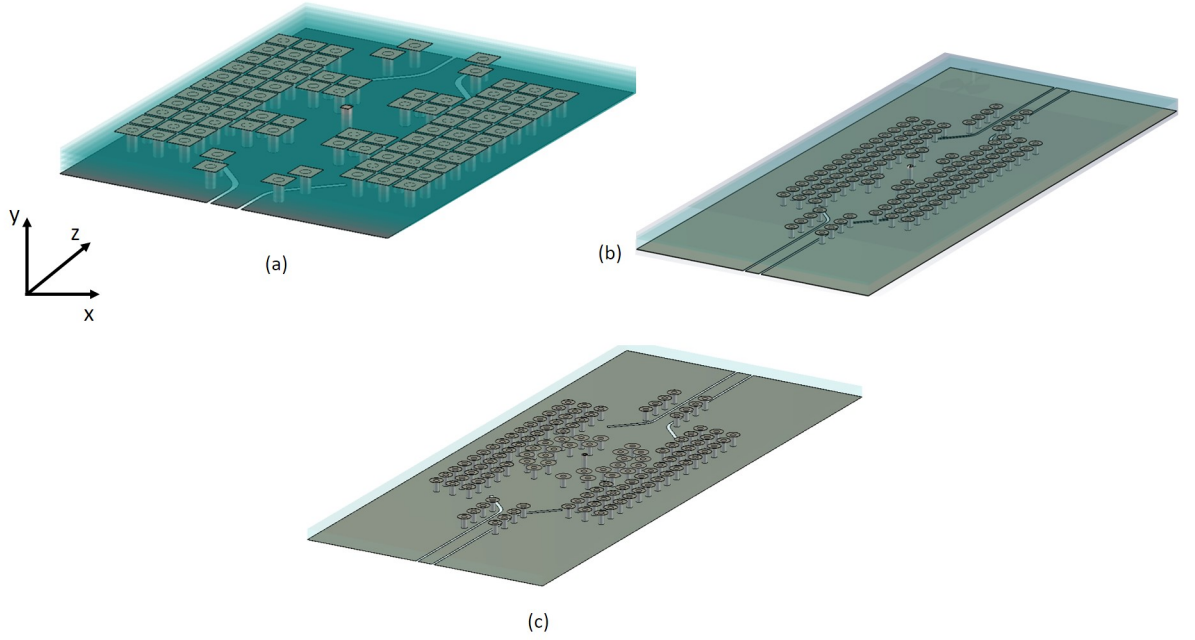


Figure 6.9: 3D models of different PGGWG resonant cavities. (a) Square patch EBG implementation of a rectangular cavity. (b) Square resonant cavity with a round EBG patch implementation (c) Circular resonant cavity with a round EBG patch implementation.

The dimensions of the waveguide in Figure 6.9 are kept the same as presented in Table 6.1 of Section 6.2. The cavity length, $L_g = 2.7$ mm for the rectangular resonant cavity implemented using the square patch EBG (Figure 6.9(a)). In the case of the square PGGWG resonant cavity in Figure 6.9(b), the cavity length, $L_g = 3.6$ mm is the same as the width w of the groove of the waveguide. The radius C_r of the circular resonant cavity of Figure 6.9(c) is 2 mm measured from the centre of the cavity to the first circular rows of EBG vias as shown in Section 5.3.

Figure 6.10(a) shows the variation in resonant frequencies of a rectangular cavity implemented with a square EBG catch pad. Figure 6.10(b) shows the variation

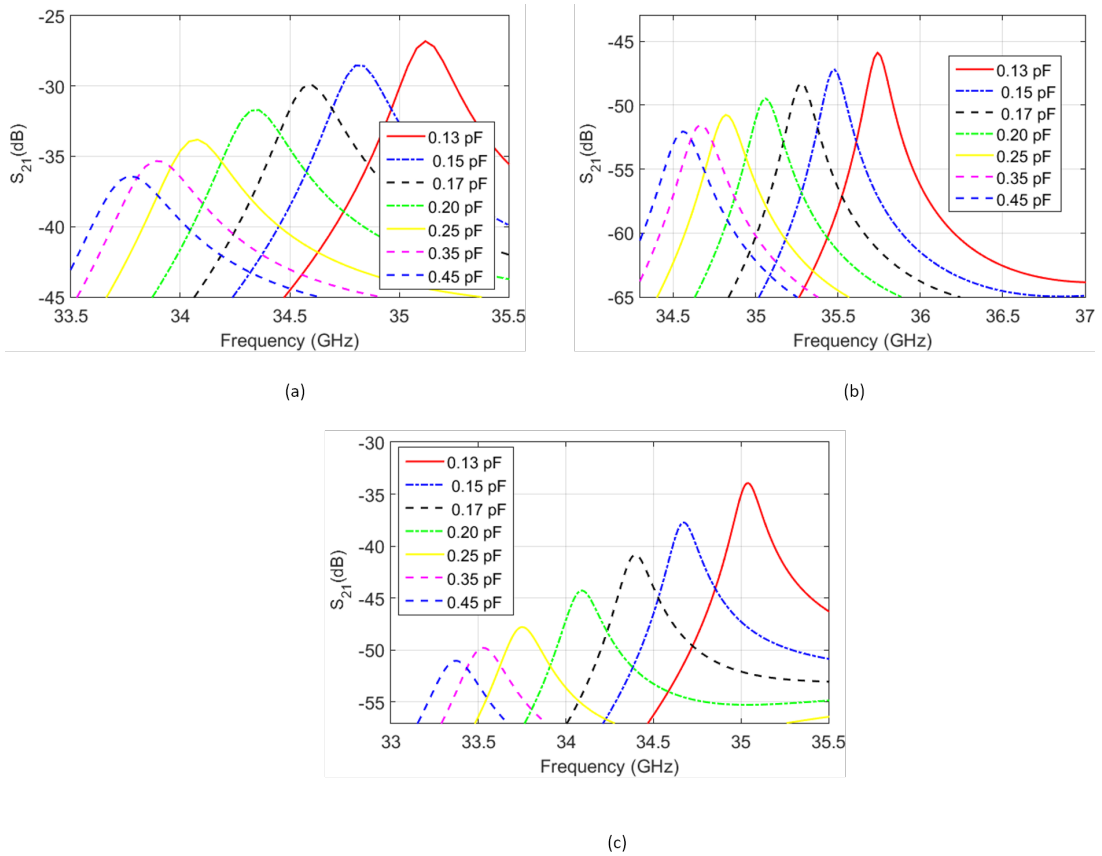


Figure 6.10: EM co-simulation result of S_{21} (dB) of the PGGWG cavity using the equivalent circuit model of MACOM 46580 varactor diode. (a) Rectangular cavity with a square patch EBG implementation. (b) Square cavity. (c) Circular PGGWG cavity.

Table 6.2: Q-factor comparison between different resonant cavities

	f_0 (GHz)	Q_u	Tuning range %
Rectangular Cavity, Round EBG	31.61 - 32.53	143 - 160	3.36
Rectangular Cavity, Square EBG	33.76 - 35.12	100 - 146	3.95
Square Cavity, Round EBG	34.56 - 35.74	144 - 197	3.35
Circular Cavity, Round EBG	33.36 - 35.03	111 - 219	4.88

in resonant frequencies of a square resonant cavity with the circular resonant cavity in Figure 6.10(c). Table 6.2 compares the tuning range obtained from these geometries. It is observed that a higher tuning range is obtained from a circular cavity, as opposed to the rectangular PGGWG cavity in Figure 6.10(b).

A higher unloaded Q-factor is also obtained for the circular cavity, which is more variable over the tuning range compared to the rectangular cavity.

6.6 Fabricated Circuit and Measurement

The rectangular PGGWG cavity was manufactured using the procedure as described in Section 4.4. Figure 6.11 shows the fabricated circuit with zoomed inserts of the varactor diode inclusion as well as the DC supply line connected to the butterfly stub.

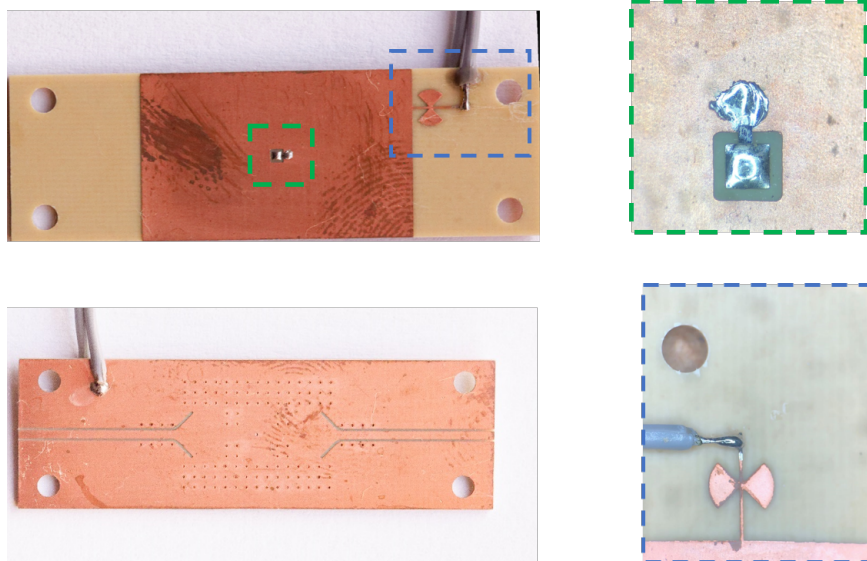


Figure 6.11: Fabricated PGGWG rectangular cavity with varactor diode inclusion.

The measured S_{21} of the tunable K_a -band PGGWG resonator is shown in Figure 6.12. These results are obtained from the continuous DC voltage tuning from 0 - 16V. A resonant frequency variation from 32.52 GHz to 33.98 GHz, corresponding to a 4.48% tuning range, was observed. The unloaded Q factor varied over the tuning range from 63 to 85 with a fairly constant Q of 85 over the first 400 MHz of frequency shift.

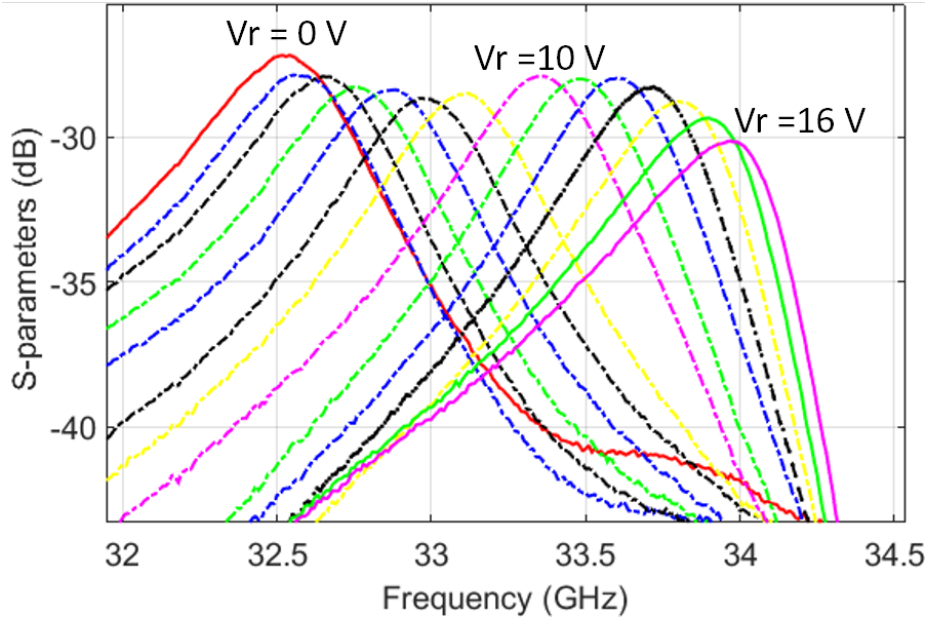


Figure 6.12: Measured S_{21} (dB) of the PGGWG resonant cavity.

The comparison between the simulated and measured result of the rectangular tunable cavity is summarized in Table 6.3. A higher tuning range is observed in measurement compared to the EM hybrid co-simulation result.

Table 6.3: A comparison between simulated and measured results of the tunable K_a -band resonant cavity.

	Simulation	Measurement
Frequency range (GHz)	31.61 - 32.53	32.52 - 33.98
Tuning range (%)	3.36	4.48
Q_u	143 - 160	63 - 85

This shift in frequency observed, can be attributed to fabrication of the circuits. It can be observe from the microscopic image of the cross section $X-X'$ (that is, a cut through the centre patch and conducting via of the PGGWG resonant cavity), that the dimensions slightly differs with that in Table 6.1. Similarly, the cross section $X_1 - X'_1$ in Figure 6.13 shows discrepancy in the simulated dimensions.

Also, the discrepancy in the tuning range can be attributed to possible underestimation of the parasitics of the varactor diode included in simulation.

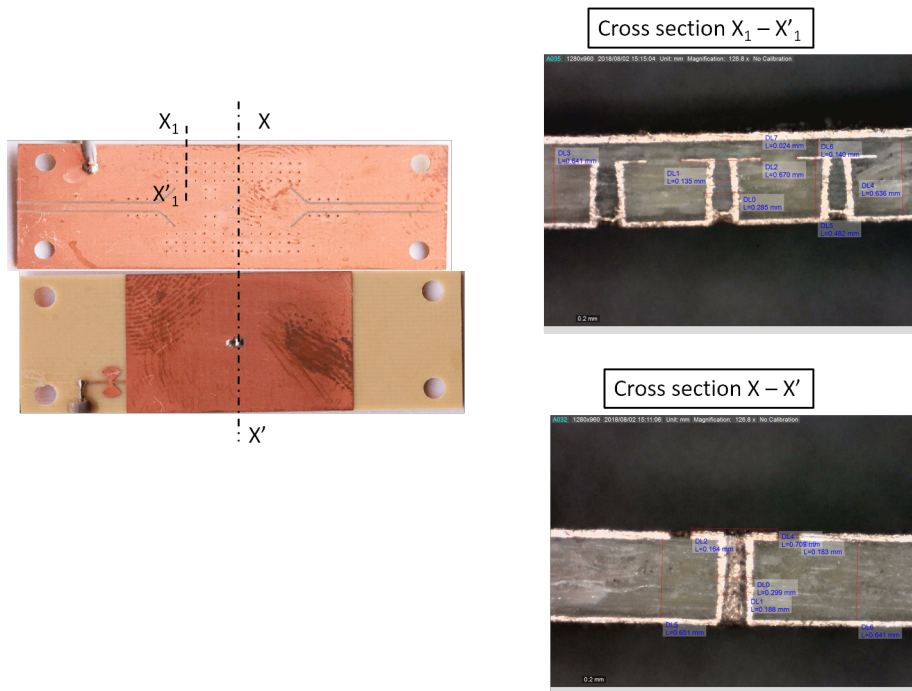


Figure 6.13: Cross section $X-X'$ and $X_1 - X'_1$ showing the microscopic image of the PGGWG sidewall and the cut through the fabricated circuit.

6.7 Conclusion

This chapter presented the development of a tunable PGGWG resonant cavity. It is shown that, with a simple biasing scheme applied to the PGGWG resonant cavity that does not require bridging wires or DC blocking capacitors, continuous tuning of the resonant frequency can be achieved.

A 4.48% continuous frequency tuning range was obtained in the measurement of the cavity for a 0 - 16V applied bias range, as opposed to 3.36% obtained in simulation. The difference can be attributed to possible discrepancy in the modelling of the parasitics of the varactor packaging, as well as the fabrication tolerance.

A simulation comparison between different electronically tunable resonant PGGWG cavities presented shows that the unloaded Q-factor is fairly constant over the tuning range, with higher tuning range observed from a circular PGGWG resonant cavity.

A measured range of 63 - 85 in unloaded quality factor for the rectangular tunable cavity was obtained. This low value, as opposed to an unloaded PGGWG cavity Q-value of 209, is expected due to the combine loading of the cavity, in addition to the varactor's resistance.

The results are promising for future use of PGGWG cavities in VCOs and tunable filters.

Chapter 7

Conclusions

This work presents a new planar waveguide topology called PGGWG derived from the machined GGWG. This structure is entirely implemented on a standard PCB process, making it a practical planar alternative to SIW.

In Chapter 3, the PGGWG was introduced. The structure was shown to be DC isolated between the conducting planes, as opposed to SIW. This is made possible by replacing the through-hole plated via sidewalls with embedded EBG structures that act as AMCs to form conducting sidewalls. A geometrical study of the unit cell shows that it is possible to design the EBG to create a bandgap, and a corresponding AMC sidewall, within a desired frequency band.

Within the stopband created by the EBG cells, it was found that a TE_{10} mode propagates in the groove of the PGGWG. The dispersion diagram of the PGGWG also shows that the cut-off frequency of the fundamental mode that propagates within the bandgap created by the EBG is controlled by the width of the groove, with no spurious parallel plate modes present in the frequency range of interest.

Chapter 4 proposes a CPW to PGGWG transition as a method to excite the PGGWG. Calibration standards in PGGWG were also developed to de-embed the CPW to PGGWG transition, as well as the coaxial adapters in measurement.

The de-embedded measurement results of a 9.20 mm section of the PGGWG line

manufactured in MercuryWave 9350 substrate, having ϵ_r of 3.5 and loss tangent $\tan\delta$ of 0.004, shows a passband of 28 to 40 GHz with 1.2 dB average insertion loss and 0.5 dB variation over the band. The measured return loss was -18 dB on average over the passband, with a good agreement between the simulated and measured phase response.

In Chapter 5, a broadband characterisation of the PGGWG structure in comparison to SIW is presented. The attenuation constant, α of the line shows comparable loss between PGGWG and SIW implemented on the same dielectric substrate material and multi-layer stack up. Attenuation constant of less than 2.5 Np/m was observed over the passband with a mid-band phase constant, β of 1100 rad/m. The phase constant of the PGGWG is shown to be nearly double that of SIW. This result implies that PGGWG has a shorter wavelength than SIW at the same frequency and can be useful in system miniaturisation. This is illustrated with a comparison in resonant cavity size in the two media, where a 25% reduction in the cavity length ($\lambda_g/2$) of the PGGWG as compared to SIW at approximately equal the same resonant frequency was observed.

An unloaded quality factor, Q_u of 209 was obtained from measurement of the PGGWG cavity with a comparable Q_u value of 221 obtained from SIW cavity at the similar resonant frequency.

Chapter 6 presented a tunable PGGWG resonant cavity by connecting a reverse biased varactor diode across a capacitive gap on the top plane to vary the resonant frequency for each applied DC voltage. It demonstrates a further benefit of PGGWG over SIW by exploiting the DC isolated conducting planes to bias a varactor to create a frequency agile combline resonator. In contrast to SIW, no concentric etched rings or bridging wires are required for biasing the varactor.

Measured results shows that a 4.48% continuous frequency tuning range is obtained from 32.52 to 33.98 GHz corresponding to DC bias voltage of 0 - 16V. The resonator Q-factor varied from 63 - 85 across the tuning range.

7.1 Recommendations for Future Developments

The PGGWG has been shown to be an alternative planar waveguide media from the results presented in this thesis. Based on these experimental results, recommendations for future research would include exploring the PGGWG platform for millimeter-wave applications, with focus on the following aspects:

- A more comprehensive experimental characterisation of the PGGWG, exploring different substrate materials and manufacturing processes. This will look at using different substrate thickness for h_a and h in the PGGWG as well as various EBG structure arrangement and types to form the sidewall. This study could also develop equivalent widths for calculation of PGGWG cut-off frequencies, similar to what has been developed for SIW. The study should, further, be extended to develop a parameterised equivalent circuit model of PGGWG.
- The exploration of multi-mode propagation media based on PGGWG. This will explore the possibility of launching a TEM line within the groove of the waveguide, enabling a simultaneous excitation of the TE_{10} mode of the waveguide and the TEM transmission line. This can be exploited for a dualband, dual-mode passband filter. In addition, with the DC isolation conducting planes of PGGWG, one of the passband filters can be made frequency agile.
- The application of the PGGWG to frequency agile passband filters. This may include the design of multi-band filters with the possibility of activating and deactivating the different passbands. Also, investigating the tuning ranges obtained using different varactor diodes applied to different resonant cavity geometries.

The thesis presented a single tuned PGGWG resonant cavity using varactor diode to vary the capacitance across the gap created on the top plate of the structure as discussed in Section 6.3. It inevitably shows that, with

the advantages the PGGWG has over SIW, the DC isolation of PGGWG provides a simple biasing scheme for frequency agile applications such as tunable cavity.

Conceptually, a tunable narrowband filter could be realised in the PGGWG. However, the resonant cavities will have to be biased with a common bias voltage applied to the top conductor, as explained in Section 6.3.1

Figure 7.1 shows, conceptually, a 4-pole in-line topology tunable filter arrangement. Figure 7.1(a) shows each resonator with the center conductor and the catch pad in Figure 7.1(b). Figure 7.1(c) shows the varactor diode attached to the top conducting plane. By applying similar biasing scheme developed in Section 6.3, each resonance cavity could be co-tuned.

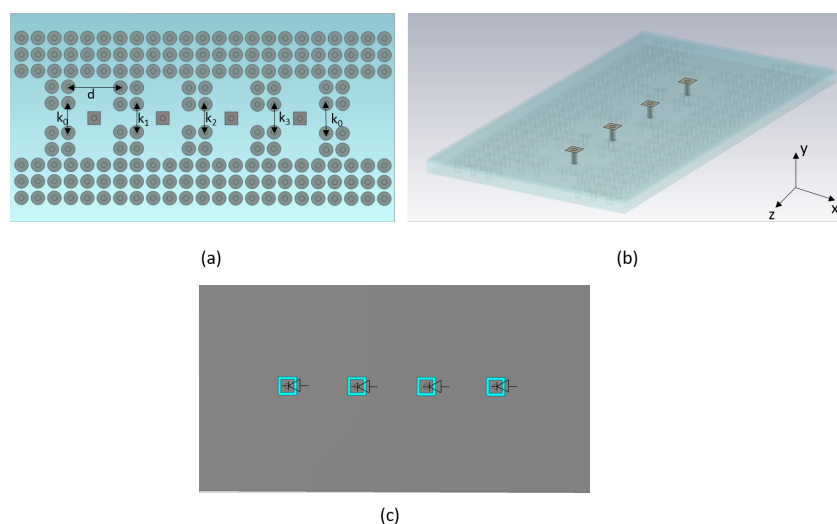


Figure 7.1: 4-pole conceptual narrowband PGGWG tunable filter.(a) Cavity arrangement show the cavity length and inter-resonator coupling. (b) Center cavity post and catch pad. (c) Top view showing the varactor diode attachment to the top plate.

The biasing scheme developed in Section 6.3 for the PGGWG tunable cavity could also be extended to voltage-controlled oscillators (VCO). A VCO is required to have low phase noise, high power output, high tuning range and high Q-factor resonator

Figure 7.2 shows the arrangement of a rectangular PGGWG cavity that could be used in the implementation of VCOs. The cavity is perturbed by a center conductor via with a cut-out gap on the top PGGWG conductor as shown in Figure 7.2(a). Figure 7.2(b) and (c) shows the gap on the top plane. By varying the capacitance across this gap with a varactor diode, the resonance frequency can be altered and, consequently, the oscillation frequency.

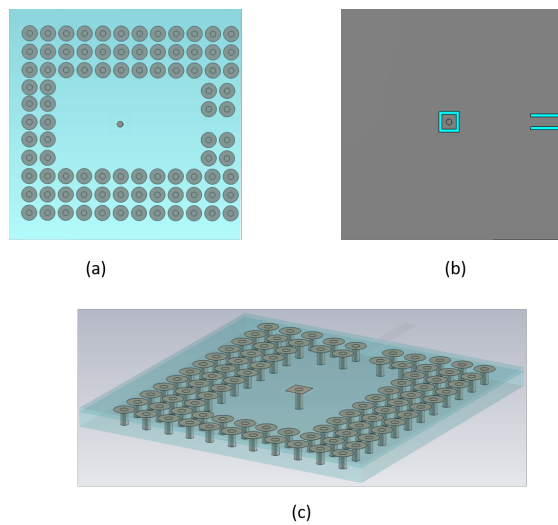


Figure 7.2: PGGWG resonance cavity. (a) PGGWG cavity with center conductor. (b) Top view of the cavity. (c) View of the center conductor and catch pad.

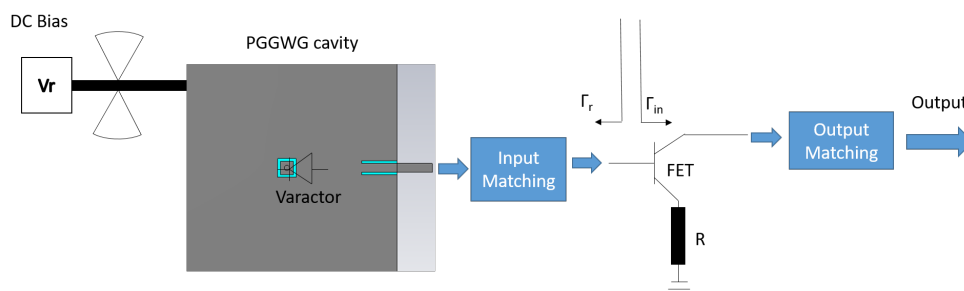


Figure 7.3: Conceptual layout of PGGWG VCO implementation

The schematic of VCO using the common-gate configuration could con-

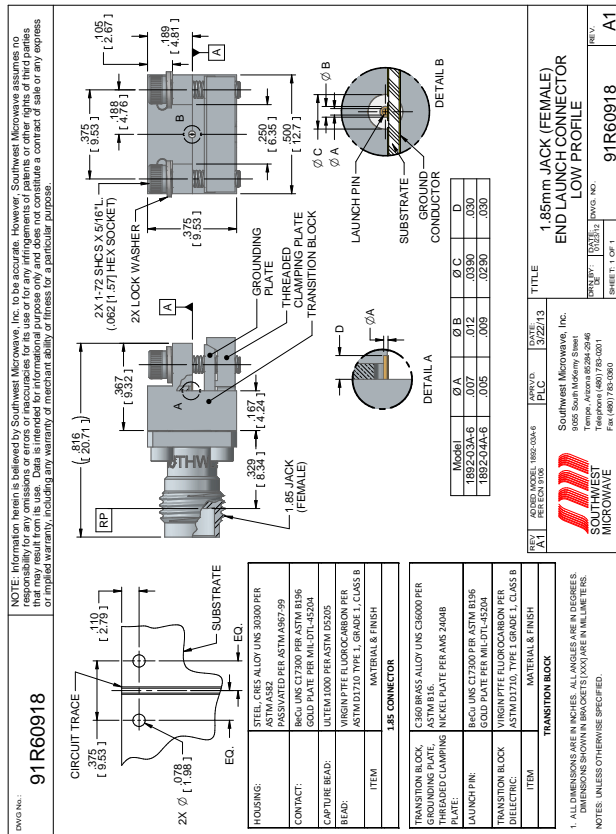
ceptually be implemented as shown in Figure 7.3. The PGGWG cavity is connected to an FET transistor with input and output matching networks. The VCO design is based on the negative resistance concept using a common-source series resistor, R feedback to generate the negative resistance [98], [99].

The DC bias voltage can be applied to the top plane of the PGGWG cavity with the varactor diode connected in reverse bias, provided that the input matching network includes a DC block (to avoid influence on the biasing of the negative resistance circuit). This will eliminate the use of bridging wires as in the case of SIW VCOs, which may introduce parasitics effects making the bias sensitive to interference [76], [98].

- PGGWG may also be used in slotted array antennas, to showcase the miniaturization effect of PGGWG over SIW implemented slotted array antennas.

Appendix A

Connector



Appendix B

Varactor diode

MA46580 & MA46585



Beam Lead Constant Gamma GaAs Tuning Varactor

Rev. V4

Features

- Constant Gamma = 1.0 & 1.25 available
- High Q (3000 minimum at 4V 50MHz)
- Strong Beam Construction (Minimum 10 gram beam strength)
- Low Parasitic Capacitance
- Close Capacitance tracking
- Lead-Free (RoHS Compliant) equivalents available with 260°C reflow compatibility

Description

The MA46580 & MA46585 series beam lead constant gamma tuning varactors are hyper-abrupt junction gallium arsenide diodes with a constant gamma of 1.0 or 1.25. The high Q values and the elimination of package parasitics make these varactors very attractive for voltage controlled oscillators that require linear tuning. These tuning diodes are useful at frequencies as high as 40 Ghz.

The beam lead design eliminates almost all of the package parasitics resulting in improved linearity of the junction capacitance change with applied reverse bias voltage. This improves tracking between diodes and can improve VCO linearity.

Electrical Specifications @ T_A = +25 °C

Gamma = 1.0²
Gamma4 = 0.9 - 1.1, VR = 2 - 12 Volts
Breakdown Voltage @ I_b = 10µA, V_b = 18 V Min
Reverse Leakage Current @ V_b = 14V, I_b = 50 nA Max

Part Number	Case Style	Total Capacitance ±20%	Total Capacitance Ratio	Q Minimum
		Vr=4V (pF)	Vr=2V Vr=12V f=50MHz	Vr=4V f=50MHz
MA46585-1209	1209	0.5	3.2-5.2	3000

- Notes:
1. Capacitance is measured at 1 MHz.
2. All junctions are hyperabrupt with nominal Γ = 1.0 or 1.25
3. Reverse voltage (VR) is measured at 10 microamps.

Absolute Maximum Ratings @ T_A = +25 °C

(Unless Otherwise Noted)¹

Parameter	Absolute Maximum
Reverse Voltage	18V
Operating Temperature	-65°C to +150°C
Storage Temperature	-65°C to +200°C
Power Dissipation	25mW at 25 °C
Beam Strength	10 grams minimum

1. Operation of this device above any one of these parameters may cause permanent damage.

Applications

These beam lead constant gamma tuning varactors are particularly useful in broadband VCO's, where linear frequency tuning is an important feature. They are also very useful for FM modulating a source for telecommunication transmitter and in many cases such circuits can be designed without a linearization circuit.

Electrical Specifications @ T_A = +25 °C

Gamma = 1.25²
Gamma4 = 1.13-1.38, VR = 2 - 12 Volts
Breakdown Voltage @ I_b = 10µA, V_b = 18 V Min
Reverse Leakage Current @ V_b = 14V, I_b = 50 nA Max

Part Number	Case Style	Total Capacitance ±20%	Total Capacitance Ratio	Q Minimum
		Vr=4V (pF)	Vr=2V Vr=12V f=50MHz	Vr=4V f=50MHz
MA46580-1209	1209	0.5	4.5-6.5	3000

ADVANCED: Data Sheets contain information regarding a product MACCOM Technology Solutions is considering for development. Performance is based on target specifications, simulated results, and/or prototype measurements. Commitment to develop is not guaranteed.
PRELIMINARY: Data Sheets contain information regarding a product MACCOM Technology Solutions has under development. Performance is based on engineering tests. Specifications are typical. Mechanical outline has been fixed. Engineering samples and/or test data may be available. Commitment to produce in volume is not guaranteed.
MACCOM Technology Solutions Inc. and its affiliates reserve the right to make changes to the product(s) or information contained herein without notice.
North America Tel: 800.366.2266 / Fax: 978.366.2266
Europe Tel: 44.1938.076200 / Fax: 44.1938.076200
Asia/Pacific Tel: 81.44.844.8296 / Fax: 81.44.844.8298
Site: www.maccomtech.com for additional data sheets and product information.

MA46580 & MA46585

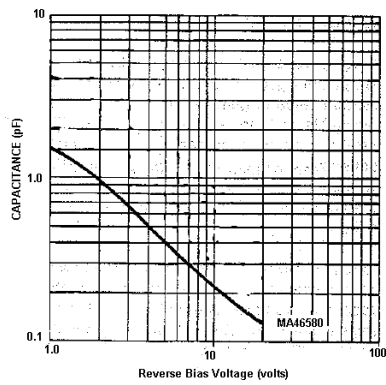


Beam Lead Constant Gamma GaAs Tuning Varactor

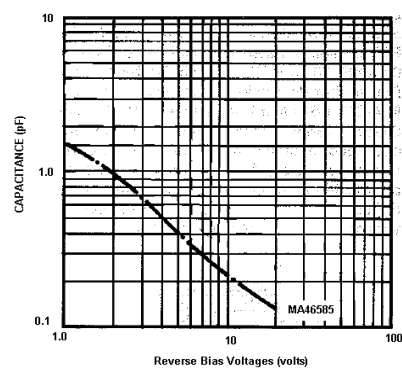
Rev. V4

Typical Performance Curves @ 25°C

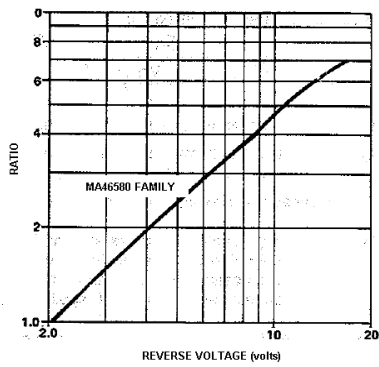
Capacitance vs. Voltage



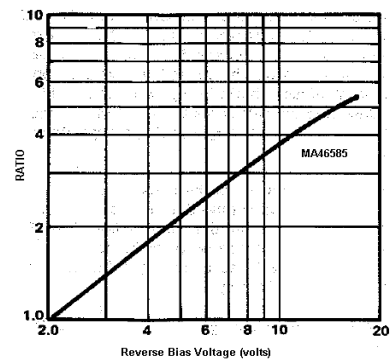
Capacitance vs. Voltage



Capacitance Ratio CT2V/CTV



Capacitance Ratio CT2V/CTV



2

ADVANCED: Data Sheets contain information regarding a product M/A-COM Technology Solutions is considering for development. Performance is based on target specifications, simulated results, and/or prototype measurements. Commitment to develop is not guaranteed.
PRELIMINARY: Data Sheets contain information regarding a product M/A-COM Technology Solutions has under development. Performance is based on engineering tests. Specifications are typical. Mechanical outline has been fixed. Engineering samples and/or test data may be available. Commitment to produce in volume is not guaranteed.

- North America Tel: 800.366.2266 / Fax: 978.366.2266
 - Europe Tel: 44.1908.574.200 / Fax: 44.1908.574.300
 - Asia/Pacific Tel: 81.44.844.8296 / Fax: 81.44.844.8298
- Visit www.macomtech.com for additional data sheets and product information.

M/A-COM Technology Solutions Inc. and its affiliates reserve the right to make changes to the product(s) or information contained herein without notice.

MA46580 & MA46585



Beam Lead Constant Gamma GaAs Tuning Varactor

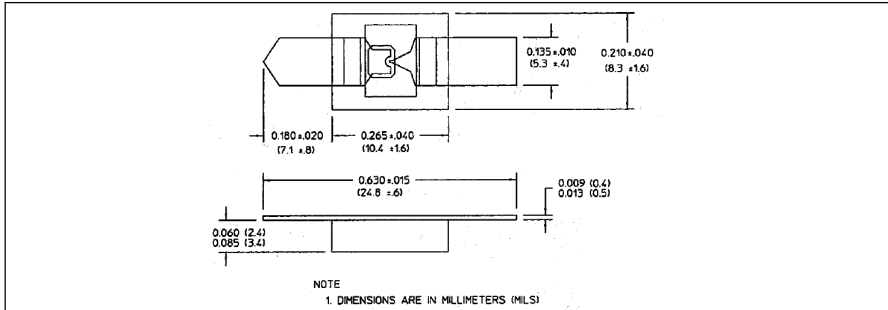
Rev. V4

Environmental Ratings PER MIL-STD-750

	Method	Level
Storage Temperature	1031	See maximum ratings
Temperature Cycle	1051	10 cycles, -65°C to +175°C
Shock	2016	500 g's
Vibration	2056	15 g's
Constant Acceleration	2006	20,000 g's
Humidity	1021	10 days
Constant Acceleration	2006	20,000 g's
Humidity	1021	10 days

Case Styles

ODS-1209



BONDING BEAM LEAD DIODES

The preferred methods for bonding a beam lead diode are thermal compression bonding and parallel gap welding. For thermal compression bonding, the beam lead diode is placed down (gold beam to gold plated substrate) with the leads resting flat on the pad and the bond is made by using a heated wedge. Heat and pressure form a metallurgical bond. A minimum of 100 microinches of gold on the substrate is recommended for optimum bonding.

In the parallel gap technique, current is first passed through the substrate metallization, then through the device lead. Most of the heat is generated at the interface. Care must be taken to see that the step welder does not discharge through the diode junction or the diode will be destroyed. The bonding pressure should be approximately 900 gms/mm².

The major advantage of the parallel gap technique is that a cold ambient may be used. Heat is only generated in the vicinity of the bond itself. Caution must be taken when making the second bond because if the diode is placed in tension, the lead may break.

The following precautions will ensure better results when bonding beam leads:

- To minimize the lead inductance, the wedge, or heated tips should be placed as close as possible to

the edge of the chip without touching it. The chip is very easily damaged, and care must be taken that the bonding tip does not contact the chip at any time during the bonding process.

The bonding tip must be perpendicular to the beam during bonding, to prevent a torsional force which will pull the beams apart. This is particularly important when bonding the second lead.

BONDING TO SOFT CIRCUITS

Beam lead diode can be soft soldered, epoxied or parallel gap welded to Teflon fiberglass or soft circuit boards if low bond pressure is used. Bonding pressure must be reduced to a minimum to prevent diode breakage by forcing the beam into the board.

In general, soft soldering or reflow soldering is the preferable technique. The circuit board should be pre-tinned with solder or a solder plating to obtain the best wetting. Solder melting temperatures of 225-300°C are most satisfactory. Usually, the circuit board manufacturer's solder recommendations should be followed.

Conductive solder paste such as high conducting silver filled epoxy will also result in good low loss bonds. Care should be taken to ensure that the wet paste does not run up the beam lead and short it.

3

ADVANCED: Data Sheets contain information regarding a product M/A-COM Technology Solutions is considering for development. Performance is based on target specifications, simulated results, and/or prototype measurements. Commitment to develop is not guaranteed.
PRELIMINARY: Data Sheets contain information regarding a product M/A-COM Technology Solutions has under development. Performance is based on engineering tests. Specifications are typical. Mechanical outline has been fixed. Engineering samples and/or test data may be available. Commitment to produce in volume is not guaranteed.

- North America Tel: 800.366.2266 / Fax: 978.366.2266
 - Europe Tel: 44.1908.574.200 / Fax: 44.1908.574.300
 - Asia/Pacific Tel: 81.44.844.8296 / Fax: 81.44.844.8298
- Visit www.macomtech.com for additional data sheets and product information.

M/A-COM Technology Solutions Inc. and its affiliates reserve the right to make changes to the product(s) or information contained herein without notice.

Bibliography

- [1] M. Bozzi, A. Georgiadis, and K. Wu, “Review of substrate-integrated waveguide circuits and antennas,” *IET Microwaves, Antennas Propagation*, vol. 5, pp. 909–920, June 2011. [1](#), [2](#), [3](#), [4](#), [20](#)
- [2] M. Z. Ur Rehman, Z. Baharudin, M. A. Zakariya, M. H. M. Khir, M. T. Khan, and P. W. Weng, “Recent advances in miniaturization of substrate integrated waveguide bandpass filters and its applications in tunable filters,” *IEEE Business Engineering and Industrial Applications Colloquium (BEIAC)*, pp. 109–114, 2013. [1](#)
- [3] J. Ni, *Development of Tunable and Miniature Microwave Filters for Modern Wireless Communications*. PhD thesis, Heriot-Watt University, 2014. [1](#), [25](#), [85](#)
- [4] K. Entesari, A. P. Saghati, V. Sekar, and M. Armendariz, “Tunable SIW structures: Antennas, VCOs, and filters,” *IEEE Microwave Magazine*, vol. 16, pp. 34–54, June 2015. [1](#), [2](#), [24](#), [25](#), [26](#), [27](#)
- [5] Z. Brito-Brito, J. C. B. Reyes, and I. Llamas-Garro, “Recent advances in reconfigurable microwave filters,” *Proceedings of the SBMO/IEEE MTT-S International Microwave and Optoelectronics Conference (IMOC 2011)*, pp. 338–346, 2011. [1](#)
- [6] T. S. Rappaport, S. Sun, R. Mayzus, H. Zhao, Y. Azar, K. Wang, G. N. Wong, J. K. Schulz, M. Samimi, and F. Gutierrez, “Millimeter wave mobile communications for 5G cellular: It will work!,” *IEEE Access*, vol. 1, pp. 335–349, 2013. [2](#)

- [7] I. Hunter, “Electronically Reconfigurable Microwave Bandpass Filter,” *IEEE Transactions on Microwave Theory and Techniques*, vol. 57, no. 12, pp. 3070–3079, 2009. [2](#)
- [8] F. Giuppi, A. Georgiadis, A. Collado, M. Bozzi, and L. Perregrini, “Tunable SIW cavity backed active antenna oscillator,” *Electronics Letters*, vol. 46, pp. 1053–1055, July 2010. [2](#), [25](#), [27](#)
- [9] K. W. Eccleston, “Mode analysis of the corrugated substrate integrated waveguide,” *IEEE Transactions on Microwave Theory and Techniques*, vol. 60, pp. 3004–3012, Oct 2012. [2](#), [4](#), [5](#), [25](#)
- [10] E. Rajo-Iglesias and P. S. Kildal, “Groove gap waveguide: A rectangular waveguide between contactless metal plates enabled by parallel-plate cut-off,” in *Proceedings of the 4th European Conference on Antennas and Propagation*, pp. 1–4, April 2010. [2](#), [19](#)
- [11] D. M. Pozar, *Microwave Engineering*. John Wiley and Sons, 4 ed., 2012. [2](#), [13](#), [74](#), [75](#)
- [12] M. Bozzi, S. A. Winkler, and K. Wu, “Broadband and compact ridge substrate-integrated waveguides,” *IET Microwaves, Antennas Propagation*, vol. 4, pp. 1965–1973, November 2010. [2](#)
- [13] K. Wu, D. Deslandes, and Y. Cassivi, “The Substrate Integrated Circuits - A New Concept for High-Frequency Electronics and Optoelectronics,” *Telecommunications in Modern Satellite, Cable and Broadcasting Service, 2003. TELSIKS 2003. 6th International Conference on*, vol. 1, pp. P–III–P–X vol.1, 2003. [2](#), [3](#)
- [14] M. Bozzi, P. Luca, K. Wu, and P. Arcioni, “Current and future research trends in substrate integrated waveguide technology,” *Radioengineering*, vol. 18, pp. 201–209, Jun 2009. [2](#), [3](#)
- [15] M. Armendariz, V. Sekar, and K. Entesari, “Tunable SIW bandpass filters with PIN diodes,” in *Proceedings of the 40th European Microwave Conference*, pp. 830–833, September 2010. [2](#), [24](#), [25](#), [27](#)

- [16] Z. Li and K. Wu, “24GHz FMCW radar front-end system on substrate,” in *IEEE Radio and Wireless Symposium*, pp. 233–236, January 2007. [2](#)
- [17] M. Bozzi, S. A. Winkler, and K. Wu, “Novel compact and broadband interconnects based on ridge substrate integrated waveguide,” *IEEE MTT-S International Microwave Symposium Digest*, pp. 121–124, June 2009. [3](#), [4](#)
- [18] W. Shen, W. Y. Yin, and X. W. Sun, “Miniaturized dual-band substrate integrated waveguide filter with controllable bandwidths,” *IEEE Microwave and Wireless Components Letters*, vol. 21, pp. 418–420, Aug 2011. [3](#)
- [19] P. Russer and Y. L. Chow, “Propagation and band broadening effect of planar integrated ridged waveguide in multilayer dielectric substrates,” *IEEE MTT-S International Microwave Symposium Digest*, pp. 217–220, June 2008. [3](#)
- [20] Y. Wang, W. Hong, Y. Dong, B. Liu, H. J. Tang, J. Chen, X. Yin, and K. Wu, “Half mode substrate integrated waveguide (HMSIW) bandpass filter,” *IEEE Microwave and Wireless Components Letters*, vol. 17, pp. 265–267, April 2007. [3](#), [4](#)
- [21] L. S. Wu, X. L. Zhou, and W. Y. Yin, “Evanescent-mode bandpass filters using folded and ridge substrate integrated waveguides (SIWs),” *IEEE Microwave and Wireless Components Letters*, vol. 19, pp. 161–163, March 2009. [4](#)
- [22] Z. Wang, S. Bu, and Z. Luo, “A substrate integrated folded waveguide (SIFW) H-plane band-pass filter with double H-plane septa based on LTCC,” *IEEE Transactions on Ultrasonics, Ferroelectrics and Frequency Control*, vol. 59, pp. 560–563, Mar. 2012. [4](#)
- [23] W. Hong, B. Liu, Y. Wang, Q. Lai, H. Tang, X. X. Yin, Y. D. Dong, Y. Zhang, and K. Wu, “Half mode substrate integrated waveguide: A new guided wave structure for microwave and millimeter wave application,” in *Joint 31st International Conference on Infrared Millimeter Waves and 14th International Conference on Terahertz Electronics*, pp. 219–219, September 2006. [4](#)

- [24] S. A. Shakib, V. Sekar, and K. Entesari, “A compact triple-band bandpass filter based on half-mode substrate integrated waveguides,” in *Proceedings of the 42nd European Microwave Conference*, pp. 116–119, October 2012. [4](#)
- [25] D. G. Chen and K. W. Eccleston, “Substrate integrated waveguide with corrugated wall,” in *Proceedings of the Asia-Pacific Microwave Conference*, pp. 1–4, December 2008. [4](#)
- [26] J. R. Sanchez, C. Bachiller, H. Esteban, A. Belenguer, V. Nova, and V. Boria, “New decoupled empty substrate integrated waveguide realisation,” *Electronics Letters*, vol. 53, no. 17, pp. 1203–1205, 2017. [5](#), [6](#), [69](#)
- [27] A. Niembro-Martin, V. Nasserddine, E. Pistono, H. Issa, A. L. Franc, T. P. Vuong, and P. Ferrari, “Slow-wave substrate integrated waveguide,” *IEEE Transactions on Microwave Theory and Techniques*, vol. 62, pp. 1625–1633, Aug 2014. [6](#), [7](#)
- [28] N. Bayat-Makou and A. A. Kishk, “Realistic air-filled TEM printed parallel-plate waveguide based on ridge gap waveguide,” *IEEE Transactions on Microwave Theory and Techniques*, vol. 66, pp. 2128–2140, May 2018. [7](#), [8](#)
- [29] J. Zhang, X. Zhang, and D. Shen, “Design of substrate integrated gap waveguide,” in *IEEE MTT-S International Microwave Symposium (IMS)*, pp. 1–4, May 2016. [8](#), [24](#)
- [30] F. He, X. P. Chen, K. Wu, and W. Hong, “Electrically tunable substrate integrated waveguide reflective cavity resonator,” in *Proceedings of the Asia Pacific Microwave Conference*, pp. 119–122, December 2009. [8](#), [24](#), [25](#)
- [31] S. Sirci, J. D. Martinez, M. Taroncher, and V. E. Boria, “Varactor-loaded continuously tunable SIW resonator for reconfigurable filter design,” in *Proceedings of the 41st European Microwave Conference*, pp. 436–439, 2011. [8](#), [24](#), [25](#), [27](#), [83](#), [84](#)
- [32] R. J. Cameron, R. Mansour, and C. M. Kudsia, *Microwave Filters for Communication Systems: Fundamentals, Design and Applications*. Wiley, 2007. [13](#)

- [33] D. Sun and J. Xu, "Rectangular waveguide coupler with adjustable coupling coefficient using gap waveguide technology," *Electronics Letters*, vol. 53, no. 3, pp. 167–169, 2017. [13](#)
- [34] C. Carceller, P. Soto, V. E. Boria, and M. Guglielmi, "Design of hybrid folded rectangular waveguide filters with transmission zeros below the pass-band," *IEEE Transactions on Microwave Theory and Techniques*, vol. 64, pp. 475–485, Feb 2016. [13](#)
- [35] X. Li, E. Li, and G. Guo, "Design of X-band H-plane waveguide Y-junction circulator," in *Proceedings of the International Workshop on Microwave and Millimeter Wave Circuits and System Technology*, pp. 1–4, April 2012. [13](#)
- [36] P. S. Kildal, "Three metamaterial-based gap waveguides between parallel metal plates for mm/submm waves," in *2009 3rd European Conference on Antennas and Propagation*, pp. 28–32, March 2009. [14](#), [15](#), [17](#)
- [37] A. Berenguer, D. Sanchez-Escuderos, B. Bernardo-Clemente, M. Baquero-Escudero, and V. E. Boria, "Groove gap waveguide as an alternative to rectangular waveguide for H-plane components," *Electronics Letters*, vol. 52, no. 11, pp. 939–941, 2016. [14](#)
- [38] H. Raza, J. Yang, P. S. Kildal, and E. Alfonso, "Resemblance between gap waveguides and hollow waveguides," *IET Microwaves, Antennas Propagation*, vol. 7, pp. 1221–1227, December 2013. [14](#), [16](#), [20](#), [21](#), [44](#)
- [39] P. S. Kildal, A. U. Zaman, E. Rajo-Iglesias, E. Alfonso, and A. Valero-Nogueira, "Design and experimental verification of ridge gap waveguide in bed of nails for parallel-plate mode suppression," *IET Microwaves, Antennas Propagation*, vol. 5, pp. 262–270, February 2011. [14](#), [16](#), [22](#)
- [40] P. S. Kildal, E. Alfonso, A. Valero-Nogueira, and E. Rajo-Iglesias, "Local metamaterial-based waveguides in gaps between parallel metal plates," *IEEE Antennas and Wireless Propagation Letters*, vol. 8, pp. 84–87, 2009. [14](#), [16](#), [19](#)

- [41] E. Pucci, *Gap Waveguide Technology for millimeter Wave Applications and Integration with Antennas*. PhD thesis, Chalmers University of Technology, 2013. [14](#), [15](#)
- [42] J. Zhang, X. Zhang, D. Shen, and K. Wu, “Gap waveguide PMC packaging for a SIW-GCPW-based filter,” *IEEE Microwave and Wireless Components Letters*, vol. 26, pp. 159–161, March 2016. [16](#)
- [43] A. U. Zaman, M. Alexanderson, T. Vukusic, and P. S. Kildal, “Gap waveguide PMC packaging for improved isolation of circuit components in high-frequency microwave modules,” *IEEE Transactions on Components, Packaging and Manufacturing Technology*, vol. 4, pp. 16–25, Jan 2014. [16](#)
- [44] E. Rajo-Iglesias, A. U. Zaman, and P. S. Kildal, “Parallel plate cavity mode suppression in microstrip circuit packages using a lid of nails,” *IEEE Microwave and Wireless Components Letters*, vol. 20, pp. 31–33, Jan 2010. [16](#)
- [45] H. Raza and J. Yang, “Compact UWB power divider packaged by using gap-waveguide technology,” in *Proceedings of the 6th European Conference on Antennas and Propagation (EUCAP)*, pp. 2938–2942, March 2012. [16](#)
- [46] A. A. Brazalez, A. U. Zaman, and P. S. Kildal, “Improved microstrip filters using PMC packaging by lid of nails,” *IEEE Transactions on Components, Packaging and Manufacturing Technology*, vol. 2, pp. 1075–1084, July 2012. [16](#)
- [47] A. U. Zaman, J. Yang, and P. S. Kildal, “Using lid of pins for packaging of microstrip board for descrambling the ports of eleven antenna for radio telescope applications,” in *IEEE Antennas and Propagation Society International Symposium*, pp. 1–4, July 2010. [16](#)
- [48] A. Berenguer, V. Fusco, D. E. Zelenchuk, D. Sanchez-Escuderos, M. Baquero-Escudero, and V. E. Boria-Esbert, “Propagation characteristics of groove gap waveguide below and above cutoff,” *IEEE Transactions on Microwave Theory and Techniques*, vol. 64, pp. 27–36, Jan 2016. [16](#), [20](#), [44](#)

- [49] A. A. Brazález, E. Rajo-Iglesias, J. L. Vázquez-Roy, A. Vosoogh, and P. S. Kildal, “Design and validation of microstrip gap waveguides and their transitions to rectangular waveguide, for millimeter-wave applications,” *IEEE Transactions on Microwave Theory and Techniques*, vol. 63, pp. 4035–4050, Dec 2015. [16](#), [23](#)
- [50] E. Pucci, A. U. Zaman, E. Rajo-Iglesias, and P. S. Kildal, “New low loss inverted microstrip line using gap waveguide technology for slot antenna applications,” in *Proceedings of the 5th European Conference on Antennas and Propagation (EUCAP)*, pp. 979–982, April 2011. [16](#), [23](#), [24](#)
- [51] D. Sievenpiper, L. Zhang, R. F. J. Broas, N. G. Alexopolous, and E. Yablonovitch, “High-impedance electromagnetic surfaces with a forbidden frequency band,” *IEEE Transactions on Microwave Theory and Techniques*, vol. 47, pp. 2059–2074, Nov 1999. [16](#), [18](#), [32](#)
- [52] P. S. Kildal, “Definition of artificially soft and hard surfaces for electromagnetic waves,” *Electronics Letters*, vol. 24, pp. 168–170, Feb 1988. [16](#)
- [53] P.-S. Kildal and A. Kishk, “EM modeling of surfaces with STOP or GO characteristics-artificial magnetic conductors and soft and hard surfaces,” *Applied Computational Electromagnetics Society Journal*, vol. 18, no. 1, pp. 32–40, 2003. [16](#), [17](#), [18](#)
- [54] P. S. Kildal, “Artificially soft and hard surfaces in electromagnetics,” *IEEE Transactions on Antennas and Propagation*, vol. 38, pp. 1537–1544, Oct 1990. [16](#)
- [55] E. Lier, “Analysis of soft and hard strip-loaded horns using a circular cylindrical model,” *IEEE Transactions on Antennas and Propagation*, vol. 38, pp. 783–793, Jun 1990. [16](#)
- [56] E. Rajo-Iglesias and P. S. Kildal, “Numerical studies of bandwidth of parallel-plate cut-off realised by a bed of nails, corrugations and mushroom-type electromagnetic bandgap for use in gap waveguides,” *IET Microwaves, Antennas Propagation*, vol. 5, pp. 282–289, Feb 2011. [17](#), [18](#), [30](#)

- [57] A. Valero-Nogueira, M. Baquero, J. I. Herranz, J. Domenech, E. Alfonso, and A. Vila, “Gap waveguides using a suspended strip on a bed of nails,” *IEEE Antennas and Wireless Propagation Letters*, vol. 10, pp. 1006–1009, 2011. [17](#)
- [58] B. M. Iravani, *Electromagnetic Interference Reduction using Electromagnetic Bandgap Structures in Packages, Enclosures, Cavities, and Antennas*. PhD thesis, University of Maryland, 2007. [17](#), [18](#), [19](#), [30](#), [32](#)
- [59] A. J. B. Verdu, *Analysis and design of efficient passive components for the millimeter-wave and THz bands*. PhD thesis, Universidad Politecnica de Valencia, 2017. [21](#), [22](#), [30](#), [31](#)
- [60] F.-R. Yang, K.-P. Ma, Y. Qian, and T. Itoh, “A novel tem waveguide using uniplanar compact photonic-bandgap (uc-pbg) structure,” *IEEE Transactions on Microwave Theory and Techniques*, vol. 47, pp. 2092–2098, Nov 1999. [20](#)
- [61] A. del Olmo-Olmeda, M. Baquero-Escudero, V. E. Boria-Esbert, A. Valero-Nogueira, and A. J. Berenguer-Verdú, “A novel band-pass filter topology for millimeter-wave applications based on the groove gap waveguide,” in *Microwave Symposium Digest (IMS), 2013 IEEE MTT-S International*, pp. 1–4, June 2013. [21](#)
- [62] A. Berenguer, M. Baquero-Escudero, D. Sanchez-Escuderos, B. Bernardo-Clemente, and V. E. Boria-Esbert, “Low insertion loss 61 GHz narrow-band filter implemented with groove gap waveguides,” in *Proceedings of the 44th Microwave Conference (EuMC)*, pp. 191–194, October 2014. [21](#)
- [63] A. U. Zaman, P. S. Kildal, and A. A. Kishk, “Narrow-band microwave filter using high-Q groove gap waveguide resonators with manufacturing flexibility and no sidewalls,” *IEEE Transactions on Components, Packaging and Manufacturing Technology*, vol. 2, pp. 1882–1889, Nov 2012. [21](#)
- [64] M. Rezaee, A. U. Zaman, and P. S. Kildal, “A groove gap waveguide iris filter for V-band application,” in *Proceedings of the 23rd Iranian Conference on Electrical Engineering*, pp. 462–465, May 2015. [21](#)

- [65] E. Alfonso, M. Baquero, A. Valero-Nogueira, J. I. Herranz, and P. S. Kildal, “Power divider in ridge gap waveguide technology,” in *Proceedings of the 4th European Conference on Antennas and Propagation*, pp. 1–4, April 2010. [22](#)
- [66] E. Alfonso, M. Baquero, P. Kildal, A. Valero-Nogueira, E. Rajo-Iglesias, and J. I. Herranz, “Design of microwave circuits in ridge-gap waveguide technology,” in *2010 IEEE MTT-S International Microwave Symposium*, pp. 1–1, May 2010. [22](#)
- [67] M. S. Sorkherizi, A. Khaleghi, and P. S. Kildal, “Direct-coupled cavity filter in ridge gap waveguide,” *IEEE Transactions on Components, Packaging and Manufacturing Technology*, vol. 4, pp. 490–495, March 2014. [22](#)
- [68] H. Raza, J. Yang, P. S. Kildal, and E. A. Alós, “Microstrip-ridge gap waveguide; study of losses, bends, and transition to WR-15,” *IEEE Transactions on Microwave Theory and Techniques*, vol. 62, pp. 1943–1952, Sept 2014. [23](#), [24](#)
- [69] H. Raza, J. Yang, and P. S. Kildal, “Study of the characteristic impedance of gap waveguide microstrip line realized with square metal pins,” in *Proceedings of the 7th European Conference on Antennas and Propagation (EuCAP)*, pp. 3001–3005, April 2013. [23](#), [24](#)
- [70] E. Pucci, E. Rajo-Iglesias, and P. S. Kildal, “New microstrip gap waveguide on mushroom-type EBG for packaging of microwave components,” *IEEE Microwave and Wireless Components Letters*, vol. 22, pp. 129–131, March 2012. [23](#)
- [71] S. A. Razavi, P. S. Kildal, L. Xiang, E. A. Alós, and H. Chen, “ 2×2 -slot element for 60-GHz planar array antenna realized on two doubled-sided PCBs using SIW cavity and EBG-type soft surface fed by microstrip-ridge gap waveguide,” *IEEE Transactions on Antennas and Propagation*, vol. 62, pp. 4564–4573, Sept 2014. [24](#)
- [72] S. Sirci, J. D. Martínez, and V. E. Boria, “Low-loss 3-bit tunable SIW filter with PIN diodes and integrated bias network,” in *Proceedings of the 2013 European Microwave Conference*, pp. 1211–1214, Oct 2013. [24](#)

- [73] V. Sekar, M. Armendariz, and K. Entesari, “A 1.2 -1.6-GHz substrate-integrated-waveguide RF MEMS tunable filter,” *IEEE Transactions on Microwave Theory and Techniques*, vol. 59, pp. 866–876, April 2011. [25](#)
- [74] F. He, K. Wu, and H. Wei, “Electrically tunable half mode substrate integrated waveguide resonator,” in *Proceedings of the Asia-Pacific Microwave Conference*, pp. 1166–1169, Dec 2011. [25](#)
- [75] S. Sirci, J. D. Martínez, M. Taroncher, and V. E. Boria, “Analog tuning of compact varactor-loaded combline filters in substrate integrated waveguide,” in *Proceedings of the 42nd European Microwave Conference*, pp. 257–260, Oct 2012. [25](#)
- [76] F. F. He, K. Wu, W. Hong, L. Han, and X. Chen, “A low phase-noise VCO using an electronically tunable substrate integrated waveguide resonator,” *IEEE Transactions on Microwave Theory and Techniques*, vol. 58, pp. 3452–3458, Dec 2010. [25](#), [103](#)
- [77] S. Adhikari, Y. J. Ban, and K. Wu, “Magnetically tunable ferrite loaded substrate integrated waveguide cavity resonator,” *IEEE Microwave and Wireless Components Letters*, vol. 21, pp. 139–141, March 2011. [25](#), [26](#), [27](#)
- [78] F. Mira, J. Mateu, and C. Collado, “Mechanical tuning of substrate integrated waveguide filters,” *IEEE Transactions on Microwave Theory and Techniques*, vol. 63, pp. 3939–3946, Dec 2015. [26](#), [27](#)
- [79] A. Anand, J. Small, D. Peroulis, and X. Liu, “Theory and design of octave tunable filters with lumped tuning elements,” *IEEE Transactions on Microwave Theory and Techniques*, vol. 61, pp. 4353–4364, Dec 2013. [27](#)
- [80] T. Oyedokun, R. Geschke, and T. Stander, “Experimental characterisation of planar groove gap waveguide and cavity,” in *Proceedings of the 47th European Microwave Conference (EuMC)*, pp. 436–439, Oct 2017. [29](#)
- [81] S. D. Rogers, “Electromagnetic-bandgap layers for broad-band suppression of TEM modes in power planes,” *IEEE Transactions on Microwave Theory and Techniques*, vol. 53, pp. 2495–2505, Aug 2005. [32](#)

- [82] T. Oyedokun, R. Geschke, and T. Stander, “A geometric study of tunable planar groove gap waveguide cavities,” *IOP Conference Series: Materials Science and Engineering*, vol. 321, no. 1, p. 012008, 2018. [40](#)
- [83] R. Kazemi, A. E. Fathy, S. Yang, and R. A. Sadeghzadeh, “Development of an ultra wide band GCPW to SIW transition,” in *IEEE Radio and Wireless Symposium*, pp. 171–174, Jan 2012. [54](#)
- [84] H. Chen, W. Che, Y. Chao, W. Feng, and K. Wu, “Revisiting and improvement of thru-reflect-line calibration for accurate measurement of substrate integrated waveguide components,” *IET Microwaves, Antennas Propagation*, vol. 11, no. 1, pp. 29–35, 2017. [57](#)
- [85] A. U. Zaman, P. S. Kildal, M. Ferndahl, and A. Kishk, “Validation of ridge gap waveguide performance using in-house TRL calibration kit,” in *Proceedings of the 4th European Conference on Antennas and Propagation*, pp. 1–4, April 2010. [58](#)
- [86] Keysight, *TRL calibration application note*, 2018. [58](#)
- [87] P. I. Somlo, “Some aspects of the measurement of the Q factor of transmission lines,” *IEEE Transactions on Microwave Theory and Techniques*, vol. 11, pp. 472–478, Nov 1963. [72](#)
- [88] F. Grine, T. Djerafi, M. T. Benhabiles, K. Wu, and M. L. Riabi, “High-Q substrate integrated waveguide resonator filter with dielectric loading,” *IEEE Access*, vol. 5, pp. 12526–12532, 2017. [75](#)
- [89] E. Pucci, A. U. Zaman, E. Rajo-Iglesias, P. S. Kildal, and A. Kishk, “Study of Q-factors of ridge and groove gap waveguide resonators,” *IET Microwaves, Antennas Propagation*, vol. 7, pp. 900–908, August 2013. [75](#)
- [90] M. Nathan, *Waveguide handbook*. IET, 1951. [80](#)
- [91] Z. Cai, K. D. Xu, D. Lu, Y. Liu, and X. Tang, “A low phase noise oscillator using SIW combline resonator,” in *IEEE MTT-S International Microwave Symposium (IMS)*, pp. 1976–1978, June 2017. [80](#)

- [92] J. D. Martinez, S. Sirci, M. Taroncher, and V. E. Boria, "Compact CPW-fed combline filter in substrate integrated waveguide technology," *IEEE Microwave and Wireless Components Letters*, vol. 22, pp. 7–9, Jan 2012. 80
- [93] G. Zhang, Y. Xu, and X. Wang, "Compact tunable bandpass filter with wide tuning range of centre frequency and bandwidth using short coupled lines," *IEEE Access*, vol. 6, pp. 2962–2969, 2018. 85
- [94] T. S. Beukman, "Tune-all wideband planar filters for kat-7," Master's thesis, University of Stellenbosch, 2011. 85
- [95] T. S. Beukman and R. H. Geschke, "A tune-all wideband filter based on perturbed ring-resonators," *IEEE Microwave and Wireless Components Letters*, vol. 23, pp. 131–133, March 2013. 85
- [96] Skyworks, *Varactor diode application note*, 2018. Accessed July 2, 2018. 86
- [97] MACOM, "<https://www.macom.com>," 2018. Accessed July 2, 2018. 86
- [98] Z. Chen, W. Hong, J. Chen, and J. Zhou, "Design of high-q tunable siw resonator and its application to low phase noise vco," *IEEE Microwave and Wireless Components Letters*, vol. 23, pp. 43–45, Jan 2013. 103
- [99] A. P. Saghati and K. Entesari, "A 1.7–2.2 ghz compact low phase-noise vco using a widely-tuned siw resonator," *IEEE Microwave and Wireless Components Letters*, vol. 24, pp. 622–624, Sep. 2014. 103